NORTHWESTERN UNIVERSITY

Nanomechanical Properties of Cementitious Materials

A DISSERTATION

SUBMITTED TO THE GRADUATE SCHOOL

IN PARTIAL FULFILLMENT OF THE REQUIREMENTS

for the degree

DOCTOR OF PHILOSOPHY

Field of Civil and Environmental Engineering

By

Paramita Mondal

EVANSTON, ILLINOIS

December 2008

ABSTRACT

Nanomechanical Properties of Cementitious Materials

Paramita Mondal

Although cementitious construction materials are mainly used in a large scale and in huge quantities, fundamental properties such as strength, ductility, creep, shrinkage, and fracture behavior depend, to a great extent, on structural elements and phenomena which are effective at the micro- and nanoscale. This research involves characterization of the micro- and nanoscale properties of cementitious materials using various imaging techniques and evaluation of local mechanical properties. A systematic sample preparation technique developed in this work enabled the investigation of the microstructure and nanostructure of cement paste using atomic force microscopy and a novel nanoindentation technique. An in-depth study on the effects of curing age, water to cement ratio, and micro- and nano-modifiers on the nanomechanical properties of concrete was performed. Furthermore, this study examined experimentally the nanomechanical properties of the interfacial transition zone (ITZ) in concrete. Despite the difficulties associated with the complex nature of the ITZ, this dissertation reports one of the first, most comprehensive endeavors to successfully measure its local nanomechanical properties. Additionally, the effects of silica fume and nanosilica additives on bulk paste were investigated. The ultimate goal of this research is to control the macroscopic properties and develop new materials with improved properties. Findings from this work will lead to a better understanding of the complex macroscopic phenomena and also provide input for multiscale modeling.

Acknowledgments

I express my sincere gratitude towards my advisor Prof. Surendra P. Shah for his guidance and support throughout this work. He has always motivated and encouraged me to grow in my career. I am thankful to him for introducing me to other specialists in many national and international conferences that facilitated fruitful discussions and international collaboration. I am grateful to my co-advisor Prof. Laurence D. Marks for his guidance and encouragement. His novel ideas were an inspiration, making this interdisciplinary work a great learning experience for me. A special thanks goes to my committee member, Prof. Hamlin Jennings. I greatly appreciate his valuable thoughts and constructive suggestions on numerous occasions. I also thank Prof. Leon Keer for his valuable suggestions and participation in my qualifier and defense committee.

I greatly acknowledge the support of the Center for Advanced Cement-Based Materials (ACBM), the Walter P. Murphy and the Richter Terminal Year Fellowship committees at Northwestern University, and the Federal Highway Administration for funding this work and my graduate career.

I would like to thank everybody in the ACBM family, my colleagues from the Civil Engineering department, the group members of Prof. Marks' team, and other colleagues from the Materials Science department for their academic discussions and friendship. They helped make graduate student life bearable outside the lab. A special thanks goes to Dr. Raissa Ferron and Nathan Tregger for many discussions on research and academia. I would like to mention Dr. Juan Gaitero for his direct involvement in this research and Zoi Metaxa for her interest in continuing the work. My special gratitude goes towards Richard Garza and Janet Soule for providing the support and

creating a friendly and productive work environment. I would also like to thank Priscilla Fonseca for her invaluable assistance with proofreading this dissertation.

This acknowledgement recognizes the support provided by the Atomic - and Nanoscale Characterization Experimental Center at Northwestern University. I would like to thank Dr. Gajendra S. Shekhawat from this center for his valuable suggestions throughout this work. I would also like to recognize the support provided by Steve Albertson from the ACBM center.

I sincerely thank my friends, specially Debjit, Peter and Arindam, for always being there. I would also like to thank my parents and my sister, Poulami, for their love and support, and for having faith in me. Finally, I would like to thank my husband, Santanu, for his continuous encouragement and support to accomplish this goal.

Table of Contents

List of Tables

List of Figures

Chapter 1 Introduction

Concrete is the most widely used construction material made commonly by mixing Portland cement, sand, crushed rock, and water [49]. As quoted by Mehata and Monteiro [47] from an article in Scientific American, April 1964, by S. Brunauer and L. E. Copeland, *"The total world consumption of concrete last year is estimated at three billion tons, or one ton for every living human being. Man consumes no material except water in such tremendous quantities"*. Present concrete consumption is much higher than what it was almost 40 years ago. In 2000, consumption of concrete in the world was of the order of 11 billion metric tons per year. The amount of world trade associated with concrete is estimated to be about 13 to 14 trillion dollars, providing jobs to 1% of the world's population. In North America, construction is a trillion-dollar industry where concrete is the most used material. Over the past 100 years, concrete has made major progress in quality and performance through scientific and technological innovations. Nevertheless, little

is known about the properties of concrete at the micro- and nanoscale, which governs its overall properties such as strength, ductility, durability etc. Concrete is the material of choice for new construction of high-rise buildings, roadway pavements, and bridges. Additionally, there is a huge demand for repair and rehabilitation to maintain functionality of the National Highway System. The highways and bridges in the US are deteriorating under heavy traffic and the freeze-thaw cycle caused by adverse weather. According to estimates by the U.S. Department of Transportation, the current backlog of unfunded repairs totals $495 billion. The construction industry is facing an escalating need for high-performance, durable, and sustainable construction materials for buildings and roadway pavements. This need, in turn, is driving research to develop the next generation of materials. In Civil Engineering, the traditional method of designing a concrete mix is by trial and error where different additives are used to achieve a set of final properties. Recently, however the construction industry has recognized the need to investigate the science and fundamental properties of concrete and other construction materials.

1.1. Goal and Objective of the Research

The science of nanotechnology offers a unique opportunity to transform this material into a more robust, environmentally sustainable material. The nanostructure of concrete, which is controlled by the structure of calcium silicate hydrate (C-S-H), governs fundamental properties such as strength, ductility, early age rheology, creep, shrinkage, fracture behavior, and durability. This demands a detailed knowledge of the nanostructure and how it relates to local mechanical properties. However, the complexity and the delicate nature of the C-S-H gel produced by cement hydration makes it extremely challenging to characterize at the nanoscale. Over last the 100 years,

researchers used different experimental techniques to characterize this material to come up with a description of the morphology and developed a relationship between the microstructure and macroscopic properties. While several models describing the structural evolution of C-S-H at the crystal chemical level exist, the link between nano- and microstructure and mechanical behavior of C-S-H is still unresolved. The ultimate goal of this kind of research is to be able to control macroscopic properties from the nanoscale and develop nano-engineered materials. This research is the first step to achieve this final goal. The immediate objective is to determine the local mechanical properties, particularly the elastic modulus and hardness of the cementitious materials microstructure.

Nanoindentation techniques have been used to determine local mechanical properties of different phases present in the cement paste and concrete microstructure. Nanoindentation has its origins in the Mohs hardness scale developed in 1822, in which one material is considered to be harder if it can leave a permanent scratch on another material [31]. One material of known properties is used to indent the material with unknown mechanical properties. Nanoindentation was also used to determine the local mechanical properties of the interfacial transition zone (ITZ) in cement paste. Although it is widely accepted that the properties of the ITZ have to be taken into account in modeling the overall mechanical properties, current models make assumptions without much theory or experimental support. This research is one of the first endeavors to characterize the nanomechanical properties of the ITZ using nanoindentation. Furthermore, nanoindentation was used to investigate the effects of the addition of silica fume, a micro-modifier, and nanosilica, a nano-modifier.

1.2. Structure of this Thesis

This thesis is structured as follows. Chapter 2.1 reviews the literature on the microstructure of concrete, models of C-S-H, and various experimental methodologies for determination of local mechanical properties of different phases of concrete. In Chapter 3, a review of contact mechanics and theory of nanoindentation is provided.

Nanoindentation theory is developed from contact mechanics based on the assumption of indentation on flat surface. In reality, however, it is extremely difficult to achieve a perfectly flat surface. Hence, the major challenge in applying nanoindentation to characterize cementitious material is preparing the sample surface. Accuracy of nanoindentation experiments depend on reducing the surface roughness to a tolerable level without causing any damage to the sample. A detailed description of the development of a surface preparation technique and the use of atomic force microscopy to study polished surfaces is provided in Chapter 4.

Chapter 5 provides a description of the nanoindentation experiments performed in this work to determine local mechanical properties of different phases of the cement paste microstructure. The experiments were conducted in two phases. The first phase involved use of a local probe in atomic force microscopy. In the second phase of the experiments, a special type of nanoindenter from Hysitron, called Triboindenter, was used. A Triboindenter combines principles of nanoindentation with atomic force microscopy.

In Chapter 6, nanoindentation experiments on the interfacial transition zone (ITZ) are described. In concrete, the ITZ is believed to be the weakest zone. This region develops around

cement paste aggregates due to the so called "wall effect" [4]. It is widely accepted that the properties of the ITZ controls failure and has to be considered to predict overall performance. However, due to the complex nature of the microstructure and limitations of experimental techniques, direct experimental measurements of local nanomechanical properties of the ITZ is extremely difficult. This chapter summarizes one of the first, and most complete effort.

It is well recognized that the use of mineral admixture such as silica fume and fly ash enhances strength and durability of concrete. Chapter 7 provides a detailed discussion on how addition of silica fume and nanosilica affect nanoscale local mechanical properties of paste. From macroscopic tests, silica fume was found to improve properties of the ITZ in concrete. Research presented in this chapter shows how addition of silica fume has greater effects on mechanical properties of the ITZ than on bulk paste in concrete.

In Chapter 8, the theoretical framework to solve contact problems on a rough surface is presented, followed by the development of a statistical technique to determine the actual area. In earlier experiments, indentation has been considered as contact between an indenter and infinite half-space where the initial surface is perfectly flat. Consequently, contact between the indenter and the sample was continuous within the nominal contact area and absent outside it. In this chapter, the assumption of continuous contact is relaxed and corresponding analysis for nanoindentation on polished cementitious samples is presented.

Finally, Chapter 9 presents the conclusions drawn in the course of this research and recommendations for future work.

Chapter 2 Literature Review

2.1. Microstructure of Concrete

Concrete is heterogeneous at all length scales as shown in Figure 2.1. It is a mixture of mortar and aggregate with an interfacial transition zone (ITZ) in between. Mortar is again a composite containing sand, cement paste, and ITZ in between. Cement powder, when mixed with water, undergoes a set of reactions to form hydration products. With time, these hydration products in cement paste form a rigid structure which is also heterogeneous in nature. The main phases present in hydrated cement paste microstructure can be listed as, 1) calcium silicate hydrate, C-S-H; 2) calcium hydroxide, CH; 3) ettringite, 4) monosulfate, 5) unhydrated cement particle, and 6) air voids. Macroscopic properties of cementitious materials is governed by the properties of these phases, demanding detailed knowledge of the morphology and mechanical properties of each phases.

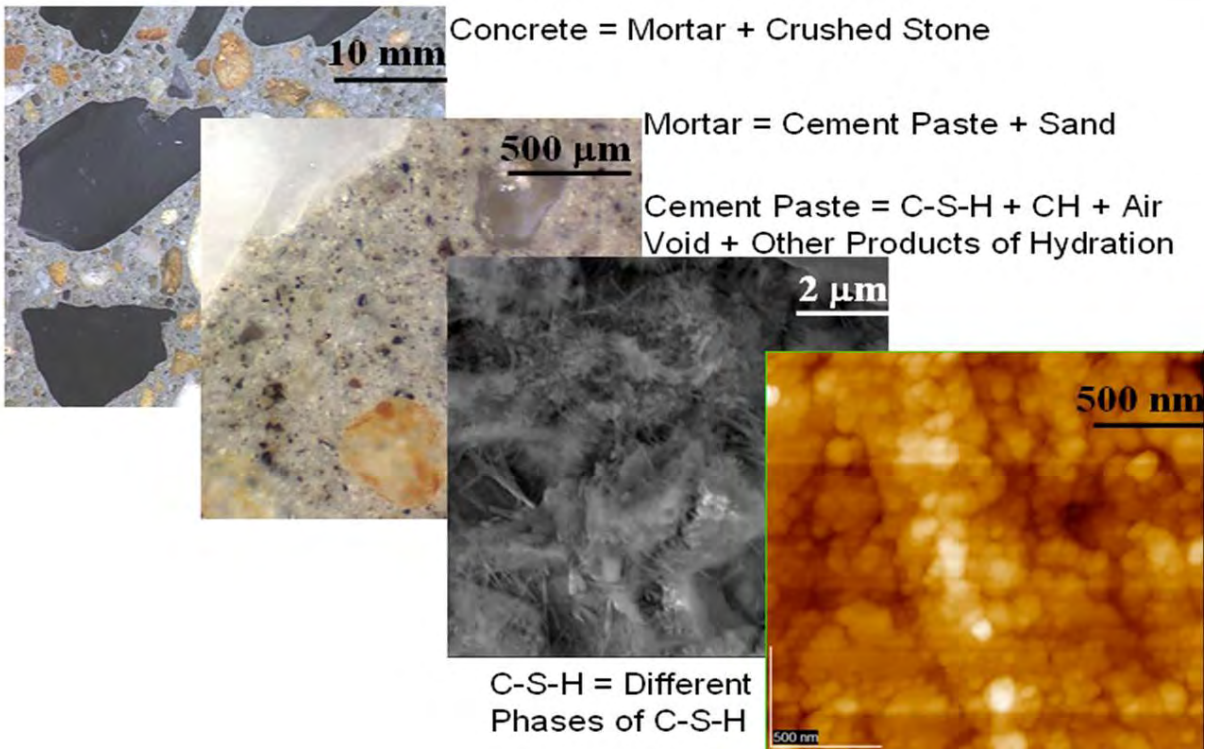

Figure 2.1. Concrete at Different Length Scale

2.2. Calcium Silicate Hydrate, C-S-H

C-S-H is the main hydration product that accounts for 50-70% of the volume and contributes to the macroscopic properties the most. The dashes indicate that no particular composition is implied. Over the last 100 years, researchers have used various experimental techniques to characterize this material. The goal was to come up with a description of the morphology and develop a relationship between the microstructure and macroscopic properties. As early as in 1887, Le Chatelier described a gel-like morphology of the C-S-H phase (from Neville [57]). Taylor [29] compared the atomic structure of C-S-H in cement paste with many known crystalline calcium silicate hydrates. He suggested that the C-S-H structure is similar to that of the naturally occurring minerals

Tobermorite and Jennite. He also suggested that there are some semicrystalline calcium silicate hydrate that are intermediate in structure between the crystalline Tobermorite, Jennite, and C-S-H gel. Two types of semicrystalline C-S-H, C-S-H(I) and C-S-H(II), has been reported to have a layered structure of CaO_2 with linear silicate of 'dreierketten' chains on each side. It has also been found from nuclear magnetic resonance (NMR) spectroscopy that C-S-H consists of dimers and higher polymers, mainly pentamers and octamers. Using scanning electron microscopy (SEM), Diamond [26] identified four morphological types of C-S-H gel visible on fractured surface of hydrated cement paste:

1. Type I: prominent in early ages, elongated fibrous material where fibers may be up to 2μm long

2. Type II: normally early products forming honeycombs or reticular networks

3. Type III: prominent in oldr paste which is more massive and apparently consisting of tightly packed grains up to 300 nm across

4. Type IV: late product, also called inner product which is more massive and featureless.

Though SEM images of fractured surfaces have provided valuable information, these surfaces are inherently unrepresentative of the bulk microstructure. Furthermore, dehydration in the high vacuum chamber in SEM affects the morphology. The use of backscattered electron imaging is being used by many researchers on polished samples and the use of a wet cell is adapted to stop dehydration inside the SEM [36]. Jennings [36] correlated various morphological features with the reactions occurring during various stages. He mentioned that, at early stage, an "early product", appears as a thin foil which can exfoliate and crumple into needles. This process slowly continues throughout stage II (induction period) of hydration. During stage III (acceleration period) and

stage IV (deceleration period) of hydration, a colloidal "middle product" forms, later developing into either Type 1 (fibers) or Type 3 (interleaved thin foils). During stage IV, Type 4, the "inner product" develops which has a fine grain appearance. Many experiments suggest the existence of two different morphological entities of C-S-H. Early studies with light microscopy of thin sections suggested this, which was later supported by means of high resolution TEM of ground and dispersed samples, X-ray mapping of flat polished sections, Newton scattering, and other techniques. These two types of C-S-H have been referred in literature as phenograins - groundmass, outer product - inner product [70], low density - high density [37, 39], or middle product - late product [29]. Recent TEM study by Richardson [70] showed a distinct difference in the morphology of the two types of C-S-H. In another study by Nonat et al. [58] indicated a crystalline nature of C-S-H by Atomic Force Microscopy (AFM) imaging. Recent research using small-angle neutron scattering revealed further morphological information on two different types of C-S-H [1, 2].

2.2.1. Model of C-S-H

Depending on the information available from experimental techniques, many researchers attempted to develop a general model of C-S-H to provide quantitative and qualitative information. The Following sections present a brief overview of different models. The first significant one was the Powers and Brownyard model (as summarized by Taylor [77]) the gives the quantitative calculations of the volumetric proportions in cement based materials. Powers and Brownyard in their model considered the solid phases, either cement or the product of hydrations collectively as

"cement gel". Volumetric proportions of different phases were given by

$$\begin{aligned} V_{cs} &= 0.20(1-p)\xi && \text{Chemical Shrinkage} \\ V_{cp} &= p - 1.32(1-p)\xi && \text{Capillary Pores} \\ V_{cs} &= 2.12(1-p)\xi && \text{Gel Pores} \\ V_{cl} &= (1-p)(1-\xi) && \text{Unhydrated Cement} \end{aligned} \tag{2.1}$$

where ξ is the degree of hydration and p is the initial porosity, i.e. the space initially occupied by water and is given by

$$p = \frac{w/c}{w/c + p_w/p_c} \tag{2.2}$$

where cement mass density, p_c = 3150 kg/m^3 and water mass density, p_w = 1000 kg/m^3. This model concentrates on the gel phase and does not distinguish between two types of C-S-H. It does not incorporate any other product of hydration either. Brunauer considered that the gel particles of the Powers-Brownyard model consisted of either two or three layers of C-S-H which could roll into fibers. According to Brunauer, the specific surface area can be measured by water sorption which gives a value in the region of 200 m^2g^{-1}. Lower value of surface area measured by nitrogen was attributed to the failure of the nitrogen molecule to enter all the pore spaces. Feldman and Sereda [30] described the gel as a three dimensional assembly of C-S-H layers. They mentioned that C-S-H forms subparallel groups which are few layers thick and it has pores of dimensions equal or greater than interlayer spaces. Contrary to Brunauer, they mentioned that the surface area measurement by nitrogen is the true one and not by water [18, 19]. Wittmann described hydrated

cement paste as a xerogel, that consists of separate particles. No internal structure was assumed for these particles and the state of structural water in spaces between particles were emphasized. In this model C-S-H was treated as a single phase. The Jennings and Tennis model [37–39] considers two forms of C-S-H, high density (HD) and low density (LD), and proposes a microstructure that is consistent with surface area measurements and nitrogen sorption. This model provides a means of quantifying the volumetric proportions of all major products of hydration. It is assumed that the surface area measured by nitrogen is contributed mostly by LD C-S-H. It is also assumed that the pores in HD C-S-H are not accessible to nitrogen, while only some of the pores in LD C-S-H are accessible. The model postulates that C-S-H has an elementary solid phase of characteristic size of 4.2 nm. The two types of C-S-H have the same fundamental building block, referred as globule, which are packed differently. The gel porosity of LD C-S-H is reported roughly as 37%, so the packing density is 0.63, which is similar to the random close packing, whereas the gel porosity of HD C-S-H is reported as 24%, meaning the packing density is 0.76, which is similar to the highest possible density of an ordered lattice of spheres.

2.3. Experimental Determination of Mechanical Properties of Different Phases

Modeling of microstructure is a promising approach to predict macroscopic properties and it requires knowledge of mechanical properties of the residual clinker phases, hydrated phases, aggregates, interfacial transition zone and all other phases that may present such as fibers. Many researchers in the past used microindentation or microhardness tests for this purpose. With advances in computation and technical instrumentation, it is now possible to investigate mechanical properties of different phases of concrete microstructure at the nanoscale. This section summarizes

the work done by different researchers using nanoindentation technique in an effort to determine local mechanical properties of cement paste micro- and nanostructure.

Velez et al. [85] reported the elastic modulus and the hardness of pure constituents of Portland cement clinker (C_3S, C_2S, C_3A, C_4AF) at the microscopic scale by nanoindentation. Researchers have used a Berkovich indenter to make the indents and used the Oliver and Pharr method, which is described in Section 3.4.1, to determine the elastic properties. To make each indent, multiple cycles of loading and unloading with a hold period to eliminate creep effects were used. Typical indentation depths in this study are about 300 nm-500 nm which corresponds to a maximum indentation load in the range of 40 mN-50 mN. A Poisson's ratio of 0.3 was assumed for all constituents and the average values of the elastic modulus and hardness with standard deviation is shown in Table 2.1 and Table 2.2. The standard deviation for the elastic modulus is within 7% except for

	C_3S	**C_2S**	**C_3A**	**C_4AF**	**Alite**	**Belite**
E(GPa)	**135**	**130**	**145**	**125**	**125**	**127**
S.D.	**7**	**20**	**10**	**25**	**7**	**10**

Table 2.1. Elastic Moduli (E) of Calcium Silicates, Calcium Aluminate and Calcium Aluminoferrite Present in Portland Cement clinker [85]

	C_3S	C_2S	C_3A	C_4AF	Alite	Belite
H(GPa)	8.7	8.0	10.8	9.5	9.2	8.8
S.D.	0.5	1.0	0.7	1.4	0.5	1.0

Table 2.2. Hardness (H) of Calcium Silicates, Calcium Aluminate and Calcium Aluminoferrite Present in Portland Cement Clinker [85]

C_2S and C_4AF which the researchers attributed to the generation of microcracks in the C_2S matrix during processing and microcracking in C_4AF during indentation. The researchers also determined elastic modulus of bulk samples which is an integrated response of the intrinsic elastic modulus of

the solid and porosity of the sample and compared the extrapolated modulus for zero porosity with the nanoindentation data.

In another study by Ulm et al., nanoindentation on cement paste sample was performed to provide input for a continuum mechanics model [81]. A statistical representative area of C-S-H matrix was chosen for indentation where depth of indentation were in the range of 300-500 nm. Authors mentioned that the elastic properties determined using Oliver and Pharr method and the duel indentation method were in very good agreement (S.D. $< \pm 1\%$). Frequency histograms of the elastic modulus obtained from nanoindentation on non-degraded and calcium leached (degraded) cement paste were studied to determine volume fraction of different phases. According to the authors, a bimodal distribution fitted to the nanoindentation data represents the existence of two types of C-S-H compounds, a low stiffness C-S-H phase (C-S-H_a) and a high stiffness C-S-H (C-S-H_b), at a scale of $10^{-6} - 10^{-7}$ m. Table 2.3 summarizes the mean elastic modulus values calculated. Authors mentioned that the mean elastic modulus for non-degraded material almost coincide with the indentation results reported by Acker on ultra high performance concrete produced at a very low water to cement ratio (w/c = 0.18) and with admixtures. They suggested that the properties obtained by nanoindentation are intrinsic to all types of cement-based materials which do not depend on the w/c ratio or admixtures, although they mentioned that additional tests are required to confirm this. The researchers concluded that the volumetric proportions of the two types of C-S-H remain approximately constant even after calcium leaching. For the considered cement paste, the estimated volume fractions of low stiffness C-S-H_a and high stiffness C-S-H_b is reported as 70% and 30%. They also estimated the volume fraction for w/c = 0.5, using the Jennings and

	Elastic Modulus(GPa)		Residual
	Nondegraded	Degraded	Value(%)
CH	**38.0±5**	**-**	**-**
C-S-H$_a$	**21.7±2.2**	**3.0±0.8**	**14**
C-S-H$_b$	**29.4±2.4**	**12.0±1.2**	**41**

Table 2.3. Elastic Modulus of Individual Constituents of Cement Paste Microstructure Obtained by Nanoindentation [81]

Tennis model which are in very good agreement. Ulm et al. applied reverse micromechanical model to obtain indentation modulus of solid C-S-H particles using the self-consistent method, which is commonly used for polycrystalline materials. The modulus of C-S-H particles obtained from the indentation modulus of LD C-S-H is 65.9 GPa and the value obtained from HD C-S-H is 62.9 GPa. The closeness of these two values obtained hints that the two types of C-S-H comprises the same solid phase packed in different packing densities. This observation is in good agreements with Jennings' model of C-S-H.

Hughes and Trtik [35] used depth sensing nanoindentation to determine mechanical properties of different phases with a goal, similar to that of the previous researchers, to provide better inputs for microstructural modeling of cementitious materials. Cement paste samples with w/c ratio of 0.45 were tested. Nanoindentation was performed over a regular grid of 50 positions on the sample, each spaced at 50 μm. In this study, authors emphasized on the need for imaging the location of each indents to determine the phase present at the site. To serve this purpose, the sample was imaged using a field emission scanning electron microscope (FESEM). Back scattered electron (BSE) imaging and quantitative energy dispersive spectrometer (EDS) analysis were used to determine the compositions of the phases that were indented point-by-point. This process seems to be

time consuming and only initial results are available so far in open literature. Table 2.4 summarizes the results reported by the authors.

Category	E	H	S.D.E	S.D.H	n
Clinker	**45.32**	**2.75**	**30.12**	**2.89**	**10**
Inner CSH	**22.97**	**0.88**			**1**
Outer CSH	**25.74**	**0.88**	**10.84**	**0.36**	**4**
Calcium hydroxide	**29.05**	**1.00**	**9.95**	**0.43**	**6**
Mixed CSH and clinker	**46.07**	**2.08**	**33.58**	**2.59**	**9**
Mixed CH and clinker	**26.61**	**1.04**	**10.86**	**0.51**	**3**
Edge CSH and CH	**30.75**	**1.52**			**1**
CH and CSH	**26.53**	**0.91**	**8.00**	**0.31**	**12**

Moduli have been calculated from the unloading in load-displacement graph

Table 2.4. Results of the Depth-Sensing Nanoindentation Experiment [35]

Nonat [58] used atomic force microscopy (AFM) to investigate the structure of C-S-H at the nanoscale and performed nanoindentation hardness tests with a modified AFM tip. Indentation depth was as low as 1 nm. He used single crystal calcite in a concentrated sodium silicate solution (pH = 14.2) to obtained a C-S-H layer in the form of identical nanoparticles ($60 \times 30 \times 5nm^3$). The C-S-H covered single crystal calcite was immersed in calcium hydroxide solutions of different concentrations to obtain C-S-H with different Ca/Si ratios. From the atomic resolution AFM image of the crystalline C-S-H layer, surface cell parameters ($\overrightarrow{a}$, $\overrightarrow{b}$)were determined for different Ca/Si ratio. AFM nanoindentation was used to obtain information in the perpendicular direction, $\overrightarrow{c}$ to the C-S-H layer. They have seen an increase in modulus with the increase in calcium concentration which is a consequence of decrease in interlayer spacing. The researcher reported an elastic modulus of 88.9 ±4.9 Gpa at a calcium concentration of 0.36 mmol/l which can be compared to the elastic modulus of tobermorite. Both the elastic modulus and cell parameters show a discontinuity

at a calcium concentration of 8 mmol/l which, as suggested by the researchers, is due to a possible phase transformation.

Bittnar et al. [56] performed nanoindentation on cement paste sample with indentation depth varying from 400 nm to 2500 nm. They reported that both the modulus and the hardness values decrease with the increase in indentation depth and approaches values similar to macroscopic tests results on large-scale specimens. Bittner et al. discussed the possible size effect due to the nucleation of dislocations within the plastic zone under the indentation area as a possible explanation for this behavior. However, it should be noted that it is impossible to indent just one phase when the indentation depth is too large. Therefore, it may be the case that the modulus values obtained from indents with relatively small indentation depths (around 400 nm) represent properties of the microstructure whereas larger indentation depths will tend to capture properties of the cement paste as a whole.

Chapter 3 Contact Mechanics and Nanoindentation

3.1. Introduction

Stresses developing from contact between two elastic bodies are of considerable importance in different fields of science and engineering. Contact stresses are highly concentrated near the point of contact, but decrease rapidly with distance. For two non-conforming bodies in contact, stresses under sufficiently small deformation can be computed for by assuming each body as a semi-infinite elastic solid bounded by a plane surface i.e. an elastic half-space. In such situations, dimensions of contact areas are small compared to the dimensions of the contacting bodies and stress distributions do not critically depend on the shape of the bodies away from the point of contact or the precise support conditions. This chapter provides a review of the theory for computing stresses, area of contact, and the deformation of bodies in contact.

3.2. Analysis of Elastic Stress Fields

Two non-conforming bodies, when brought into contact, touch initially at a single point or along a line. With the increase in load, they deform in the vicinity of their first contact point, making contact over an area. But this area is still small compared to the dimensions of the two bodies. The theory of contact mechanics predicts the shape of the contact area and how it grows in size with increase in load, and stress and deformation of both the bodies in the vicinity of the contact region.

3.2.1. Line Loading

The two-dimensional problem of a uniformly distributed concentrated force acting on a line along the y-axis was first solved by Flamant [40]. Figure 3.1 shows the distribution of stresses within the specimen due to a concentrated force of intensity P per unit length. Radial stresses acting towards the point of contact at any point at a distance r, can be written as:

$$\sigma_r = -\frac{2P}{\pi}\frac{\cos\theta}{r} \tag{3.1}$$

$$\sigma_\theta = \tau_{r\theta} = 0 \tag{3.2}$$

A more general two-dimensional problem with arbitrary traction on the surface can be treated as a combination of such line loads. The theory of superposition can be applied to determine stresses and displacements. Eq. 3.3 and 3.4 gives the displacement of the surface along the x and the z

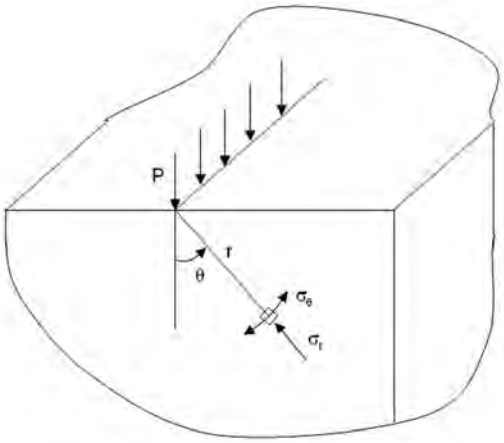

Figure 3.1. Line Contact on Elastic Half Space

direction due to an applied traction $p(x)$.

$$\frac{\partial \bar{u}_x}{\partial x} = -\frac{(1-2\nu)(1+\nu)}{E} p(x) \tag{3.3}$$

$$\frac{\partial \bar{u}_z}{\partial x} = -\frac{2(1-\nu^2)}{\pi E} \int_{-b}^{a} \frac{p(s)}{x-s} ds \tag{3.4}$$

3.2.2. Point Loading

The classical approach for the determination of stresses and deformations due to traction applied to a closed area S on the surface begins with the analysis of a point contact. Boussinesq and Cerruti [40] used the theory of potential to solve point loading of an elastic half-space. Any contact configuration, such as indentation with a cylindrical flat punch or a spherical indenter, can be represented by multiple point loads of the appropriate intensity on the specimen surface. The stress distribution within the specimen is the summation of the stress fields due to each point load. Figure 3.2 shows the stress and displacement produced by a concentrated normal load P at the origin. Recognizing that the system is axi-symmetric, Timoshenko and Goodier [78] used

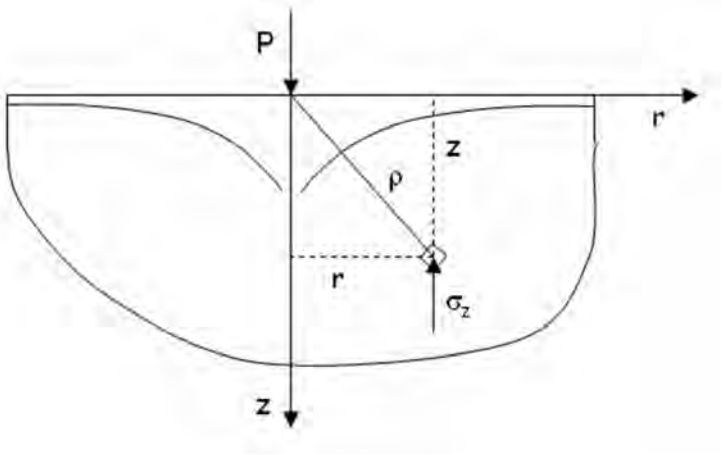

Figure 3.2. Point Contact on Elastic Half Space

polar coordinate to solve the problem. Eq. 3.5 represents the radial displacement u_r and Eq. 3.6 represents the vertical displacement u_z along the z axis.

$$u_r = \frac{P}{4\pi G}\left[\frac{rz}{\rho^3} - (1-2\nu)\frac{\rho - z}{\rho r}\right] \tag{3.5}$$

$$u_z = \frac{P}{4\pi G}\left[\frac{z^2}{\rho^3} - \frac{2(1-\nu)}{\rho}\right] \tag{3.6}$$

where ρ is the distance of the point of interest from the point contact and is given by

$$\rho = (x^2 + y^2 + z^2)^{1/2} \tag{3.7}$$

Similarly, the radial and the vertical displacements at the surface of the solid, i.e. at $z = 0$, can be written as

$$\bar{u}_r = -\frac{(1-2\nu)}{4\pi G}\frac{P}{r} \tag{3.8}$$

$$\bar{u}_z = \frac{(1-\nu)}{2\pi G}\frac{P}{r} \tag{3.9}$$

From Eq. 3.9, it can be observed that the surface profile of the deformed solid is a rectangular hyperboloid. The deformed profile is asymptotic to the original surface at a large distance from the point load. Furthermore, the displacement is theoretically infinite under the load. Applying superposition, the displacement of any point due to an arbitrary pressure $p(s, \phi)$ over an area S can be determined by

$$\bar{u}_z = \frac{(1-\nu^2)}{\pi E}\int_S\int p(s,\phi)dsd\phi \tag{3.10}$$

In principal, so-called Boussinesq solution [40] allows the stress distribution to be determined for any distributed pressure within a contact area using the principle of superposition. However, in practice, classical theory can successfully predict the closed form solution for stresses only in simple cases. More sophisticated analytical techniques were developed later to overcome some of the difficulties of the classical approach.

3.2.3. Description of Smooth Non-Conforming Surfaces in Contact

In classical contact mechanics, surfaces in contact are considered to be topographically smooth on both micro and macro scale. On the micro scale, this implies absence or disregard of small surface irregularities or surface roughness that leads to discontinuous contact and major local variation in contact pressure. On the macro scale, surfaces are assumed to be continuous up to the second derivative and may be expressed as

$$z_1 = A_1 x^2 + B_1 y^2 + C_1 xy + \dots \tag{3.11}$$

Here the higher order terms in x and y are neglected. Then the separation between two approaching surfaces can be written as $h = z_1 - z_2$ or

$$h = Ax^2 + By^2 + Cxy \tag{3.12}$$

Consider the two bodies shown in Figure 3.3 with two corresponding surface points $S_1(x, y, z_1)$ and $S_2(x, y, z_2)$. The separation between them before deformation is represented by Eq. 3.12 where C can be set to zero with the proper choice of axes. Under the application of load, two bodies move towards each other by displacements δ_1 and δ_2 respectively. If the solids do not deform, their profile would overlap which is shown by the dotted lines in Figure 3.3. However, if they deform by an amount $\bar{u}_{z1}$ and $\bar{u}_{z2}$ respectively and if S_1, S_2 are coincident within the contact surface then,

$$\bar{u}_{z1} + \bar{u}_{z2} + h \;\; = \;\; \delta_1 + \delta_2 = \delta \tag{3.13}$$

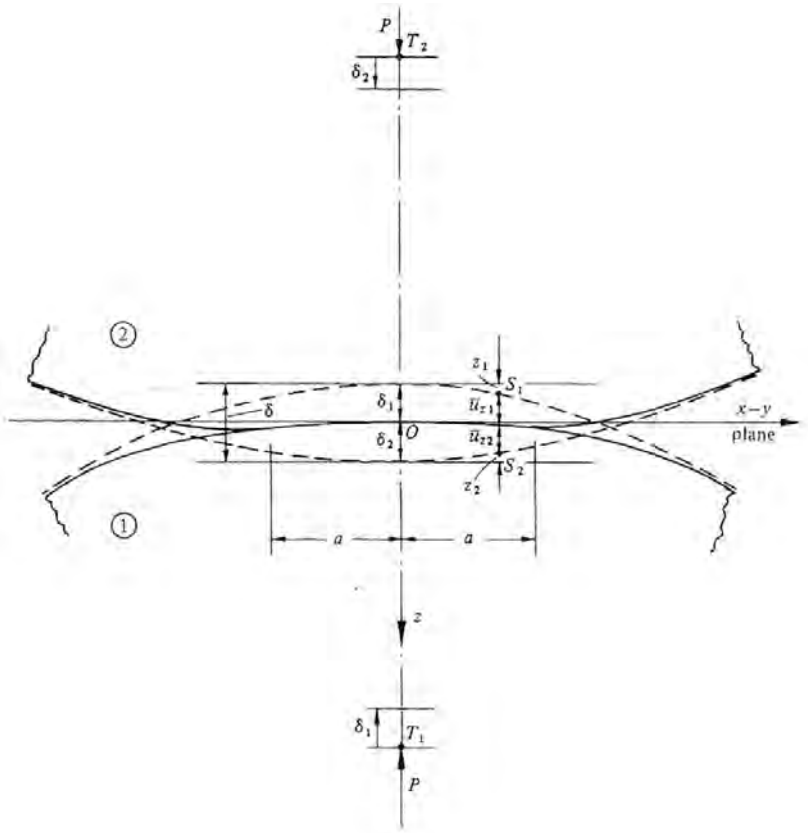

Figure 3.3. Schematic Diagram of Two Smooth Non-Conforming Surfaces in Contact [40]

Therefore, using Eq. 3.12 the condition for contact can be written as,

$$\bar{u}_{z1} + \bar{u}_{z2} \quad = \quad \delta - Ax^2 - By^2 \tag{3.14}$$

where x and y are the common coordinates of S_1 and S_2 projected onto the $x - y$ plane. The condition for the points to lie outside the area of contact can be written as

$$\bar{u}_{z1} + \bar{u}_{z2} \quad > \quad \delta - Ax^2 - By^2 \tag{3.15}$$

3.2.4. Hertz Theory

The credit for developing the first satisfactory analysis of the stress at the contact of two elastic solids is attributed to Hertz. The assumptions made in the Hertz's theory [40] are summarized below:

i) The surfaces are continuous and non-conforming, i.e. $a << R$ where a is the dimension of the contact area and R is the relative radius of curvature of the two bodies.

ii) The strains are small, i,e. $a << R$.

iii) Solids can be considered as elastic half-space, i.e. $a << R_1$, $a << R_2$, and $a << l$, where R_1 and R_2 are radius of curvature of the bodies and l is the significant dimension of the bodies.

iv) Surfaces are frictionless.

The boundary conditions are given by,

a) Displacements and stresses satisfy differential equations of equilibrium for elastic bodies and stresses vanish at a great distance from the contact surface.

b) At the surface of the bodies, the normal pressure is equal and opposite within the elliptical contact area and zero outside.

c) The distance between the surfaces of two bodies is zero within the contact area and greater than zero outside.

d) The integral of pressure distribution within the contact area is equal to the force acting between the two bodies.

In case of contact between two solids of revolution with relative radius of curvature R, the condition of contact given in Eq. 3.14 can be written as

$$\bar{u}_{z1} + \bar{u}_{z2} = \delta - \left(\frac{1}{2R}\right) r^2 \tag{3.16}$$

where $A = B = \frac{1}{2}\left(\frac{1}{R_1} + \frac{1}{R_2}\right) = \frac{1}{2R}$. The pressure distribution proposed by Hertz is

$$p = p_0 \left\{1 - \left(\frac{r}{a}\right)^2\right\}^{1/2} \tag{3.17}$$

which produces normal displacements

$$\bar{u}_z = \frac{1-\nu^2}{E}\frac{\pi p_0}{4a}(2a^2 - r^2) \tag{3.18}$$

In Eq. 3.18 E^* is related to the elastic modulus and Poisson's ratio of the two bodies as below:

$$\frac{1}{E^*} = \frac{1-\nu_1^2}{E_1} + \frac{1-\nu_2^2}{E_2} \tag{3.19}$$

Substituting S^* in the expressions for $\bar{u_{z1}}$ and $\bar{u_{z2}}$ we get,

$$\frac{\pi p_0}{4aE^*}(2a^2 - r^2) = \delta - \left(\frac{1}{2R}\right) r^2 \tag{3.20}$$

This yields an expression for the radius of contact circle, a and the approach of the two bodies δ as given below:

$$a = \frac{\pi p_0 R}{2E^*} \tag{3.21}$$

$$\delta = \frac{\pi a p_0}{2E^*} \tag{3.22}$$

Now, the total force acting on the solids can be written as

$$P = \int_0^a p(r) 2\pi r dr = \frac{2}{3} p_0 \pi a^2 \tag{3.23}$$

Combining Eq. 3.21, Eq. 3.22 and Eq. 3.23, we can write

$$a = \left(\frac{3PR}{4E^*}\right)^{1/3} \tag{3.24}$$

$$\delta = \frac{a^2}{R} = \left(\frac{9P^2}{16RE^{*^2}}\right)^{1/3} \tag{3.25}$$

$$A = \pi a^2 = \pi \frac{\delta}{R} \tag{3.26}$$

$$p_0 = \frac{3P}{2\pi a^2} = \left(\frac{6PE^{*^2}}{\pi^3 R^2}\right)^{1/3} \tag{3.27}$$

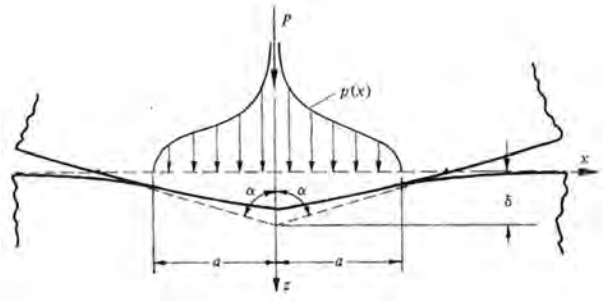

Figure 3.4. Indentation by a Blunt Wedge [40]

3.2.5. Non-Hertzian Contact: Blunt Wedge and Rigid Cone Indenters

The Hertz theory as discussed in the previous section, is restricted to smooth and continuous surfaces profiles so that the stresses are finite everywhere. But the stresses and deformations due to a rigid conical indenter are of significant practical interest since it can approximate different indenters used in hardness testing. A blunt wedge or a rigid cone indenter introduces a sharp discontinuity in the slope of the profile within the contact area. In case of a two-dimensional wedge indenting a flat surface, as shown in Figure 3.4, elastic solutions for a half-space can be used for both the indenter and the flat surface if the contact strip is small compared to the size of the two bodies. The normal displacements can be related to the shape of the wedge (cone semi-angle α) by

$$\bar{u}_{z1} + \bar{u}_{z2} = \delta - \cot\alpha|x|, \qquad -a < x < a \tag{3.28}$$

Neglecting friction, the normal force and the pressure distribution can be written as

$$\frac{2}{\pi E^*}\int_{-a}^{a}\frac{p(s)}{x-s}ds = (\text{sign } x)\cot\alpha \tag{3.29}$$

Normal force and pressure distribution due to a rigid cone indenter with cone semi-angle α can be written as

$$p(x) = \frac{E^* \cot \alpha}{2\pi} \ln \left\{ \frac{a + (a^2 - x^2)^1/2}{a - (a^2 - x^2)^1/2} \right\} = \frac{E^* \cot \alpha}{\pi} \cosh^{-1}(a/x) \tag{3.30}$$

and

$$P = \frac{1}{2} \pi a^2 E^* \cot \alpha \tag{3.31}$$

From Eq. 3.30, it is clear that the pressure distribution at the apex becomes infinite. The displacement of the original surface in z direction can be written as

$$u_z = \left(\frac{\pi}{2} - \frac{r}{a} \right) a \cot \alpha \qquad r \leq a \tag{3.32}$$

3.3. Nanoindentation

Nanoindentation is a technique that has been successfully used to obtain mechanical properties of different phases of cement paste microstructure. In any indentation technique, one material of known properties is used to touch the material of interest whose mechanical properties such as elastic modulus and hardness are unknown.

3.4. Mathematical Formulation to Determine Mechanical Properties from Nanoindentation

In nanoindentation, an indenter is pushed into a sample while load applied by the indenter is plotted continuously with the displacement of the indenter into the sample. This kind of plot is commonly known as the load-indentation or simply, the p-h plot. The data obtained is then

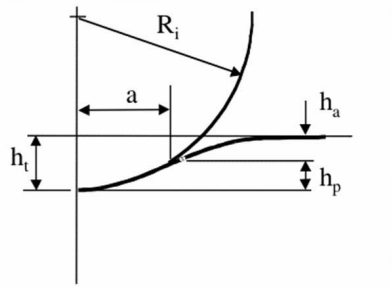

Figure 3.5. Schematic of contact between a Rigid Indenter and a Flat Specimen[31]

analyzed to estimate elastic modulus, E and hardness, H. This analysis procedure is essentially based on the solution of elastic contact problem developed by Boussinesq and Hertz [40] in late 19th century. Figure 3.5 shows a schematic of contact between a rigid sphere and a flat surface. As discussed in Section 3.2.4, Hertz found that the radius of the circle of contact, a is related to the indenter load P, the indenter radius R, and the elastic properties of the contacting materials. Hence, we can rewrite Eq. 3.24 as,

$$a^3 = \frac{3}{4}\frac{PR}{E_r} \tag{3.33}$$

where E_r combines the elastic modulus of the indenter and the specimen and is often referred to as the “reduced modulus", the “combined modulus" or the “indentation modulus". Replacing E^* in Eq. 3.19 by E_r, we can relate it to the modulus of the indenter, E' and elastic modulus of the specimen, E by

$$\frac{1}{E_r} = \frac{1-\nu^2}{E} + \frac{1-\nu'^2}{E'} \tag{3.34}$$

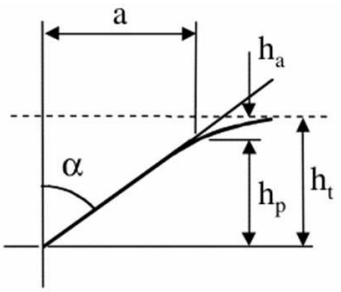

Figure 3.6. Geometry of Contact with Conical Indenter[31]

where ν is the Poisson's ratio of the specimen and ν' is the Poisson's ratio of the indenter. In terms of total depth of penetration, h_t, we can also write

$$P = \frac{4}{3} E_r R^{1/2} h_t^{3/2} \tag{3.35}$$

For a conical indenter, we can rewrite Eq. 3.31 to relate the radius of circle of contact to the indenter load as,

$$P = \frac{\pi a}{2} E_r a \cot \alpha \tag{3.36}$$

where α is the cone semi-angle as shown in the Figure 3.6 and $a \cot \alpha$ is the depth of indentation, $h(p)$, measured at the circle of contact. From this we get,

$$P = \frac{2E \tan \alpha}{\pi} h_t^2 \tag{3.37}$$

In indentation test, the most common types of indenters are pyramidal indenters, among which two widely used are the four-sided Vickers indenter and the three-sided Berkovich indenter. Pyramidal indenters are generally treated as conical indenters with a cone angle that provides the same area

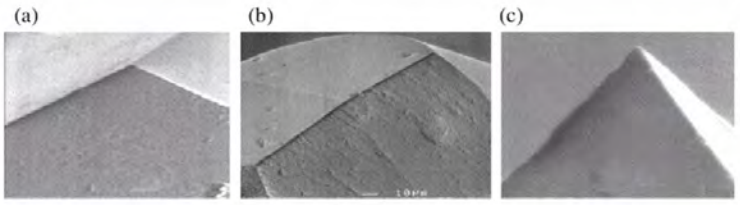

Figure 3.7. Images of Different Indenter Tip, (a) Berkovich, (b) Knoop and (c) Cube Corner[31]

to depth relationship as the actual indenter in question. This allows the use of convenient axi-symmetric elastic solution. Area of contact, as a function of the depth of the circle of contact for some common indenters, are given in Table 3.1. Another major contribution in this field was

Indenter type	Projected Area A	Semi-angle θ(deg)	Effective Cone angle α(deg)	Intercept factor	Geometry correction factor β
Sphere	$\pi 2Rh_p$	N/A	N/A	0.75	1
Berkovich	$3\sqrt{3}h_p^2 \tan^2\theta$	65.3°	70.2996°	0.75	1.034
Vickers	$4h_p^2 \tan^2\theta$	68°	70.32°	0.75	1.012
Knoop	$2h_p^2 \tan\theta_1 \tan\theta_2$	$\theta_1 = 86.25°$, $\theta_2 = 65°$	77.64°	0.75 0.75	1.012 1.012
Cube Corner	$3\sqrt{3}h_p^2 \tan^2\theta$	35.26°	42.28°	0.75	1.034
Cone	$\pi h_p^2 \tan^2\alpha$	α	α	0.72	1

Table 3.1. Contact Area for Different Indenter Geometries[31]

made by Sneddon [74, 75]. For any punch geometry that can be described as a solid of revolution of a smooth function, he showed that the general relationships among the load and displacement can be written as

$$P = \alpha h^m \tag{3.38}$$

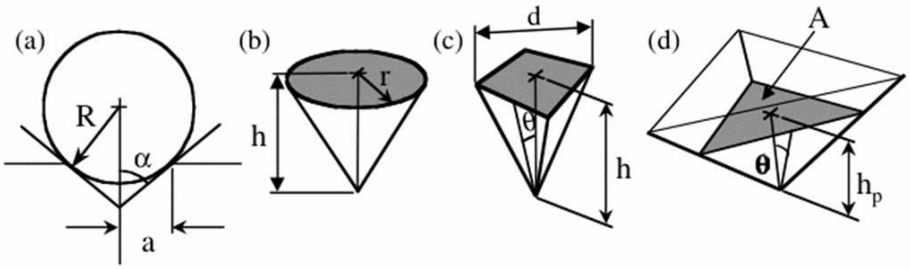

Figure 3.8. Indentation Parameters for (a) Spherical, (b) Conical, (c) Vickers and (d) Berkovich Indenter[31]

where P is the indenter load, h is the elastic displacement of the indenter, α and m are constants. For a flat cylindrical indenter, $m = 1$, for cones, $m = 2$, for spheres in the limit of small displacements, and for paraboloids of revolution, $m = 1.5$

In the early 1970's, Buylchev, Alekhin, Shorshorov [40] used instrumented microhardness testing machines to obtain a load-displacement plot and analysed the data using the following equation which is known as Buylchev-Alekhin-Shorshorov (BASh) equation [40],

$$S = \frac{dP}{dH} = \beta \frac{2}{\sqrt{\pi}} E_r \sqrt{A} \tag{3.39}$$

In the BASh equation, $S = dP/dh$ is the experimentally measured stiffness for the upper portion of the unloading data and A is the projected area of the elastic contact which was assumed to be equal to the optically measured area of the hardness impression. Though Eq. (3.39) was originally derived for a conical indenter, Buylchev et al. [40] showed that this holds equally well for spherical and cylindrical indenters and speculated that it may as well apply to other geometries. Subsequently, Pharr, and Oliver [59] showed that Eq. (3.39) applies to any indenter geometries that can be described as a body of revolution of a smooth function.

3.4.1. Oliver and Pharr Method

In 1992, Oliver and Pharr[59] proposed a method of analysis based on analytical solutions. This accounts for the curvature in the unloading data. They also mentioned that the direct measurement of the contact area is not always accurate and convenient, and proposed a procedure to determine the contact area based on the depth of indentation and indenter shape function. Such a method is sometimes called “depth-sensing indentation testing". Figure 3.9 shows the cross-section of an indentation. At any time during loading, the total displacement h is written as

$$h = h_c + h_s \tag{3.40}$$

where h_c is the vertical distance along which contact is made, called the contact depth. h_s is the

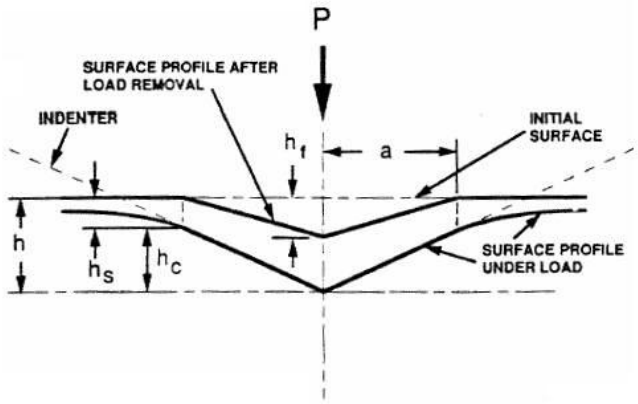

Figure 3.9. Schematic Representation of a Section through an Indenter[59]

displacement of the surface at the perimeter of the contact. At the peak load, P_{max}, displacement is h_{max} and the radius of contact circle is a. During unloading, elastic displacement is recovered and the final depth of the residual hardness impression once the indenter is fully withdrawn is h_f.

The projected contact area, A is determined as a function of the contact depth, h_c i.e.

$$A = F(h_c) \tag{3.41}$$

where the form of the function F has to be established prior to the analysis of data on the sample of interest. From Figure 3.9

$$h_c = h_{max} - h_s \tag{3.42}$$

and for conical indenter

$$h_s = \frac{(\pi - 2)}{\pi}(h - h_f) \quad \text{and} \quad (h - h_f) = 2\frac{P}{S} \tag{3.43}$$

Combining these two equations at peak load, one can obtain

$$h_s = \epsilon\frac{P_{max}}{S} \quad \text{and} \quad \epsilon = \frac{2}{\pi}(\pi - 2) = 0.72 \tag{3.44}$$

where ϵ is the geometric constant. From similar analysis, $\epsilon = 1$ for a flat punch and $\epsilon = 0.75$ for a paraboloid of revolution. So, for flat punch, $h_s = \frac{P_{max}}{S}$ and the contact depth h_c is obtained by the intercept of the initial unloading slope with the displacement axis, which is same as what was used by Doerner and Nix [40].

Area Function and Load Frame Compliance

It is important to determine both load frame compliance and area function accurately to compute elastic properties. Oliver and Pharr [59] modeled the load frame and the specimen as two springs

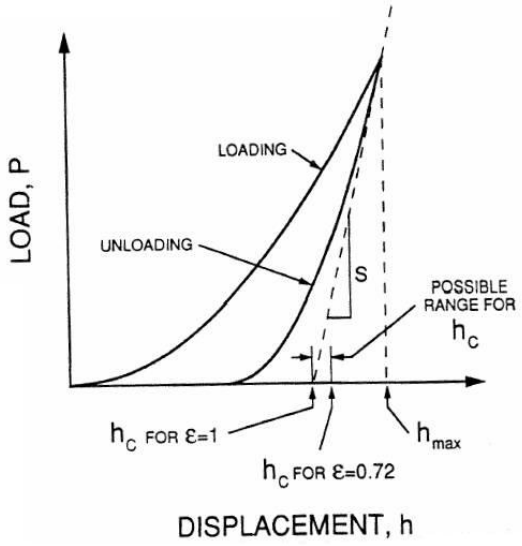

Figure 3.10. Schematic Representation of Load vs Indenter Displacement[59]

in series. Therefore

$$C = C_s + C_f \tag{3.45}$$

where C is the total measured compliance, C_s is the compliance of the specimen and C_f is the compliance of the load frame. Since specimen compliance is the inverse of the stiffness S,

$$C = C_f + \frac{\sqrt{\pi}}{2E_r}\frac{1}{\sqrt{A}} \tag{3.46}$$

For a given material with constant modulus, a plot of C vs $\frac{1}{\sqrt{A}}$ is linear and the intercept is the load frame compliance. It is better to determine the value of C_f from data of large indents so that the second term in Eq. (3.46) becomes small.

As mentioned previously, the perfect area function for a Berkovich indenter is

$$A(h_c) = 3\sqrt{3}h_c^2 \tan^2\theta = 24.5h_c^2 \tag{3.47}$$

To account for imperfect indenter geometry, large indents are made in quartz and corrected area function is determined in the following form

$$A(h_{c)} = 24.5h_c^2 + C_1h_c^1 + C_2h_c^{1/2} + C_3h_c^{1/4} + \ldots + C_8h_c^{1/128} \tag{3.48}$$

Contact area calculated in this way works better in the case of sink-in phenomenon rather than pile-up during indentation [59].

3.4.2. Cheng and Cheng's Method

Cheng and Cheng [13–17] used finite element indentation simulations for a wide variety of elasto-plastic materials with different work hardening characteristics to examine pile-up during indentation with conical indenter and developed a method of analysis that does not require measurement of contact area. Calculating the work of indentation from the $P-h$ plot, authors showed that the ratio of the irreversible work to the work of indentation is a unique function of hardness to indentation modulus ratio. Irrespective of the work hardening characteristics of the material,

$$\frac{W_{tot} - W_{el}}{W_{tot}} \approx 1 - 5\frac{H}{M} \tag{3.49}$$

where the area under the loading curve, W_{tot} is the total work of indentation and the area under the unloading curve, W_{el} is the work recovered during unloading. It can also be written as

$$\frac{4}{\pi}\frac{P_{max}}{S^2} = \frac{H}{M^2} \tag{3.50}$$

where the quantities W_{tot}, W_{el}, P_{max}, S can be calculated from the $P - h$ plot. Using Eq. (3.49) and (3.50) one can calculate hardness and modulus without knowing the contact area. This simulation was originally done on Von-Mises materials with an equivalent cone angle of 68°.

3.4.3. Duel Indentation Technique

The principle of this technique [20] is to perform indentation tests with two different indenter geometries, say a Berkovich and a Cube Corner indenter and express contact area as

$$A_c^{(i)} = \frac{\pi}{4}\left(\frac{S^{exp(i)}}{M}\right)^2 \tag{3.51}$$

where $i = 1$ for Berkovich indenter and $i = 2$ for Cube Corner indenter. $S^{exp(i)}$, $P^{exp(i)}$ and $h^{exp(i)}$ are the stiffness, indentation load, and maximum depth of indentation measured directly from experiment. Assuming that the indentation modulus, M is same in both the experiments,

$$\frac{A_c^{(1)}}{A_c^{(2)}} = \left(\frac{S^{exp(1)}}{S^{exp(2)}}\right)^2 \tag{3.52}$$

and the ratio of hardness from two different experiments can be expressed as

$$\frac{H^{(1)}}{H^{(2)}} = \frac{P^{exp(1)}}{P^{exp(2)}} \times \left(\frac{S^{exp(1)}}{S^{exp(2)}}\right)^2 \tag{3.53}$$

Now, it is proposed to estimate the contact areas ($A_c^{est(1)}$ and $A_c^{est(2)}$) using one particular method, say Oliver and Pharr method, and calculate estimated values of hardness and modulus by the following equations

$$H^{est(i)} = \frac{P^{exp(i)}}{A_c^{est(i)}} \quad \text{and} \quad M^{est(i)} = \frac{2}{\sqrt{\pi}} \frac{S^{exp(i)}}{\sqrt{A_c^{est(i)}}} \tag{3.54}$$

Now, if $M^{est(1)} = M^{est(2)} = M^{exp(1)}$, the estimate is correct otherwise an iterative method can be used to arrive at a better estimate.

Chapter 4 Sample Preparation and Atomic Force Microscopy for Surface Studies

4.1. Introduction

One of the main challenges in applying nanoindentation to characterize cementitious material is preparing the sample surface. Contact mechanics theory used in the analysis of nanoindentation data is based on indentation on a flat surface. It reality, extremely flat surfaces can be achieved only in very rare occasions. For example, mica or graphite can be cleaved along atomic plane to obtain atomically smooth surface. Therefore, the accuracy of nanoindentation experiments on cementitious materials depend on reducing the surface roughness to a tolerable level without causing any damage to the sample. The challenge here is how to minimize both surface roughness and polishing artifact. The question is how rough a surface can be without affecting the results of nanoindentation. This chapter describes the development of a surface preparation technique.

This topic will be revisited in a later chapter when effects of sample roughness on nanoindentation results are discussed.

4.2. Effects of Surface Roughness on Nanoindentation

Classical theory of contact mechanics deals with indentation on an infinite half-space where the initial surface is perfectly flat. In consequence, contact between an indenter and a sample is continuous within the nominal contact area and absent outside. In reality, surface roughness introduces discontinuity in contact and the actual area of contact is a fraction of the nominal contact area. Therefore, the presence of significant surface roughness will cause an overall reduction in measured indentation modulus and indentation hardness. Furthermore, roughness increases scatter in measured indentation modulus and indentation hardness because, in depth sensing nanoindentation, asperities on the surface increase the possibility of false engage of the indenter due to erroneous surface detection. Since measurement of the indentation depth depends on proper detection of the sample surface, roughness introduces error in the measurement. Improper engage may also cause slip of the indenter on the sample surface, causing erroneous drift measurement, and excess scatter in measured indentation modulus and indentation hardness.

4.3. Development of Surface Preparation Technique

This section describes the polishing techniques that were studied to understand the effectiveness of these techniques and estimate the damaging effect that might be associated with them. Finally, an optimized technique was developed to achieve the smoothest possible surface with minimum damage.

4.3.1. Different Polishing Techniques for Surface Preparation

Step 1:

Small specimens with approximate dimensions 10 mm $\times$ 10 mm $\times$ 5 mm were cut out using a diamond saw. A very high rotational speed (3000 rpm) and slow cutting speed was used to minimize specimen damage. Sections were then mounted on metal sample holder using Crystalbond™ 509 adhesive (softening temperature: 71°C) for polishing.

Step 2:

In the second step, Beuhler-Met II paper discs were used for coarse grinding. Samples were polished using paper discs of gradations 34.2 μm, 22.1 μm, 14.5 μm and 6.5 μm successively. Approximate polishing time on each polishing paper was 1 minute. Water was used as the cooling medium during first two coarse grinding steps. The last two steps involved dry polishing. The sample holder was always placed within an annular metal collar. The inside diameter of the collar was flush with the outside diameter of the sample holder. This configuration prevented any wobbling of the sample holder and helped to maintain parallel top and bottom surfaces while polishing. The setup also ensured even polishing of the whole sample surface and minimum tilt of the surface during indentation. Restricting specimen thickness to 5 mm also helped to minimize wobbling of the sample within the metal collar. After polishing on each polishing paper, a Nikon Epiphot Microscope was used to check for effectiveness.

Step 3:

In this step, samples were polished down to 0.1 μm. Four different combinations of polishing, as described below, were performed and the results were compared to select the most efficient one.

a) Polishing was performed using an auto-polisher (Buehler Phonix Beta Grinder/Polisher). Buehler diamond suspensions in water of gradations 6 μm, 3 μm, 1 μm, and 0.1 μm were used as polishing liquids on a Buehler Consumables texmat cloth in four successive polishing steps.

b) Oil based diamond suspensions of gradations 6 μm, 3 μm, 1 μm, and 0.1 μm were used to polish samples on a texmat cloth in the autopolisher.

c) A dimpler (Gatan Model 656 Dimple Grinder) was used with diamond suspensions in oil of gradations 3 μm, 1 μm, and 0.1 μm as polishing liquids.

d) Diamond lapping films from Allied High Tech Products Inc. of gradations 6 μm, and 3 μm were used to polish samples down to 3 μm. In this step, specimens were hand polished using the sample holder and metal collar configuration mentioned earlier to achieve even polishing everywhere on the surface. Next, a diamond suspension in water of 0.1 μm was used to polish specimen on texmat cloth.

Step 4:

Finally, 2 mm thick polished samples were ultrasonically cleaned to remove polishing debris. Both ethanol and water were considered as a cleaning medium. Samples cleaned in water for 1 minute did not show any damage compared to samples cleaned in ethanol. However, cleaning in water for more than 3 minutes caused sample damage. Considering this, it was decided to clean samples in water for 1 minute for the rest of the experiments.

4.3.2. Comparison of Different Polishing Techniques

Figure 4.1 shows scanning electron microscopy (SEM) images of samples polished using the techniques mentioned above. One of the main challenges in polishing a heterogeneous sample is to grind phases of different hardness evenly. In cement paste, unhydrated cement particles are much stiffer than the rest of the paste matrix. As a result, they form islands which stand above the paste matrix and get polished better. The first two fine polishing methods from Step 3 (a and b) were not successful to resolve this problem. However, the last two methods using the dimpler or the fine Diamond lapping film ensured that the highest surfaces of the sample are removed first before grinding the phases of different hardness by equal amount. Instead of using a conventional polishing wheel or an auto-polisher, the effect of using diamond suspension in a dimpler was investigated in the fine polishing method (c). A dimpler is generally used to prepare transmission electron microscopy samples, since it applies less force on the sample and offers more controlled polishing. But the area polished is relatively small and it is difficult to polish the exact same area in successive polishing steps. In method (d), final polish on 0.1 μm helped to remove fine polishing scratches caused by the diamond particles from the lapping film. It was decided not to use a suspension in oil since oil made the samples difficult to clean. Also, a suspension in water did not cause any additional damage compared to a suspension in oil. Considering all these, method (d) was proposed as an optimum surface preparation technique for cementitious materials to achieve a flat surface with minimum possible sample damage.

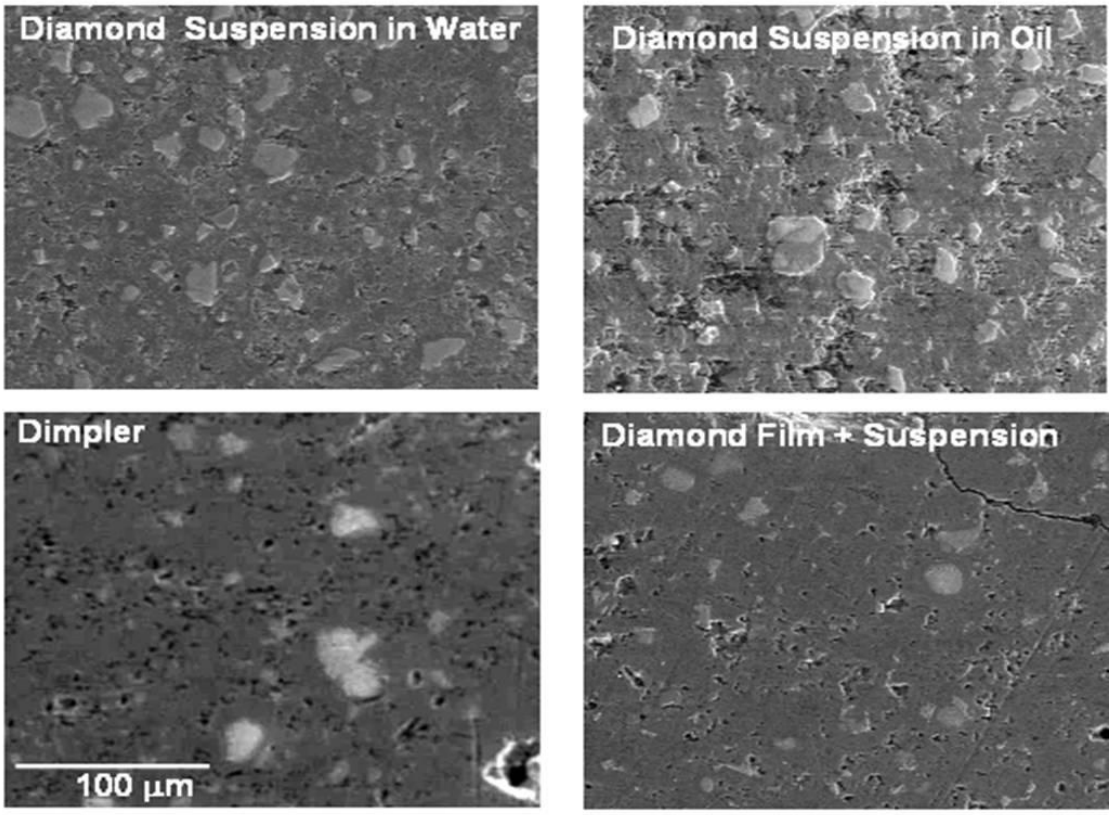

Figure 4.1. Scanning Electron Microscope Image of Cement Paste Samples: Comparison of Different Polishing Techniques

4.4. Use of Atomic Force Microscopy to Investigate Cement Paste Micro- and Nanostructure

Atomic force microscope (AFM) is a very high-resolution type of scanning probe microscope, with demonstrated resolution of fractions of a nanometer. Binnig, Quate and Gerber [5] invented the first AFM in 1986. It is one of the foremost tools for imaging, measuring and manipulating matter at the nanoscale. It can provide local mechanical properties along with nanoscale imaging. This technique is still relatively new to study the nanostructure of cementitious materials [41, 50, 58, 61, 64, 86, 87]. As some examples, AFM has been used to study the surface changes of cement clinker immersed initially in saturated calcium hydroxide solution, followed by water and sucrose

solution [50]; the change in hydrated cement paste microstructure with the exposure to different humidity levels [86]; the carbonation process of calcium hydroxide present in the hydrated cement paste [87] and for imaging the denser microstructure of the cement paste with silica fume or fly ash [61]. To determine local mechanical properties, AFM can be used with a special diamond indenter probe. This has been successfully implemented for different soft materials [69], but in general it only provides qualitative information and proportional values for the elastic modulus [7, 83, 84].

4.4.1. AFM Basics

Atomic force microscopy (AFM) is a particular type of Scanning Probe Microscopy, where a sharp probe (nominal tip radius of the order of 10 nm) located near the end of a cantilever beam scans across the sample surface using piezoelectric scanners. Imaging can be done in normal atmospheric temperature and pressure. It can also be done under liquid. Figure 4.2 shows the schematic of how AFM works. When the tip is brought into proximity of a sample surface, forces between the tip and the sample lead to a deflection of the cantilever. Depending on the situation, forces that are measured in AFM may include mechanical contact forces, Van der Waals forces, capillary forces, chemical bonding, electrostatic forces, and magnetic forces. Changes in the tip-sample interaction are monitored using an optical lever detection system. Figure 4.3 shows how a laser beam is reflected from the back of a cantilever onto a position-sensitive photodiode in the cantilever deflection detection system. The angular displacement of the cantilever results in one photodiode collecting more light than the other photodiode, producing an output signal which is proportional to the deflection of the cantilever. Depending on the mode of operation, a particular operating parameter such as tip-sample force or tip-sample distance is maintained at a constant

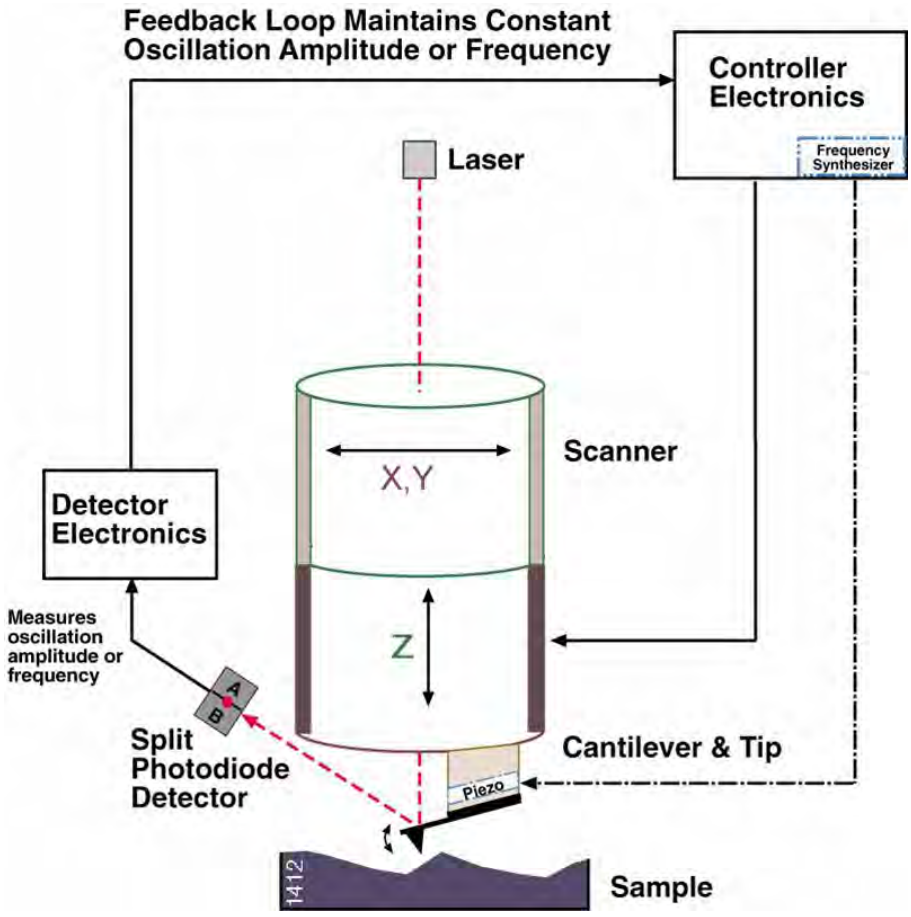

Figure 4.2. Schematic of Atomic Force Microscope

level with a feedback control mechanism between the optical detection system and the piezoelectric scanners. There are three basic imaging modes, contact mode, non-contact mode, and intermittent contact or tapping mode that can be used to produce topographic images of sample surfaces. In contact mode, the probe is essentially dragged across the sample surface. During scanning, as the topography of the sample changes, the z-scanner also moves and adjusts the relative position of the tip with respect to the sample to maintain a constant cantilever deflection. To minimize the amount of applied force used to scan the sample, low spring constant ($k < 1$ N/m) probes are

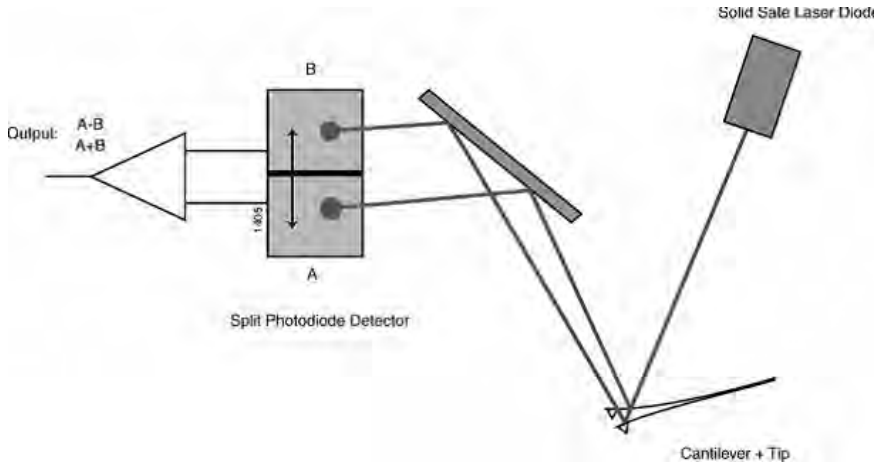

Figure 4.3. Schematic of Cantilever Deflection Detection System

normally used. Figure 4.4 shows an example of a silicon tip that is commonly used in contact mode. While scanning a surface in non-contact mode or tapping mode, the cantilever is oscillated

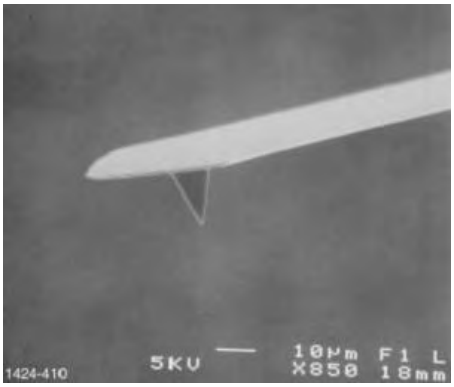

Figure 4.4. Silicon Tip Used in Contact Mode

near its first bending mode resonance frequency (normally of the order of 100 kHz) to reduce or eliminate the damaging forces associated with contact mode. Either a constant amplitude or a constant resonance frequency is maintained through a feedback loop that controls the scanner. The motion of the scanner is used to generate the topographic image. In this mode, the cantilever

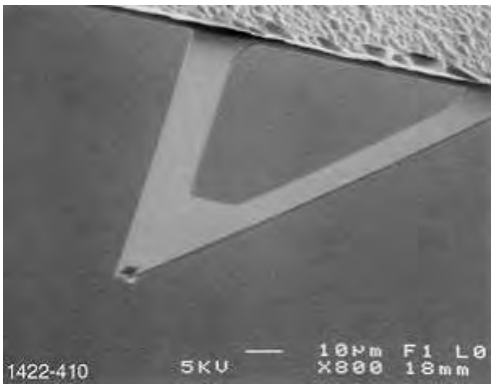

Figure 4.5. Silicon Nitride Tip Used in Tapping Mode

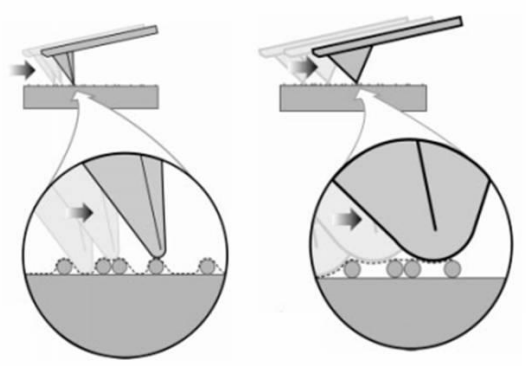

Figure 4.6. Dependence of Resolution on Tip Sharpness

spring constant is normally much higher compared to the spring constant in contact mode to reduce the tendency of the tip to be pulled down to the surface by attractive forces. Figure 4.5 shows a typical tapping mode silicon nitrite tip. Figure 4.6 shows how resolution of image depends on the tip radius and tip sharpness.

AFM has several advantages over a scanning electron microscope (SEM). Unlike an electron microscope which provides a two-dimensional projection or a two-dimensional image of a sample, AFM provides a true three-dimensional surface profile. The benefit of every AFM image is

that it is height encoded. The quantitative information about all the three dimensions of every feature in an AFM image opens up a myriad options for statistical analysis of surface topography on the nanometer scale. These options do not exist in scanning electron and transmission electron microscopy (despite their superior resolution) because the images are slope-encoded, not height encoded. Furthermore, samples viewed by AFM do not require electrical conductivity. This eliminates the requirement for metal or carbon coatings that would irreversibly change or damage a sample. While an electron microscope needs an expensive vacuum environment for proper operation, most AFM modes can work perfectly well in ambient air or even in a liquid environment. In principle, AFM can provide higher resolution than SEM. It has been shown to give true atomic resolution in ultra-high vacuum (UHV) and, more recently, in liquid environments. High resolution AFM is comparable in resolution to Scanning Tunneling Microscopy and Transmission Electron Microscopy.

Image size is one of the disadvantage of AFM when compared with the scanning electron microscope (SEM). A SEM can image an area to the order of millimetres $\times$ millimetres with a depth of field to the order of millimetres. But an AFM can only image a maximum height to the order of micrometres and a maximum scanning area of around 150 $\times$ 150 micrometres. Another disadvantage of AFM is the scanning speed. Traditionally, an AFM takes several minutes for a typical scan, which is much slower than the scanning speed of a SEM.

4.4.2. Imaging Micro and Nanostructure of Cement Paste

A DI 3100 AFM was used for imaging micro- and nanostructure of cement paste and for quantitative characterization of the effectiveness of polishing method described in Section 4.3. A paste

sample with a water to cement ratio of 0.5 was used for this study. Figure 4.7 shows the Digital Instrument Nanoscope MultiMode Scanning Probe Microscope used in this study. Figure 4.8 shows a blown up image of the tip holder. Topographic images were acquired in tapping mode using a silicon nitride tip of radius 10 nm. For each scan, the resolution was 217 $\times$ 217 pixels and the scan rate was 0.35 Hz. Varying scan sizes, from 2 μm $\times$ 2 μm to 60 μm $\times$ 60 μm were used. A Quanta scanning electron microscope and an optical microscope were used to get an overall idea of the sample surface, to examine the effectiveness of sample preparation and to provide structural and morphological information at different length scales. Figure 4.9 shows scanning electron microscopy image of cement paste sample polished using diamond suspension in the fine polishing step (protocol (a)) as described in Section 4.3. The image is captured in secondary

Figure 4.7. Digital Instrument Nanoscope MultiMode Scanning Probe Microscope

Figure 4.8. Digital Instrument Nanoscope MultiMode Scanning Probe Microscope Tip Holder

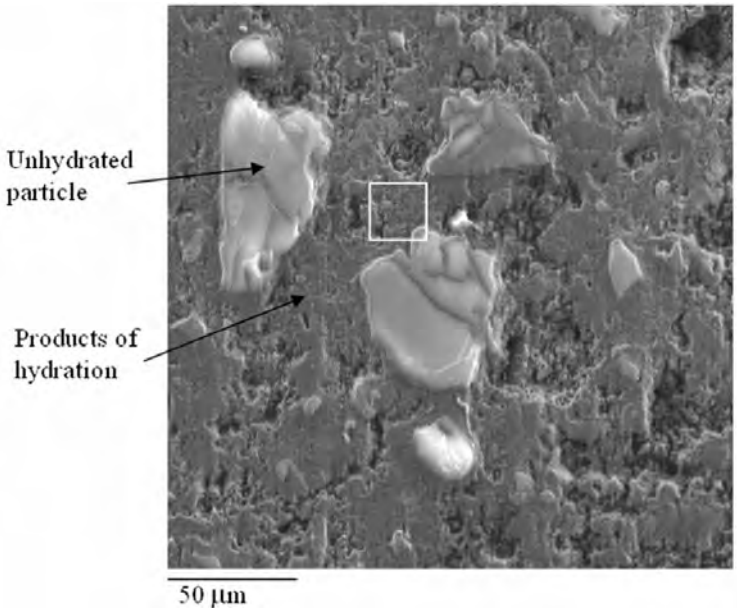

Figure 4.9. Scanning Electron Microscope Image of Polished Cement Paste

electron mode, where contrast is related to the height difference between different areas on the sample surface. From the image, it is clear that the unhydrated cement paste particles are at higher elevation than the rest of the paste matrix. Atomic force microscopy study was performed on an approximate area marked by a square on the SEM image. Figure 4.10 shows a 20 μm $\times$ 20 μm atomic force microscopy image of cement paste where the maximum height difference between different areas is 1.7 μm, brighter regions being at higher elevation than darker ones. Images of

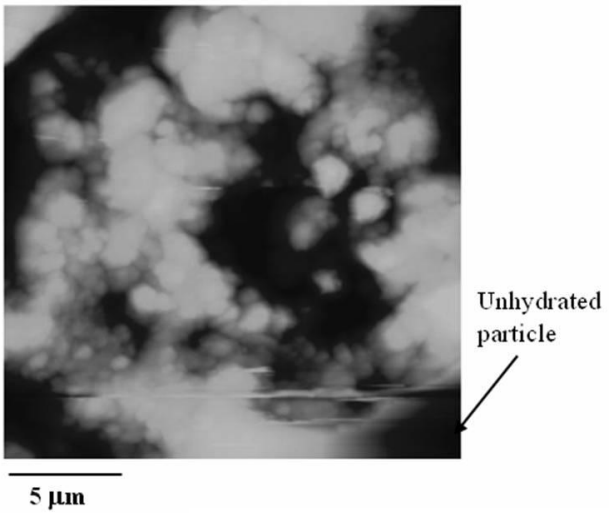

Figure 4.10. 20 μm $\times$ 20 μm Atomic Force Microscopy Image of Cement Paste

C-S-H gel captured at higher magnification showed nearly spherical particles of different sizes in different areas. Typical sizes of these spherical particles ranged from 100 nm to 700 nm. Figure 4.11 is an AFM image of C-S-H gel adjacent to an unhydrated cement particle. This image

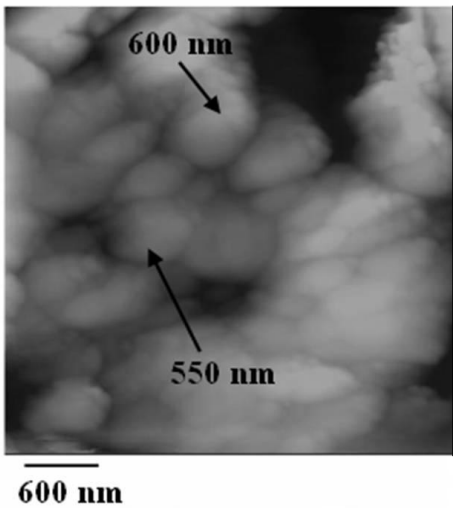

Figure 4.11. 3.9 μm $\times$ 3.9 μm AFM Image of C-S-H Near Unhydrated Cement Particle

shows comparatively large spherical particles in the size range of 550 nm to 600 nm. Figure 4.12 is another AFM image captured further away from unhydrated cement particle. The image in this area is showing C-S-H gel as cluster of 200 nm to 350 nm diameter spherical particles. Figure 4.13

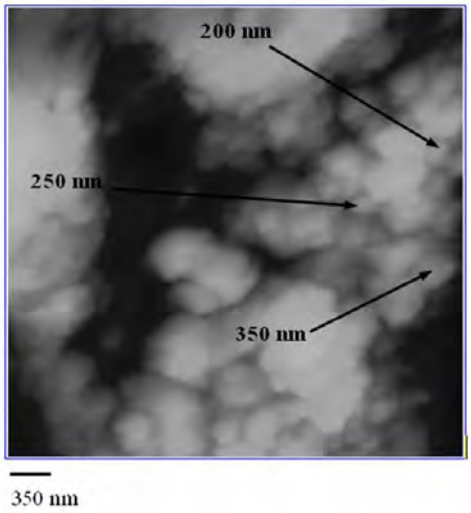

Figure 4.12. 4.7 μm ×4.7 μm AFM image of C-S-H further away from unhydrated cement particle

shows the scanning electron image of cement paste sample polished using diamond lapping film and diamond suspension in the fine polishing step (protocol (d)) described in Section 4.3. Very low contrast in this secondary electron SEM image represents the smoothness of the sample surface. Figure 4.14 shows the 50 μm $\times$ 50 μm atomic force microscopy image of cement paste where the maximum height difference between different areas is 1.5 μm. Again because of the effectiveness of the polishing method, it was possible to image such a big area with an unhydrated particle in it in one scan. Furthermore, in the AFM study, the inherent structure of a material is revealed in the topography image as the course sample roughness is eliminated. As an example, Figure 4.15 shows a 1.5 μm $\times$ 1.5 μm AFM topography image. With the improved polishing technique, C-S-H

gel in this high magnification image was observed as clusters of 40 nm diameter spherical particles. So, with the effectiveness of the fine polishing step (d), it was possible to explore the structure of C-S-H gel at a scale of 40-50 nm. Spherical particles of larger sizes have been seen in other areas even after using the new polishing techniques [53, 54].

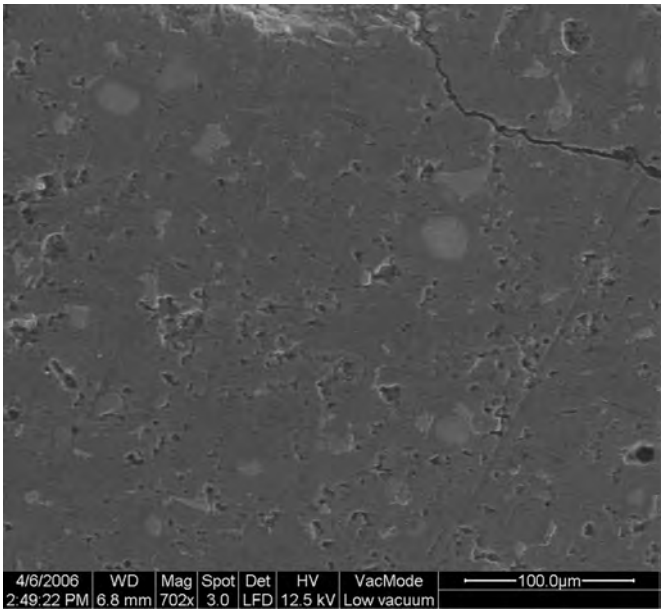

Figure 4.13. Scanning Electron Microscope Image of Cement Paste with improved polishing

4.4.3. Quantitative Evaluation of Sample Roughness Using Atomic Force Microscopy

Each image file, obtained from AFM, was digitally analyzed to determine surface roughness quantitatively. First, a linear slope correction was performed to account for an alignment difference between the reference plane of AFM imaging and the overall slope of the sample surface. Root-mean-squared average (RMS) of the topography of the surface was chosen to measure surface

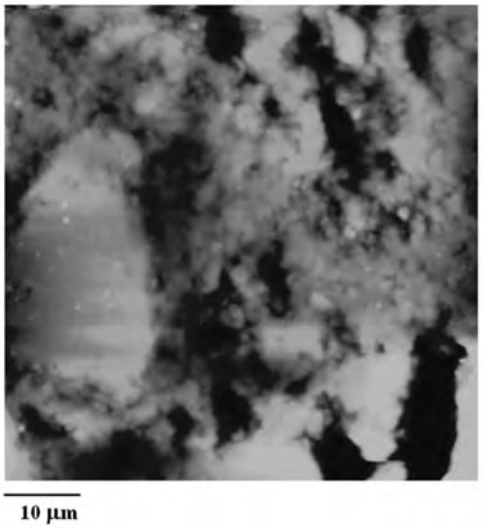

Figure 4.14. 50 μm $\times$ 50 μm Atomic Force Microscopy Image of Relatively Smooth Polished Cement Paste

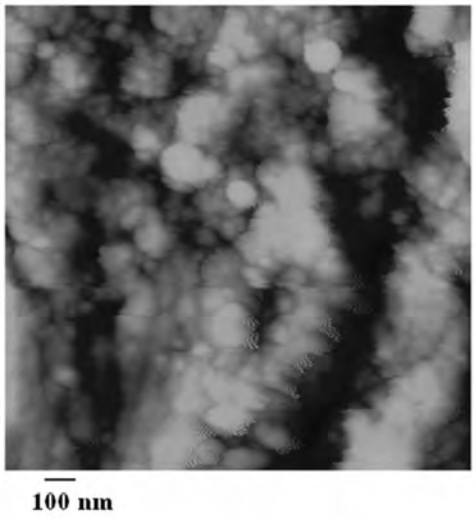

Figure 4.15. 1.5 μm $\times$ 1.5 μm Atomic Force Microscopy Image of Relatively Smooth Polished Cement Paste

roughness. RMS roughness, S_q is defined as:

$$S_q = \sqrt{\frac{1}{MN}\sum_{i=0}^{M-1}\sum_{j=0}^{N-1}\left[z\left(x_i, y_j\right) - \mu\right]^2} \tag{4.1}$$

where N is the number of pixels in each scan edge and z_{ij} is the height at position (i, j) from the mean plane. μ is the average surface height and is defined as

$$\mu = \frac{1}{MN} \sum_{i=0}^{M-1} \sum_{j=0}^{N-1} z\left(x_i, y_j\right) \tag{4.2}$$

Figure 4.16 shows a 50 μm $\times$ 50 μm AFM image of a 10-day-old polished cement paste with w/c 0.5. Surface topography shows an unhydrated cement particle on the left side of the image. From the 3D image at the bottom, it can be concluded that the cement particle is polished better than the rest of the paste. Three cross-section images on the right shows height variation at each one third of the image. Figure 4.17 shows a 50 μm $\times$ 50 μm AFM image of another area without unhydrated cement particle. Both the 3D surface topography and the cross-section image show that the surface is flat except the peaks and the valleys introduced by the capillary porosity. Table 4.1 shows the RMS roughness calculated from AFM images of different sizes. Data shows an increasing trend of RMS roughness with increase in image size. This can be justified by comparing AFM images of different sizes. Figure 4.18 shows 20 μm $\times$ 20 μm AFM image. Comparing Figure 4.18 with Figure 4.16 and Figure 4.17, it is clear that an image of smaller size shows less surface height variation. This conclusion can be further verified by looking at Figure 4.19, which is a 1.5 μm $\times$ 1.5 μm 3D topography image. As expected, this image shows very little height variation. Furthermore, it should be noted that Figure 4.19 shows an area twice the size of an area that is expected to be in contact during one indentation. Surface roughness in such a small area is very low. However, in a recent paper, Ulm et al. [48] reports that the RMS roughness, measured over an area with one side 200 times the average depth of indentation, should be less than one fifth

Image size	50 μm $\times$ 50 μm	40 μm $\times$ 40 μm	20 μm $\times$ 20 μm	10 μm $\times$ 10 μm
Avg. RMS Roughness (nm)	200	150	50	40

Table 4.1. Change in RMS Roughness with Image Size

of the average indentation depth. This implies that for the average indentation depth used in this study (200 nm), RMS roughness calculated over an area of 40 μm $\times$ 40 μm should be less than 40 nm. Table 4.1 reports RMS roughness of 150 nm obtained in this study for an area of 40 μm $\times$ 40 μm. However, another recent paper by Trtik, Holzer and et al. [79] reports that there is an intrinsic RMS roughness of cement paste. According to Holzer et al., the average intrinsic RMS roughness of cement paste is between 115 nm to 492 nm and a RMS roughness below this may indicate surface damage and polishing artefact.

4.5. Conclusion

One of the main challenges in applying nanoindentation to characterize cementitious material is preparing the sample surface. Contact mechanics theory used in the analysis of nanoindentation data is based on indentation on a flat surface. Therefore, the accuracy of nanoindentation experiments on cementitious materials depend on reducing the surface roughness to a tolerable level without causing any damage to the sample. In this study, a surface preparation technique was developed. Atomic force microscopy was used to image and characterize cement paste micro- and nanostructure. The structure of C-S-H gel in different areas showed spherical particles of different sizes in the range of 200-700 nm. With the development of an improved polishing protocol, it was found that in many areas of C-S-H, there are spherical particles as small as 40 nm. Even after

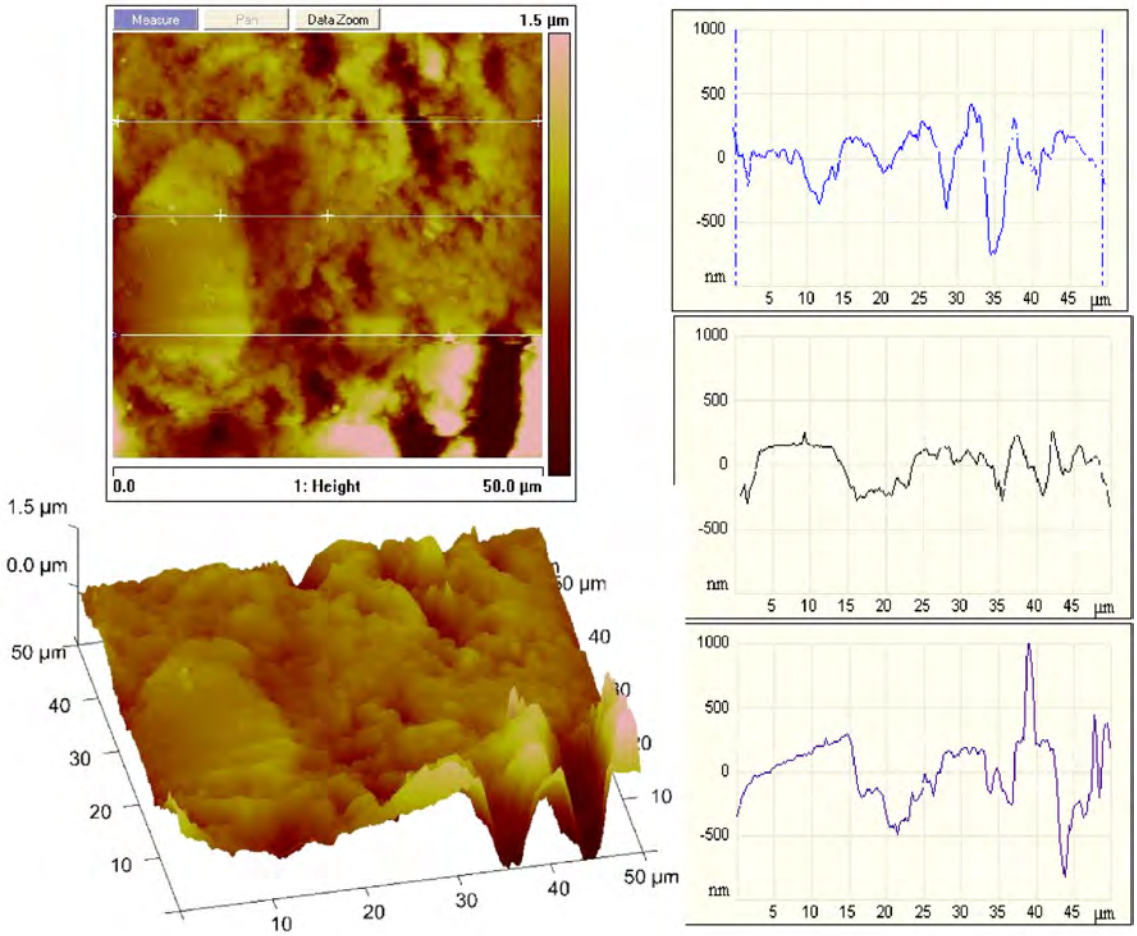

Figure 4.16. 50 μm $\times$ 50 μm AFM Image with Unhydrated Cement Particle: Topograpgy, Cross-section, 3D Topography

improved polishing, the size of spherical particles were found to vary in different areas, which seemed to be an inherent nature of C-S-H.

Quantitative analysis of surface roughness was performed by calculating RMS surface roughness from AFM topography images. Data showed an increasing trend of RMS roughness with an

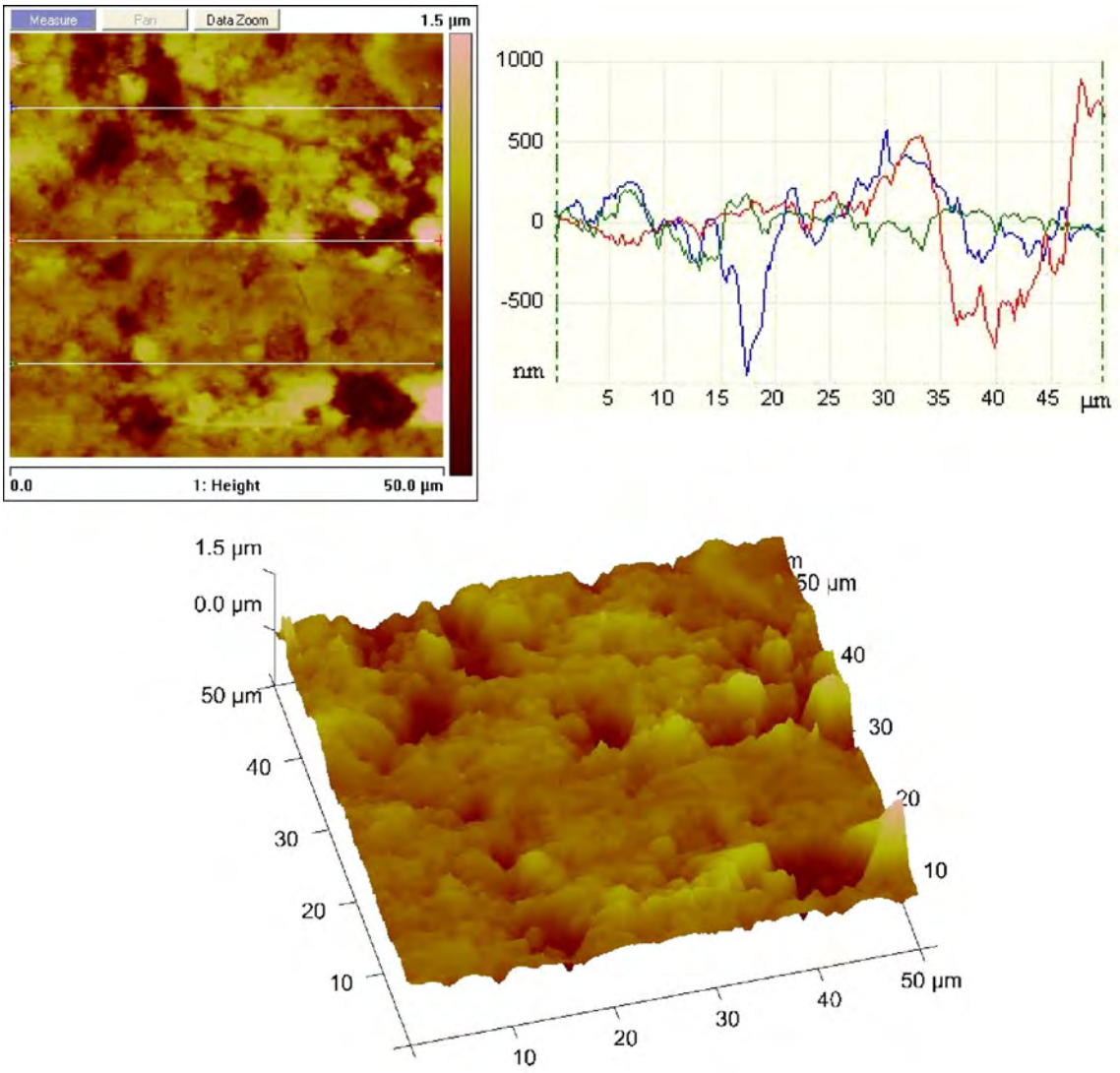

Figure 4.17. 50 μm $\times$ 50 μm AFM Image: Topograpgy, Cross-section, 3D Topography

increase in image size. It is clear that an image of smaller size showed less surface height variation. A 1.5 μm $\times$ 1.5 μm 3D topography image which is almost twice the size of an area expected to be in contact during one indentation, showed very little surface roughness. However, RMS roughness reported in this study does not satisfy the roughness criteria reported in a recent paper by Ulm et

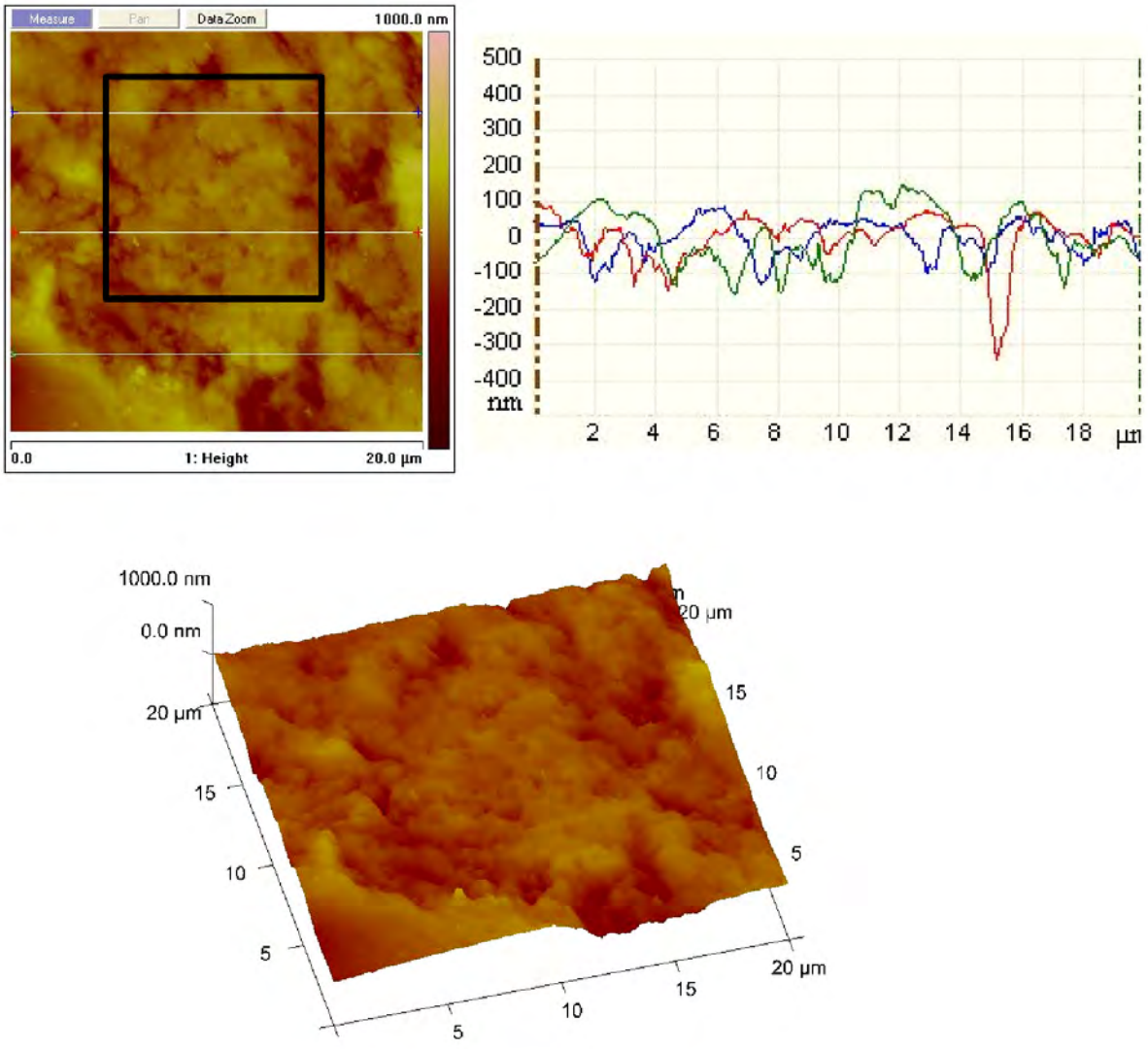

Figure 4.18. 20 μm $\times$ 20 μm AFM Image: Topograpgy, Cross-section, 3D Topography

al. [48]. RMS roughness obtained in this study for an area of 40 μm $\times$ 40 μm is 150 nm, which is higher than the roughness reported by Ulm et al. However, another recent paper by Trtik, Holzer

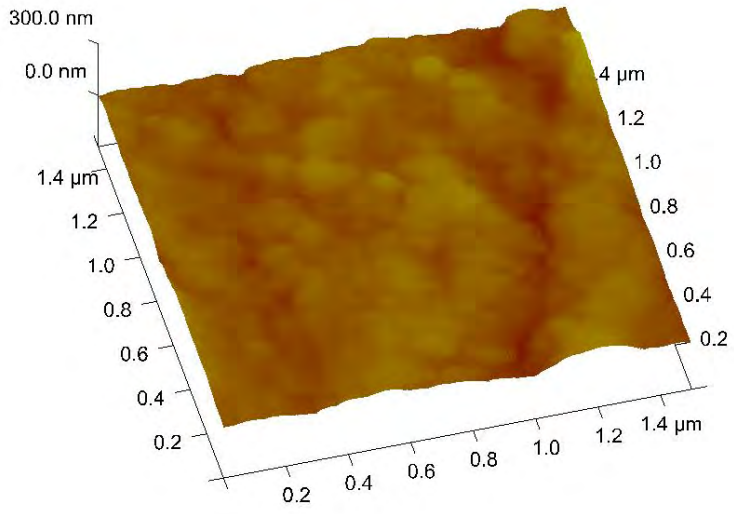

Figure 4.19. 1.5 μm $\times$ 1.5 μm 3D Topography Image of Polished Cement Paste

and et al. [79] reports that there is an intrinsic RMS roughness of cement paste. According to Holzer et al., average intrinsic RMS roughness of cement paste is between 115 nm to 492 nm and a RMS roughness below this may indicate surface damage and polishing artefact.

Chapter 5 Cement Paste Microstructure: Determination of Local Mechanical Properties

5.1. Introduction

Nanoindentation experiments were performed to determine local mechanical properties of different phases of cement paste microstructure. The initial phase of this research involved the use of a local probe of an atomic force microscope (AFM) to determine nanoscale mechanical properties. The advantage of this method is the high resolution imaging that can be performed using the same probe. This enables simultaneous study of the morphology of different phases and their mechanical properties. However, for detailed study in the second phase, a special type of nanoindenter from Hysitron, called Triboindenter, was used. Nanoindentation has been used successfully by researchers in the recent past to determine local mechanical properties of cementitious materials [21, 23, 25, 35, 51–54, 56, 80]. In most conventional nanoindenters, one disadvantage is the

absence of imaging capability. As a result, imaging has to be done using a different instrument, such as a SEM or an AFM. This is really time consuming and in most of the cases it is very difficult to image the same area before and after indentation. The advantage of using a Triboindenter is that it combines principles of nanoindentation with atomic force microscopy.

5.2. Experimental Detail

5.2.1. Material Used and Sample Preparation

Cement paste samples were made using Type I Portland cement from Lafarge. The chemical composition of the cement is listed in Table 5.1. The Blaine surface area was 365 m^2/kg. The

Chemical Data	SiO_2	CaO	Al_2O_3	Fe_2O_3	C_3S	C_3A
Percent	20.4	65.3	4.8	2.8	68	8

Table 5.1. Chemical Composition of Type I Cement

specification of ASTM standard C305 was followed during the mixing of cement paste. Samples were cured under water for a desired period of time at 25° C temperature. After curing, samples were either polished following the procedure discussed in Chapter 4 or submerged in acetone to prevent further hydration during storage. Three sets of samples were made with water to cement ratio of 0.35, 0.5 and 0.65. The age of these samples were kept constant (10 days) to compare changes in microstructural properties with water-cement ratio. Next, the water to cement ratio was kept fixed at 0.5 and changes in nano-mechanical properties of cement paste with curing age were studied. For this purpose, two additional sets of samples with water-cement ratio of 0.5 were prepared and cured for one month and six months respectively.

5.2.2. Nanoindentation Using Atomic Force Microscopy

Indentation and subsequent determination of nanoscale mechanical properties of a material can be performed using an atomic force microscope (AFM) in force mode [10, 11, 54]. In this study, a Digital Instruments D3000 scanning probe microscope with a special diamond-tipped indentation probe was used (shown schematically in Figure 5.1). The diamond tip had an approximate tip radius of 25 nm and was attached to a stainless steel cantilever that had approximate width of 100 μm, thicknesses of approximately 13 μm, and lengths of approximately 350 μm. The effective spring constant was estimated to be 150 N/m (as supplied by Digital Instruments). During the experiment in AFM force mode, the probe tip was first lowered into contact with the sample, then an indentation was made into the surface, and finally the tip was lifted off the sample surface. The probe tip deflection was measured concurrently and a plot of tip deflection versus piezo motion, called a force curve, was generated. A typical force plot is shown in Figure 5.2 where force

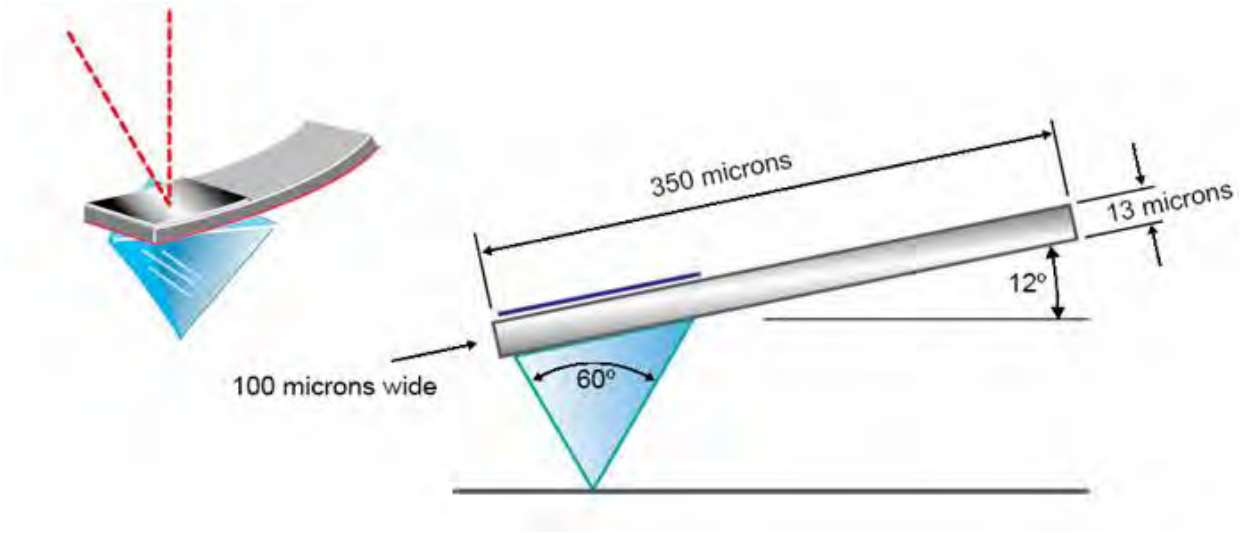

Figure 5.1. Schematic Diagram of Diamond Indenter Probe for Atomic Force Microscopy

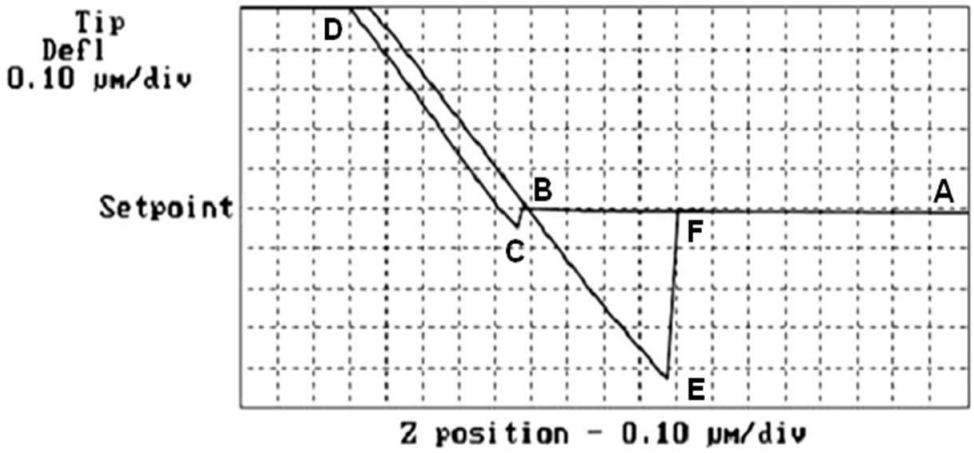

Figure 5.2. Typical Force Plot Recorded in Force Mode of Atomic Force Microscopy

can be calculated as the difference in piezo movement in the z-direction times the spring constant. As the piezo moves toward the sample surface (or vice-versa, depending on the system), the tip deflection remains constant until the probe tip touches the sample surface (A to B in Figure 5.2). Now, just before contact, the tip can be pulled down to the surface by attractive forces, causing a small decrease in tip deflection (B to C in Figure 5.2). Further decrease in the piezo height causes indentation onto the sample surface and at the same time, the cantilever deflects in the opposite direction, increasing the tip deflection from C to D as shown in the figure. During unloading, the cantilever deflection reduces (D to E in Figure 5.2) while the piezo retracts. Due to the tip-sample adhesion, the cantilever deflects further down (E to F) and finally jumps out of contact. For an infinitely stiff sample with respect to the probe, no indentation on the sample surface will occur and the piezo movement will cause only bending of the cantilever. This phenomenon can be used to calibrate the AFM probe under the operating conditions, i.e. a comparison of the force curve

without any indentation and with significant indentation in the sample of interest can be used to extract mechanical properties of the sample. In this study, sapphire was considered to be infinitely stiff and force curve captured on it was used for calibration.

5.2.3. Nanoindentation Using Hysitron Triboindenter

Figure 5.3. Hysitron Triboindenter

As mentioned earlier, a Hysitron Triboindenter (Figure 5.3) was used in the second phase of this research. Figure 5.4 shows a schematic diagram of a nanoindenter. Figure 5.5 shows a close up of the transducer and piezo assembly which is the specialty of this instrument. It combines nanoindentation to determine the local mechanical properties with high resolution in-situ scanning probe microscopy (SPM) imaging that allows pre and post-test observation of the sample. The ability to indent and image using the same probe in one instrument eliminates the complication of locating the same area with different instruments or coupling two different instruments, such as a SEM and a nanoindenter to work together. A Triboindenter allows for a more direct approach where

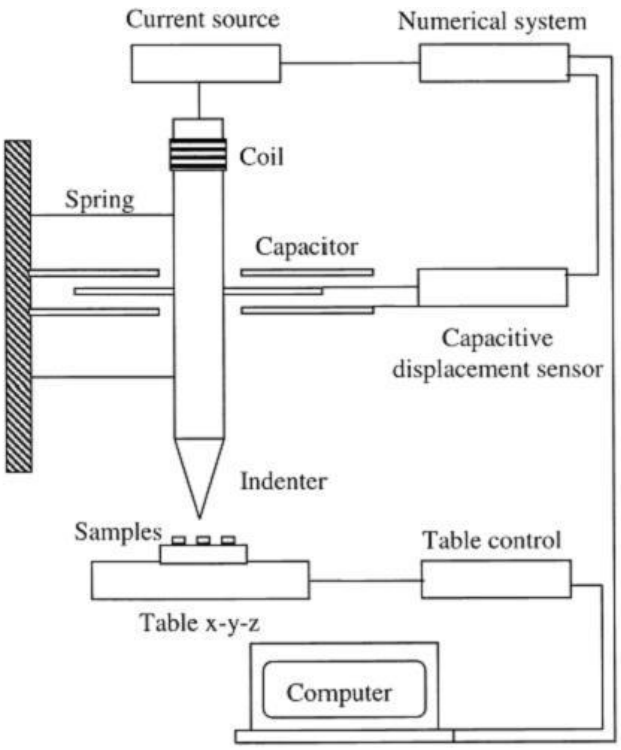

Figure 5.4. Schematic Diagram of A Nanoindenter

one can identify different phases in cement paste through imaging and determine local mechanical properties of the same phases with minimal ambiguity. A Berkovich tip with total included angle of 142.3 degrees was used for indentation. The trapezoidal load function shown in Figure 5.6 represents how load was applied during a typical single load cycle indentation. Maximum load was reached in 5 seconds and the load was then held constant for 2 seconds. Finally the load was completely released in 5 seconds. The Load vs. displacement of the tip inside the sample was recorded during the whole indentation process (12 seconds). Figure 5.7 (a) shows a typical load displacement plot recorded from nanoindentation on C-S-H in a hardened cement paste sample. Some of the indentation test data were discarded due to irregular nature of the load-displacement

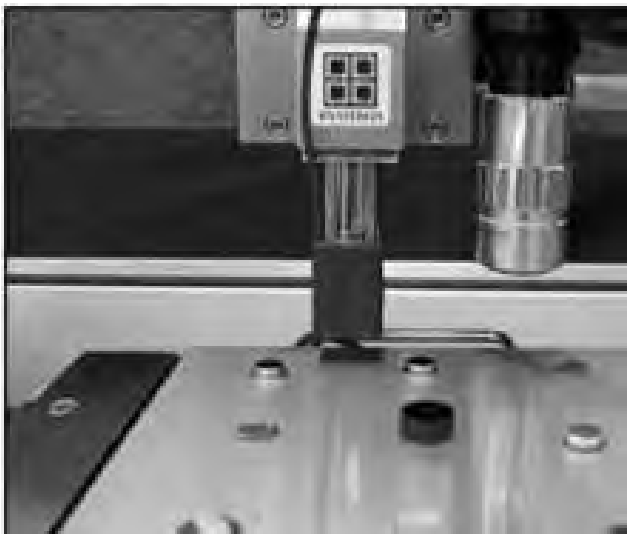

Figure 5.5. Close up: Transducer and Piezo Combination for SPM Imaging and Nanoindentation

plot (Figure 5.7 (b)) which could be due to the presence of large voids at the indentation site or cracking of the material during indentation. Multiple cycles of partial loading and unloading

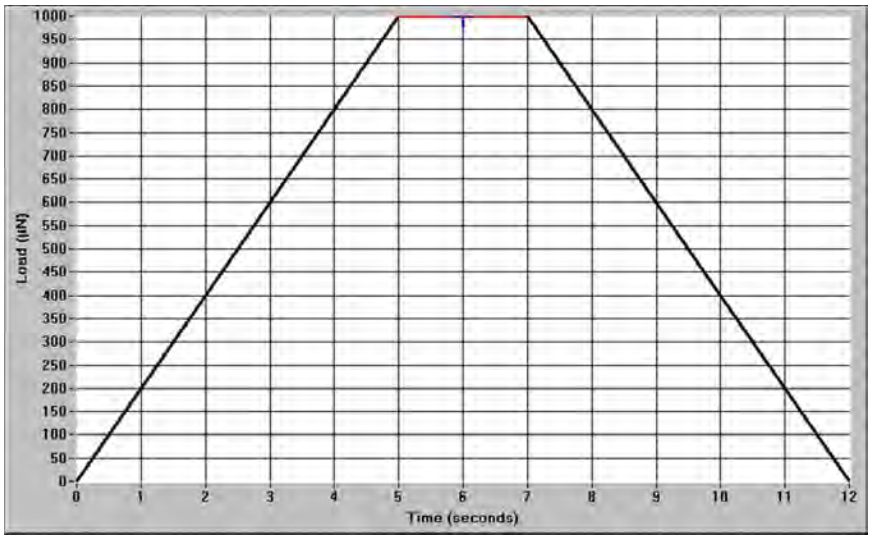

Figure 5.6. A Typical Single Cycle Trapezoidal Loading Plot, Loading Time: 5 Seconds, Hold Time: 2 Seconds, Unloading Time: 5 Seconds

were used to make each indent, thereby eliminating creep and size effects [56]. Figure 5.8 shows a

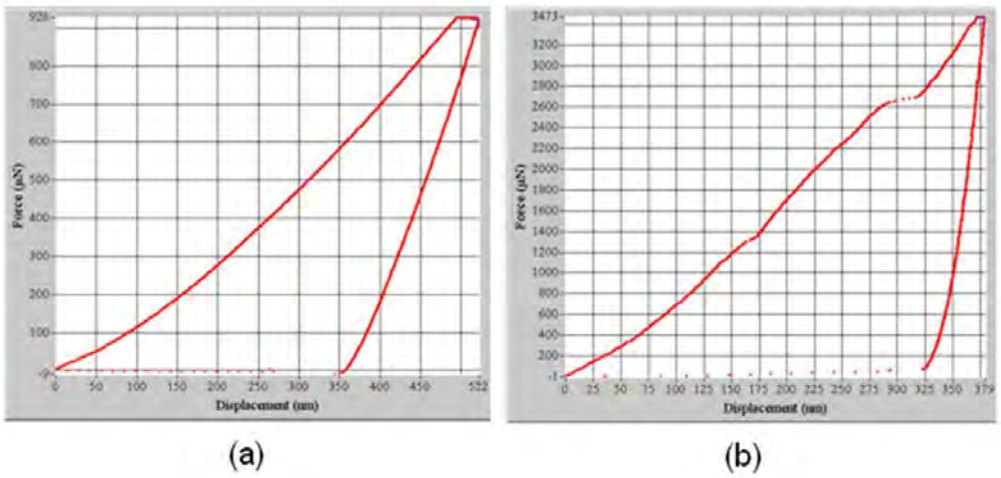

Figure 5.7. Sample Force-Indentation Plot, (a) Acceptable, (b) Not Acceptable

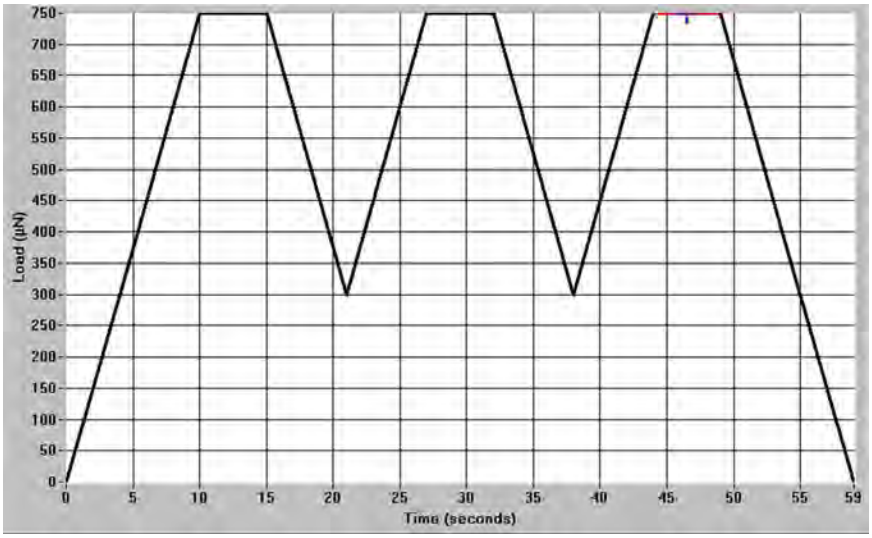

Figure 5.8. Three Cycle Loading Plot, Time to Reach Maximum Load: 10 Seconds, Hold Time: 5 Seconds, Time to Complete Unload: 10 Seconds

typical three-cycle loading plot. The time to reach maximum load in the first cycle was 10 seconds and the loading rate was kept constant for each cycle. Time for complete unload in the last cycle was also 10 seconds to maintain the same loading and unloading rate. In each cycle, the maximum

load was held constant for a period of 5 seconds. In different tests, maximum load of 500 N, 750 N and 1000 N were used at a loading rate of 100 N/s to 300 N/s. Corresponding variation in depth of indentation was from 150 nm to 350 nm. Figure 5.9 shows a force-indentation plot for three loading and unloading cycles. Elastic properties were evaluated from the final unloading region of the load vs. indentation curve using the Oliver and Pharr method [59] as described in Chapter 3. 100 indents were made on a fused silica sample to determine the area function. Knowing the indentation modulus of the fused silica as 69.6 GPa, the method described in Section 3.4.1 was used to established a relationship between contact depth and contact area. Figure 5.10 shows the area function determined from a standard quartz sample.

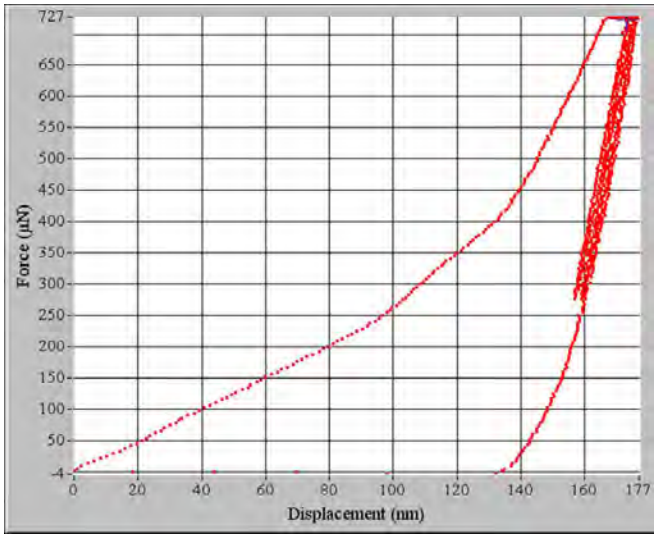

Figure 5.9. Sample Force-Indentation Plot for Multiple Loading Unloading

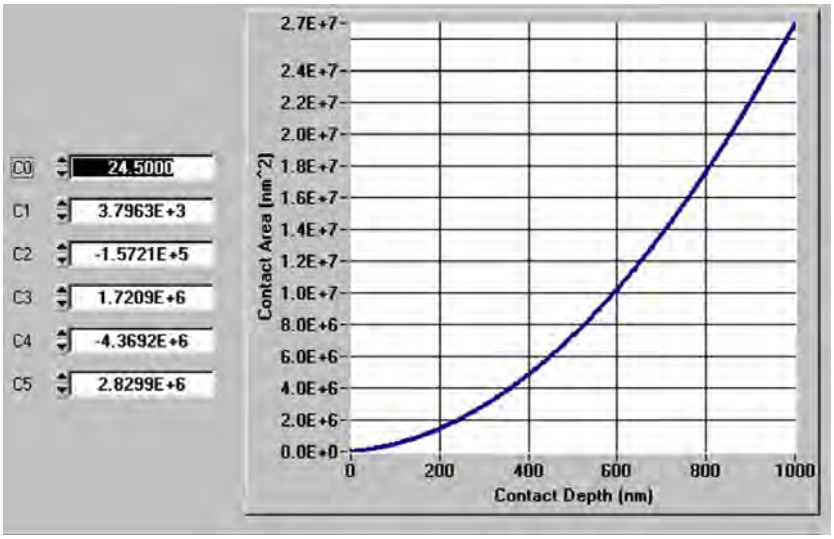

Figure 5.10. Area Function: Contact Area vs. Contact Depth Plot Determined on Fused Silica Sample

5.2.4. Nanoindentation with In-situ Imaging

The imaging feature of the Triboindenter provides the capability to identify different phases and to position the indenter probe within ten nanometers (according to the instrument specification) of the desired test location. Post-test imaging also provides the ability to verify that the test was performed at the desired location, which maximizes reliability of the data. As shown in Figure 5.11, an image of a representative area of a cement paste sample was captured first with the Berkovich tip. Then nearly 36 locations were selected for indentation, both on the unhydrated particle and on the area around it. Using the same tip, an image was captured after indentation to make sure that the indents were made at the desired locations.

5.2.5. Grid Indentation

Figure 5.12 shows schematically the grid indentation method. Intersection points in the grid represents indent locations. In this technique, a representative area on a sample surface is selected

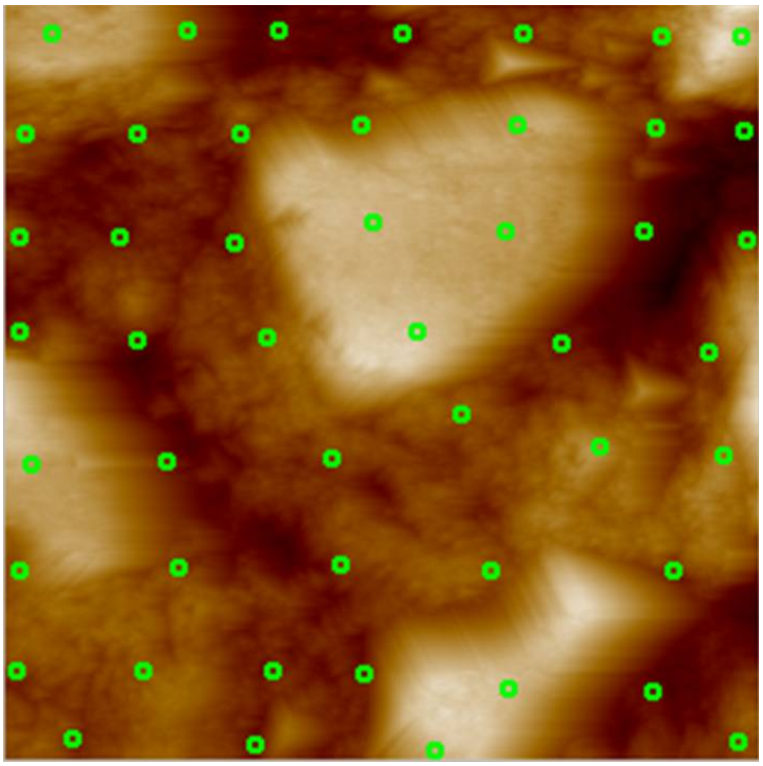

Figure 5.11. 60 μm ×60 μm Image of Paste Showing Locations of Indents

based on scanning electron microscopy and possibly atomic force microscopy imaging. A large number of indentations are performed on the sample and the data collected is analyzed statistically. In a multi-phase sample such as cement paste, statistical analysis of huge data obtained from experiments provide information on the mechanical properties and volume fraction of different phases present [23].

The distribution of the mechanical properties of each phase is assumed to follow a normal distribution. Thus, if the random variable X denotes one such mechanical property (e.g. elastic

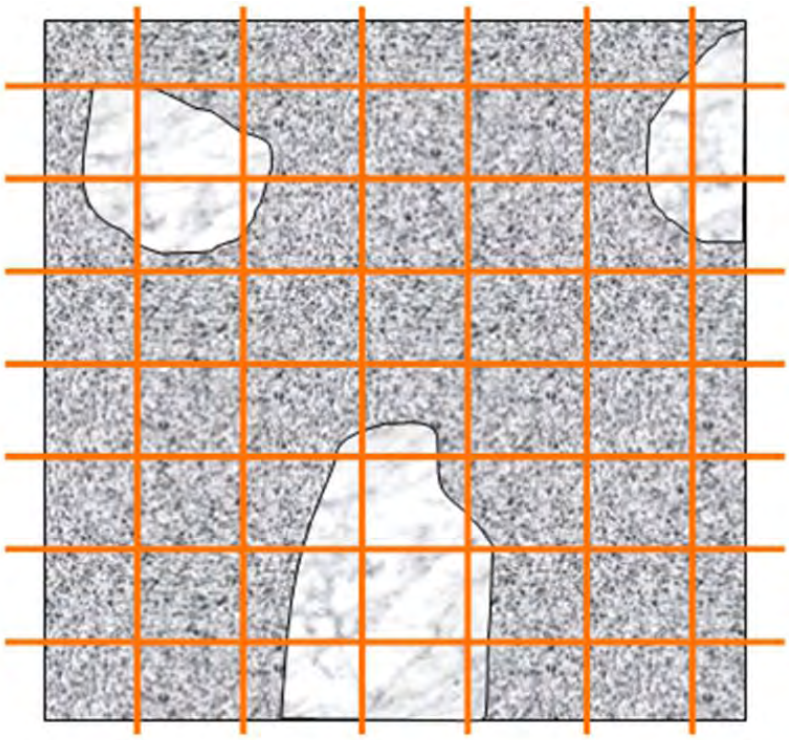

Figure 5.12. Schematic Diagram of Grid Indentation on Cement Paste Sample

modulus or hardness), then the probability distribution of X in phase i is given by

$$\phi_i(x) = \frac{1}{\sqrt{2\pi}\sigma_i} \exp\left(-\frac{1}{2\sigma^2}(x-\mu_i)^2\right) \tag{5.1}$$

where the parameters μ_i and σ_i^2 are respectively the mean and variance of the distribution.

Let $X_1, X_2, \ldots, X_N$ denote the independent and identically distributed (iid) sample data of one mechanical property obtained from grid indentation. If the specimen has only one phase then using the theory of statistical estimation, the maximum likelihood estimates (MLE) of $\mu \equiv \mu_1$ and

$\sigma^2 \equiv \sigma_1^2$ can be written as

$$\hat{\mu} = \bar{x} = \frac{1}{N}\sum_{k=1}^{N} x_k \tag{5.2}$$

$$\hat{\sigma}^2 = S^2 = \frac{1}{N-1}\sum_{k=1}^{N}(x_k - \bar{x})^2 \tag{5.3}$$

Now, for n phases present in the specimen with volume fractions $f_1, f_2, \ldots, f_n$, the theoretical (population) probability distribution of the mechanical property for the whole specimen is given by

$$\phi(x) = \sum_{i=1}^{n} f_i \phi_i(x) \tag{5.4}$$

$$\text{s.t.} \sum_{i=1} f_i = 1 \tag{5.5}$$

The sample data $X_1, X_2, \ldots, X_N$ is grouped into m bins to construct the empirical probability distribution function (p.d.f.). $g(x_j)$, $j = 1, 2, \ldots, m$ denote the empirical p.d.f, where x_j denote the mid point of the j^{th} bin. Then, for estimating the parameters of the population distribution the

following nonlinear optimization problem $(P1)$ may be used

$$
\begin{aligned}
(P1) \qquad \min_{\substack{\mu_1,\ldots,\mu_n,\\ \sigma_1,\ldots,\sigma_n\\ f_1,\ldots,f_n}} \quad & \sum_{j=1}^{m} \frac{\left(\sum_{i=1}^{n} f_i\phi_i(x_j) - g(x_j)\right)^2}{m} \\
s.t. \quad & \sum_{i=1}^{n} f_i = 1 && (5.6)\\
& -\infty < \mu_i < \infty, \qquad \forall i = 1,2,\ldots,n && (5.7)\\
& 0 < \sigma_i < \infty, \qquad \forall i = 1,2,\ldots,n && (5.8)\\
& 0 \le f_i \le 1, \qquad \forall i = 1,2,\ldots,n && (5.9)
\end{aligned}
$$

Thus, there are total $3n$ unknowns (μ_i, σ_i and f_i for each phase $i = 1, 2, \ldots, n$) in problem $(P1)$. But due to the equality constraint given in Eq. 5.6, total number of unknown reduces to $3n - 1$. Hence, the number of bins m should be so chosen that $3n - 1 \le m \le N$.

However, the dependence of the optimization problem on bin size may be eliminated if the error minimization is performed using cumulative distribution function (c.d.f) [82]. This problem is described below. Let, $\Phi_i(x)$ denote the c.d.f of the mechanical property in phase i. Then from Eq. 5.1

$$\Phi_i(x) = \int_{-\infty}^{x} \phi_i(y)dy = \int_{-\infty}^{x} \frac{1}{\sqrt{2\pi}\sigma_i} \exp\left(-\frac{1}{2\sigma^2}(y-\mu_i)^2\right) dy \tag{5.10}$$

Next let $X_{(1)}, X_{(2)}, \ldots, X_{(N)}$ denote the sorted sample data obtained from grid indentation. Then the expression for the empirical c.d.f is given by

$$G(x_{(i)}) = \frac{i}{N} - \frac{1}{2N}, \qquad \forall i = 1, 2, \ldots, N \tag{5.11}$$

Now the nonlinear optimization problem $(P2)$ described below, may be used to estimate the population parameters.

$$(P2) \quad \min_{\substack{\mu_1,\ldots,\mu_n,\\ \sigma_1,\ldots,\sigma_n\\ f_1,\ldots,f_n}} \quad \sum_{j=1}^{N} \left(\sum_{i=1}^{n} f_i \Phi_i(x_j) - G(x_j) \right)^2$$

$$s.t. \quad \sum_{i=1}^{n} f_i = 1 \tag{5.12}$$

$$-\infty < \mu_i < \infty, \qquad \forall i = 1, 2, \ldots, n \tag{5.13}$$

$$0 < \sigma_i < \infty, \qquad \forall i = 1, 2, \ldots, n \tag{5.14}$$

$$0 \leq f_i \leq 1, \qquad \forall i = 1, 2, \ldots, n \tag{5.15}$$

5.2.6. Comparison between Indentation with Imaging and Grid Indentation

Grid indentation is the preferred method to perform large number of indents on a sample. It requires much less operator time compared to indentation with imaging. For example, if 100 indents are programmed at a time, the indentation instrument can make all the indents and collect data in a 6-hour period without further assistance from an operator. Statistical analysis of this huge set of data obtained from grid indentation provides information about the overall nanomechanical

signature of any sample and volume fractions of significant phases involved. On the other hand, indentation with imaging is preferred if one is concerned with determining local nanomechanical properties at a specific site on the sample. Grid indentation is most likely to miss these areas of specific interest or the number of data obtained will not be statistically significant.

5.3. Nanoindentation Data Analysis

5.3.1. AFM Nanoindentation Data Analysis

Figure 5.13 shows a force plot recorded from three different indentations on a polished cement paste sample. The difference in the elastic properties at these three indent locations can be inferred from the difference in the slope of the unloading part (see Eq. 3.39). Figure 5.14 shows an AFM image captured after making several indents with the same peak load on the cement paste sample. Again, from the size of indent visible in the image, the difference in mechanical properties of different areas can be inferred. From the test data, a relative Young's modulus was determined. However, the disadvantage of this method is the difficulty to get absolute modulus values. Furthermore, in the case of samples with a relatively high stiffness such as cementitious samples, most of the piezo movement manifests itself in the form of cantilever bending rather than indentation in the sample. The Testing procedure was found to be not sensitive enough for a stiff material like hardened cement paste to determine quantitative values. This method has, however been applied to soft materials like yeast and polymers successfully.

5.3.2. Nanoindentation with In-situ Imaging: Data Analysis

To determine local mechanical properties quantitatively, a Hysitron Triboindenter was used. Imaging capability of the instrument was effective in easy identification of the unhydrated cement

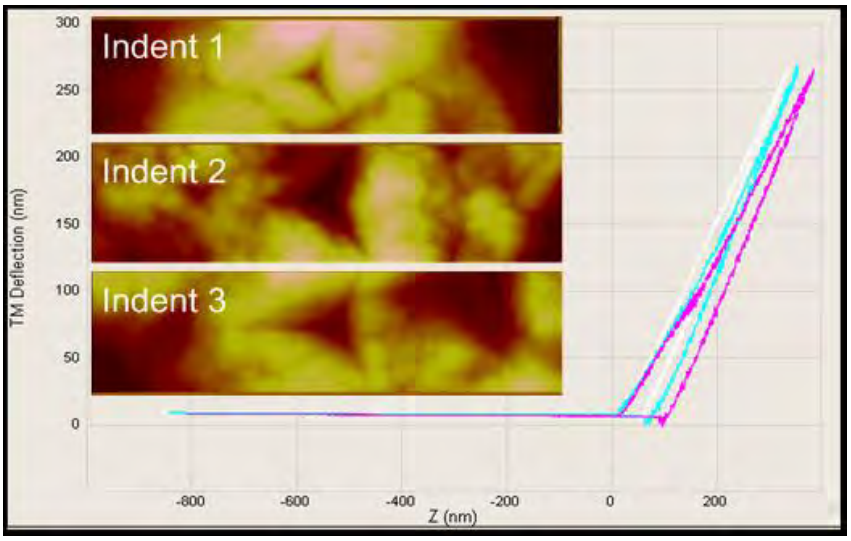

Figure 5.13. Force Plot Recorded from Three Different Indents on Hardened Cement Paste using Atomic Force Microscopy

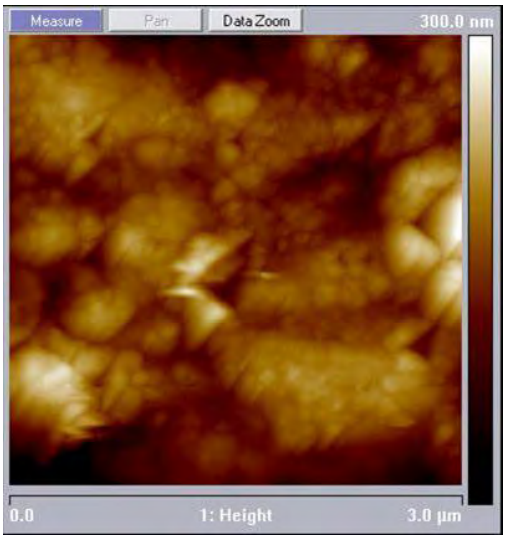

Figure 5.14. Atomic Force Microscopy Image Recorded after Indentation

particles from the products of hydration. Figure 5.15 shows an image of unhydrated cement particle captured with the indenter tip right after making an indent at the center of the image. The elastic modulus of unhydrated particles were found to be around 100 GPa. This is little lower than the

results reported by Velez *et al.* [85]. The difference can be explained since Velez *et al.* used pure clinker phases with very little porosity where as unhydrated cement particles seems more porous. Imaging capability of the instrument was also helpful to position the tip on products of hydration close to unhydrated cement particles. This facilitated exploring the variation in local mechanical properties in different areas of the paste matrix. Figure 5.16 shows an example where the indent was made close to an unhydrated particle. A decrease in elastic modulus was observed with an

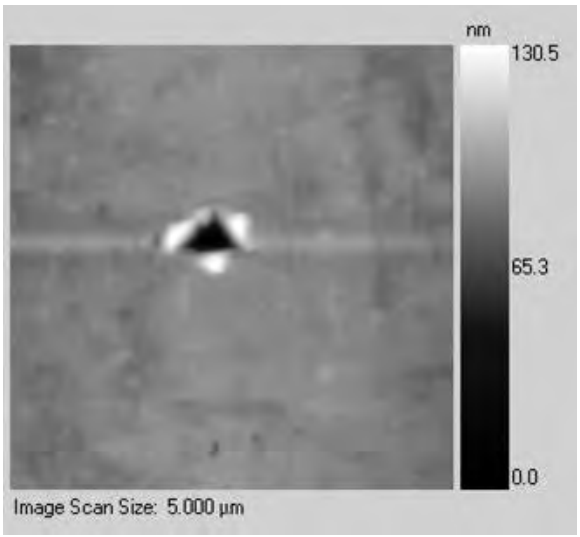

Figure 5.15. Image of Residual Indent on Unhydrated Cement Particle Captured with Indenter Tip of the Triboindenter

increase in distance from an unhydrated cement particle. Figure 5.17 shows one such instance where elastic modulus is plotted with the distance from the particle. Elastic modulus values were determined with an assumed Poisson's ratio of 0.15 for all the phases. Results of this initial study matched well with the existing literature that reported presence of a high density, stiffer layer of C-S-H around unhydrated cement particles in hydrated cement paste. A more rigorous study was carried out to confirm the results. Figure 5.18 is a 60 μm $\times$ 60 μm image of a 10-day-old

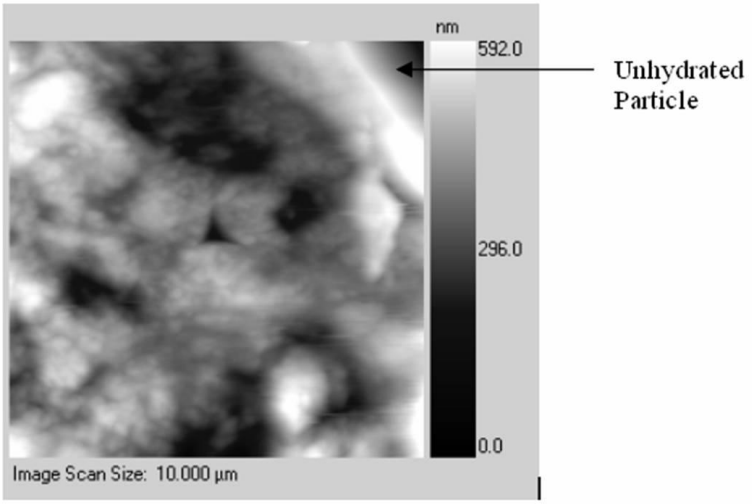

Figure 5.16. 10 μm ×10 μm Image of Paste Showing Residual Indent near Unhydrated Cement Particle

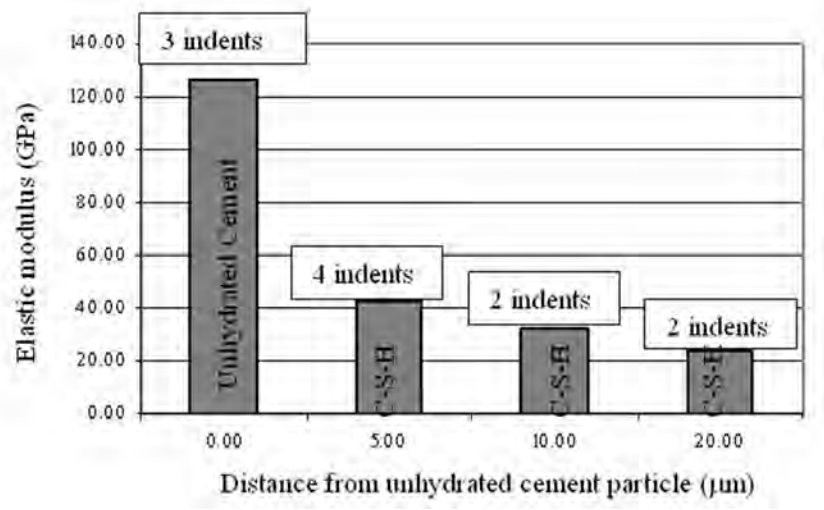

Figure 5.17. Change in Modulus of C-S-H with the Distance from Unhydrated Cement Particle

polished cement paste sample with w/c = 0.5. This figure clearly shows an unhydrated cement particle near the bottom of the image and adjacent paste matrix. The area was first chosen as a representative of cement paste sample and the image was captured with the berkovich tip.

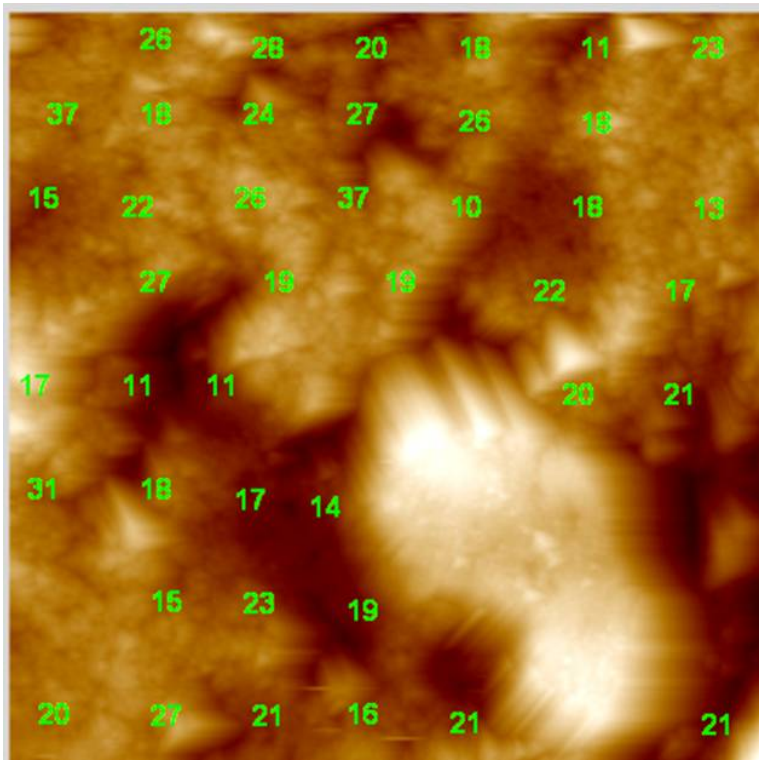

Figure 5.18. 60 μm $\times$ 60 μm Image of Cement Paste with 0.5 w/c Showing Indentation Modulus in GPa Written on Each Indent Locations

Then nearly 50 locations were selected for indentation both on the unhydrated particle and on the area around it following the method described in Section 5.2.4. Some of the indentation test data has been discarded because of the nature of the load-displacement plot which could be due to the presence of large void in the area or cracking of the material during indentation. Finally, the indentation modulus was calculated from each indent which is related to the elastic modulus and Poisson's ratio (see Eq. 3.19) of the particular phase. In this study, since Poisson's ratio of different phases present in cement paste microstructure was not measured, it was decided to represent indentation results in terms of indentation modulus instead of elastic modulus. This is in agreement with recent literature. Furthermore, using assumed value of same Poisson's ratio (which

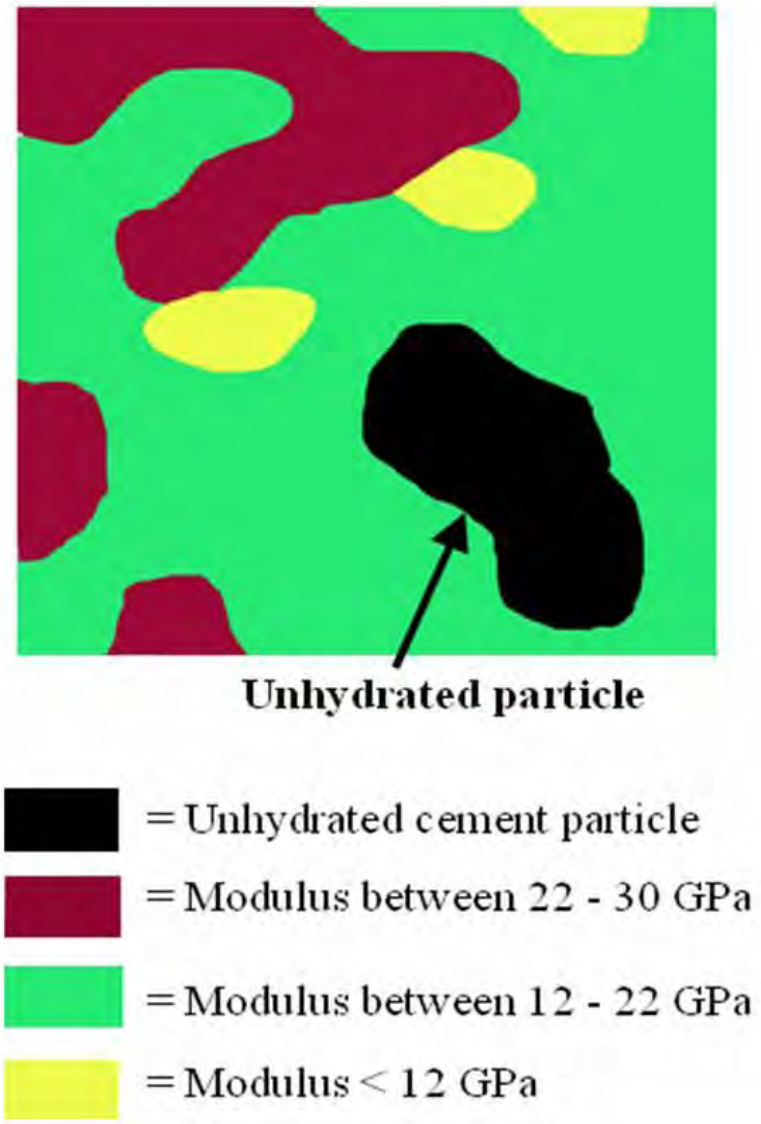

Figure 5.19. Modulus Map Drawn Based on the Indentation Results Shown in Figure 5.18, Cement Paste with 0.5 w/c

is performed for data analysis in the initial phase) will change the modulus for all the phases by the same percentage. Figure 5.18 shows the indentation modulus written on respective indent locations. In this particular case, areas of higher modulus were not found near cement particle. Similar analysis of a large number of indents made around cement particles along with the image

of the area associated on different parts of multiple samples revealed areas of low modulus as well as areas of high modulus adjacent to a cement particle. This is in contrast to what has been reported recently in the literature based on grid indentation. The reason may be attributed to lack of sufficient indents around cement particles made during grid indentation. There is a high chance of missing this area of lower stiffness while making indents. Therefore, a digitized map of properties will average out the modulus values resulting a ring like area around a cement particle with high stiffness. The indentation modulus of the C-S-H phase was found to be within a range between 10 GPa to 30 GPa and hardness of 0.25 GPa to 1 GPa. This matches well with the modulus and hardness reported by other researchers [20, 22, 24, 35, 56, 89]. Similar tests have been repeated on different samples and the results are reproducible. For ease of identifying areas of lower or higher stiffness, Figure 5.19 shows a modulus map of the area shown in 5.18. The map is drawn based on the calculated elastic modulus from each indent and modulus values are divided into four groups. Unhydrated cement particles were identified based on the image and its high elastic modulus. Indentation modulus of C-S-H is divided into two different groups, low stiffness C-S-H and high stiffness C-S-H based on existing literature [22, 24] and results of gird indentation data presented in a later section (Section 5.3.3). Areas of very low elastic modulus (< 12 GPa) is referred as porous phase which is related to the porosity of cement paste.

5.3.2.1. Different Water to Cement Ratio at Same Age of Curing

Figure 5.20 shows scanning electron microscopy images of 10-day-old polished cement paste samples captured in secondary electron mode. All three images are of the same magnification for ease of comparison. As expected, the sample with the lower water to cement ratio shows more

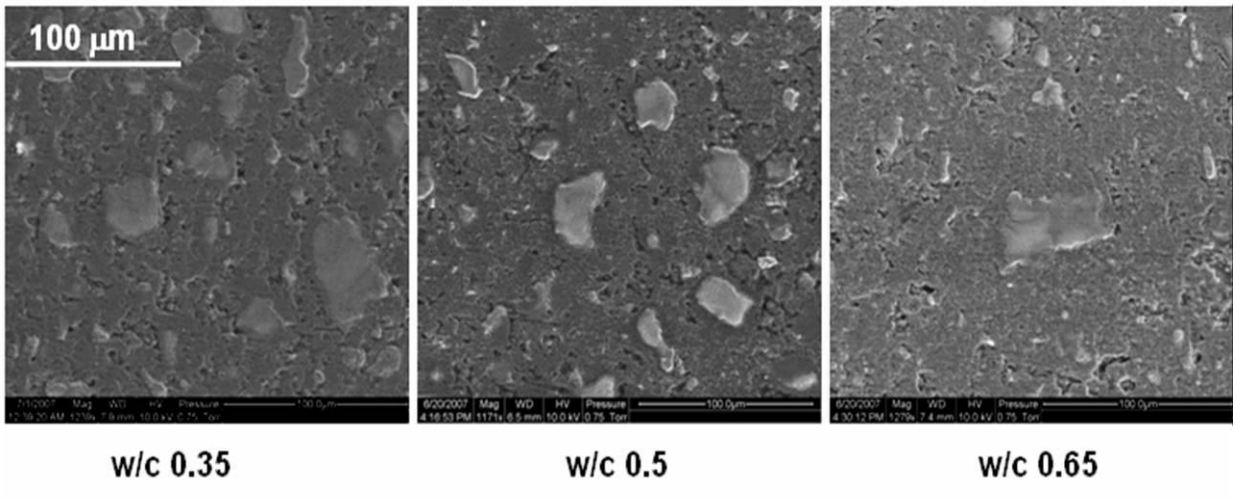

Figure 5.20. Scanning Electron Microscopy Image of Polished Cement Paste Sample with Different Water to Cement Ratio

remaining cement particles or unhydrated cement particles compared to samples with higher water to cement ratios. Figure 5.21 shows 60 μm $\times$ 60 μm AFM image of a 10-day-old cement paste sample with 0.35 w/c captured before indentation. Brighter areas represent unhydrated cement particles. At 0.35 w/c, many areas of the sample showed concentration of multiple cement particles closely packed, similar to the case shown in Figure 5.21. In this image, the modulus values calculated from the indentation data are written on the respective indent locations. Similar to the sample with 0.5 w/c, observed mechanical properties of the C-S-H gel in different areas were different and indentation modulus values were distributed within a range between 10 to 30 GPa. A modulus map of different phases was created following the method described in the previous section. Figure 5.22 shows the modulus map of the area shown in Figure 5.21 where different colors represent different range of elastic modulus. Concentration of higher modulus C-S-H phase was observed in the narrow areas between multiple cement particles. However, one can still observe areas of lower

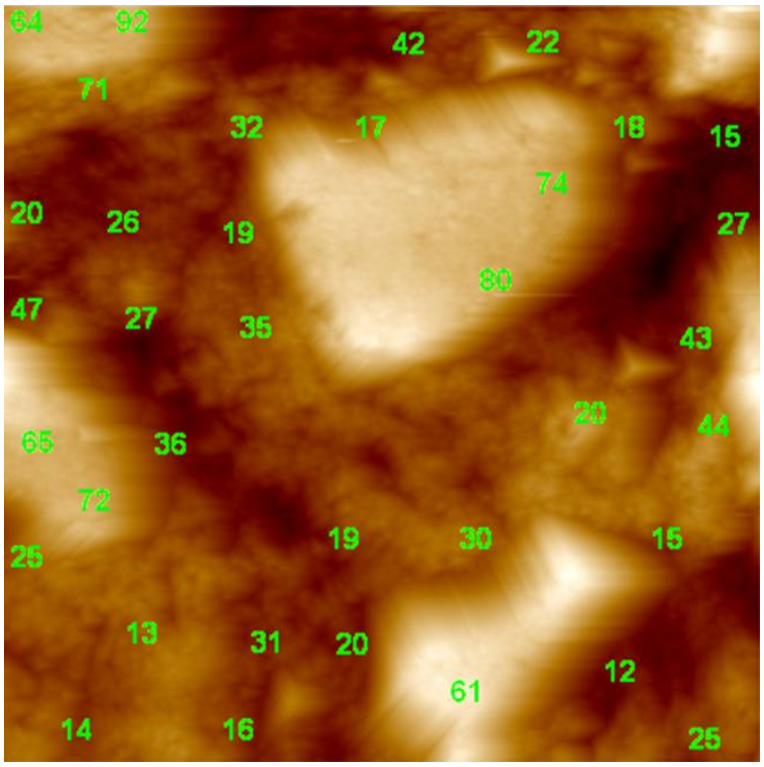

Figure 5.21. 60 μm $\times$ 60 μm Image of Cement Paste with 0.35 w/c Showing Indentation Modulus in GPa Written on Each Indent Locations

modulus C-S-H adjacent to an unhydrated cement particle. Figure 5.23 shows 60 μm $\times$ 60 μm image of a 10 days old cement paste sample with 0.65 water to cement ratio. In this image, the bright area near the center represents an unhydrated particle. Contrary to the case of cement sample with 0.35 w/c, higher water to cement ratio caused unhydrated cement particles to be distributed further apart in 3-dimensional space. This reduces the chance of overlapping between the zone around each cement particle and minimize interference among them. This facilitates study of the effects of each cement particle on adjacent C-S-H. Figure 5.23 shows modulus values calculated from the indentation data written on the respective indent locations. Similar to all the previous cases of w/c 0.5 and 0.35, observed mechanical properties of the C-S-H gel in different areas were different

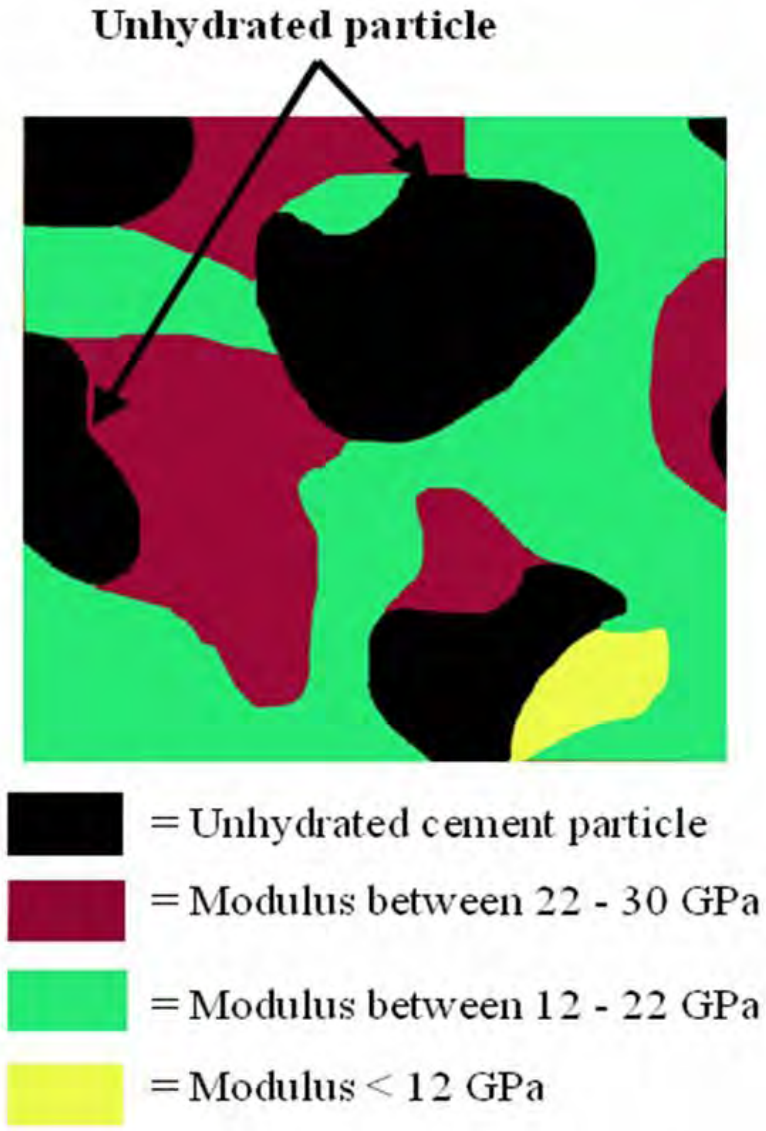

Figure 5.22. Modulus Map Drawn Based on the Indentation Results Shown in Figure 5.21, Cement Paste with 0.35 w/c

and modulus values were distributed in the similar range as before. Figure 5.24 shows a modulus map of the same area where different colors represent different range of indentation modulus. It was expected to see correlation between the indentation modulus of C-S-H and the distance from the unhydrated particle if there exists any. In Figure 5.24, one can see areas with high modulus

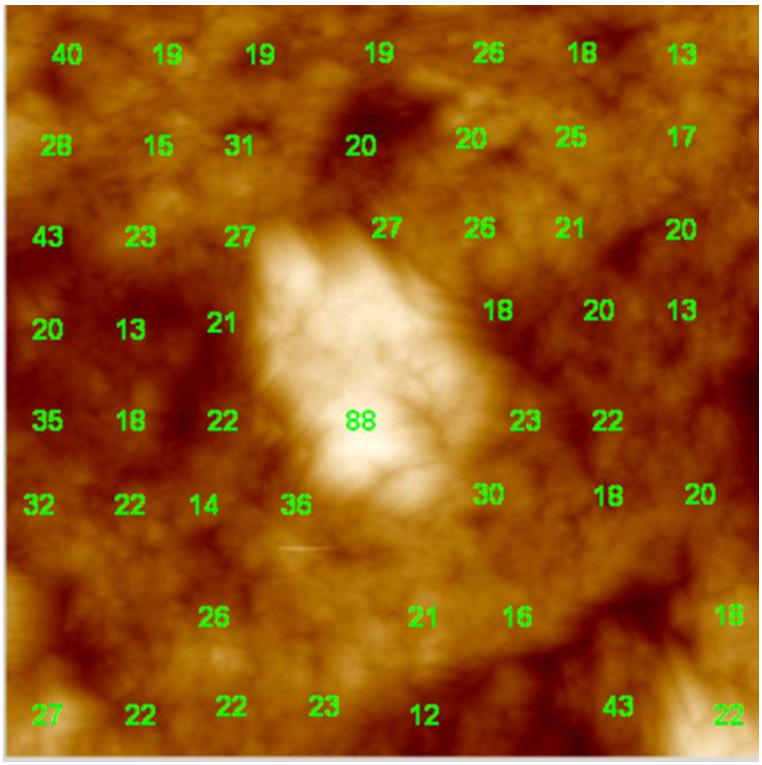

Figure 5.23. 60 μm $\times$ 60 μm Image of Cement Paste with 0.65 w/c Showing Indentation Modulus in GPa Written on Each Indent Locations

C-S-H at the top and bottom of the unhydrated particle. The rest of the area around the particle is surrounded by C-S-H with lower modulus. High modulus C-S-H was also present in other areas in the image which seems further away from the cement particle in this 2-dimensional representation of the sample. These areas of high modulus C-S-H could be due to the presence of cement particle underneath the surface or above the surface that was removed during polishing. Therefore, based on 2-dimensional representation of the sample, it is confirmed that low modulus C-S-H is always present around unhydrated cement particles with areas of high modulus C-S-H. However, it was not possible to conclude if high modulus C-S-H only exist near unhydrated cement particles. This implies that it is more relevant to call the two type of C-S-H reported in this study as low stiffness

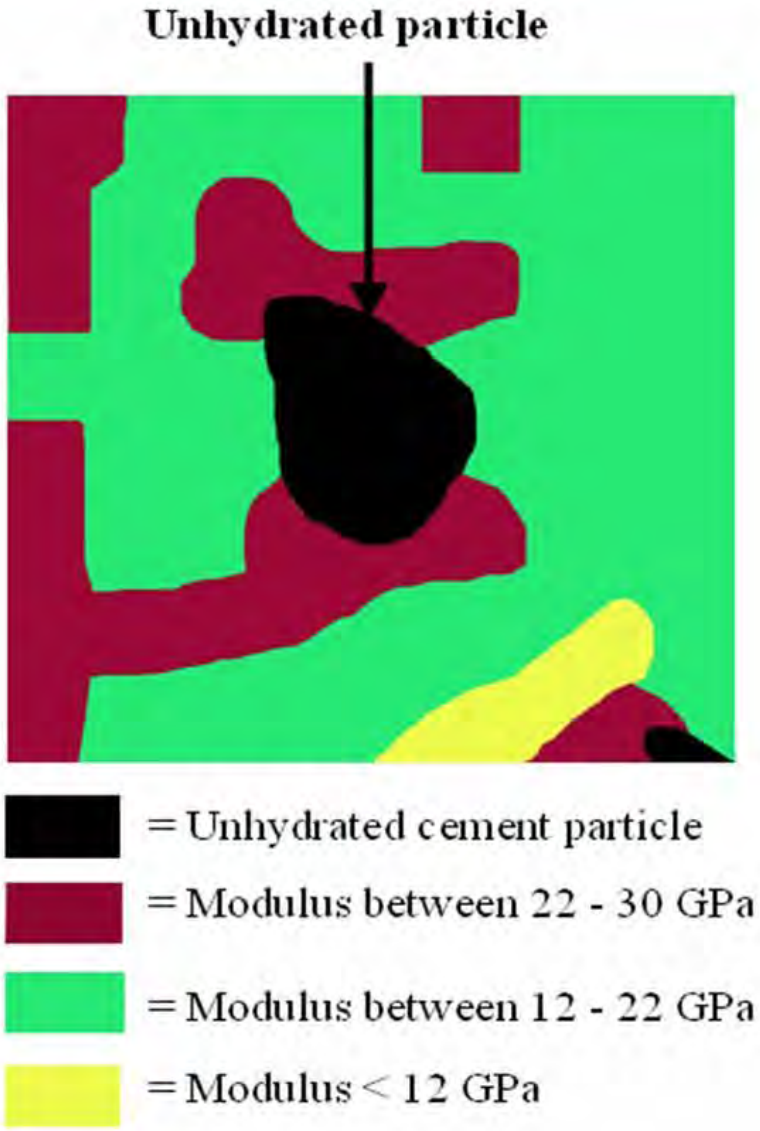

Figure 5.24. Modulus Map Drawn Based on the Indentation Results Shown in Figure 5.23, Cement Paste with 0.65 w/c

and high stiffness C-S-H (since only stiffness or modulus and hardness is measured in this study) as low density and high density C-S-H if density data is available for correlation [22, 24], than calling as inner product and outer product.

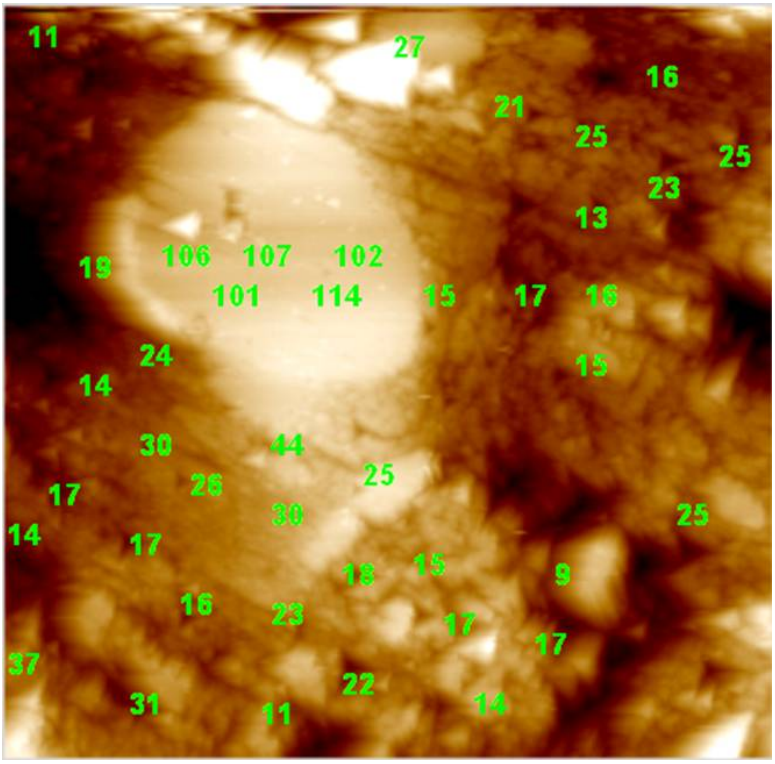

Figure 5.25. 60 μm $\times$ 60 μm Image of 6 months old Cement Paste with 0.5 w/c Showing Indentation Modulus in GPa Written on Each Indent Locations

5.3.2.2. Same Water to Cement Ratio at Different Age of Curing

Figure 5.25 shows a 60 μm × 60μm image of a 6 months old cement sample with 0.5 water to cement ratio. The bright area near the center represents unhydrated cement particle. It also shows the modulus values calculated from the indentation data. Figure 5.26 shows a modulus map of the same area. According to the literature, low density C-S-H or outer product form at the beginning of hydration period. With increase in curing age, the space available for formation of C-S-H decreases, leading to the development of inner product or high density C-S-H around the cement particle. Based on this theory, it was expected to see more high stiffness C-S-H around unhydrated cement particle after six months of curing than what have been seen for 10 days old

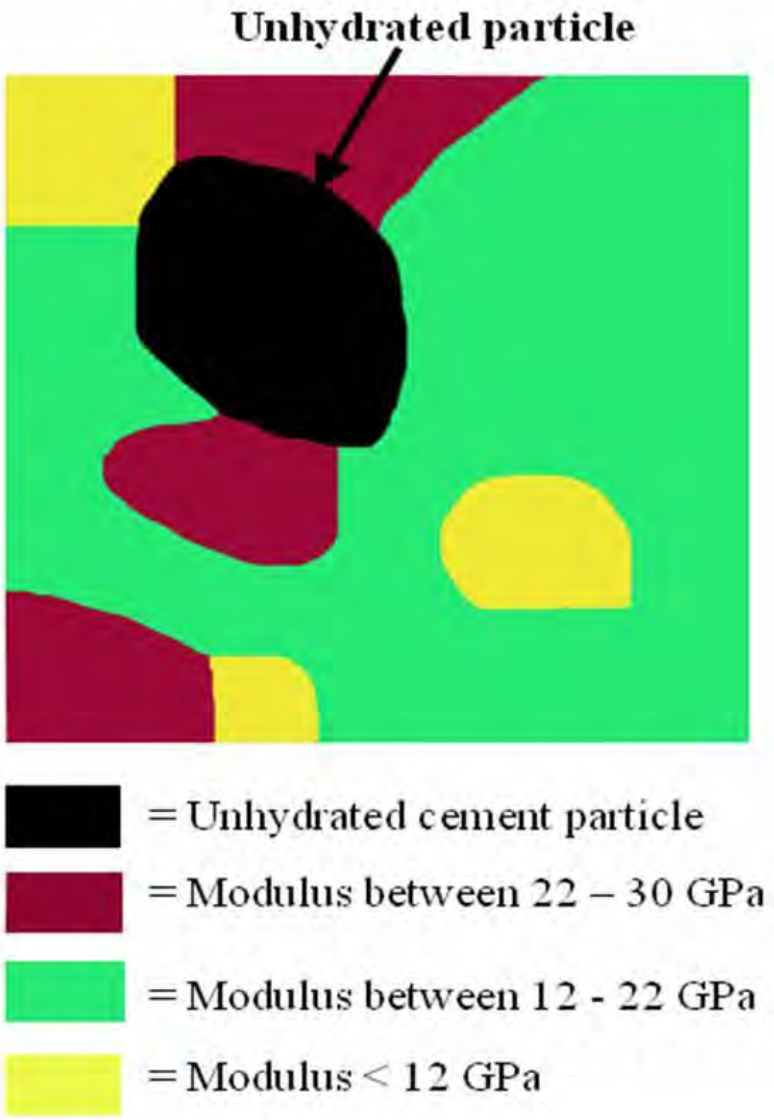

Figure 5.26. Modulus Map Drawn Based on the Indentation Results Shown in Figure 5.25, 6 months old Cement Paste with 0.5 w/c

samples with the same w/c. From the Figure (Figure 5.26), one can see areas with high stiffness C-S-H at the top and bottom of the unhydrated particle. The rest of the area around the particle is still surrounded by C-S-H with lower stiffness or lower modulus.

5.3.3. Grid Indentation: Data Analysis

5.3.3.1. Different Water to Cement Ratio at Same Age of Curing

Following the method described in Section 5.2.5, grid indentation was performed on 10-day-old samples with w/c 0.35, 0.5 and 0.65. On each sample, 3 different areas were chosen randomly to minimize site specific properties on the indentation data set. On each area, 144 indents were made in an array where 12 indents were made in each of the 12 rows. Spacing between the indents were 10 μm. An image of the whole area was captured to compare with the modulus map generated from the indentation data later. A huge volume of data was analyzed statistically to determine the phase properties and volume fraction of different phases in the cement paste microstructure. Figure 5.27 and Figure 5.28 shows probability distribution plot of the indentation modulus and hardness respectively. The bin size for the distribution was set at 2.5 GPa and 125 MPa for the elastic modulus and hardness respectively. Reducing it further would result in too irregular distributions due to limited number of data available in each bin, while further increase would result in loss of detail. Number of bins created in such way satisfy the criteria ($3n - 1 \leq m \leq N$) provided in Section 5.2.5. Indentation data was analyzed in terms of their frequency distributions. As C-S-H and other phases present in a cement sample are expected to have a unique set of modulus and hardness, both distributions show a similar trend. The modulus ranged from 10 GPa to 30 GPa and hardness ranged from 0.25 GPa to 1 GPa, which corresponds to the main phase in cement paste, C-S-H. Furthermore, both modulus and hardness plot show a peak corresponding to calcium hydroxide at a modulus around 33 GPa and hardness around 1.5 GPa.

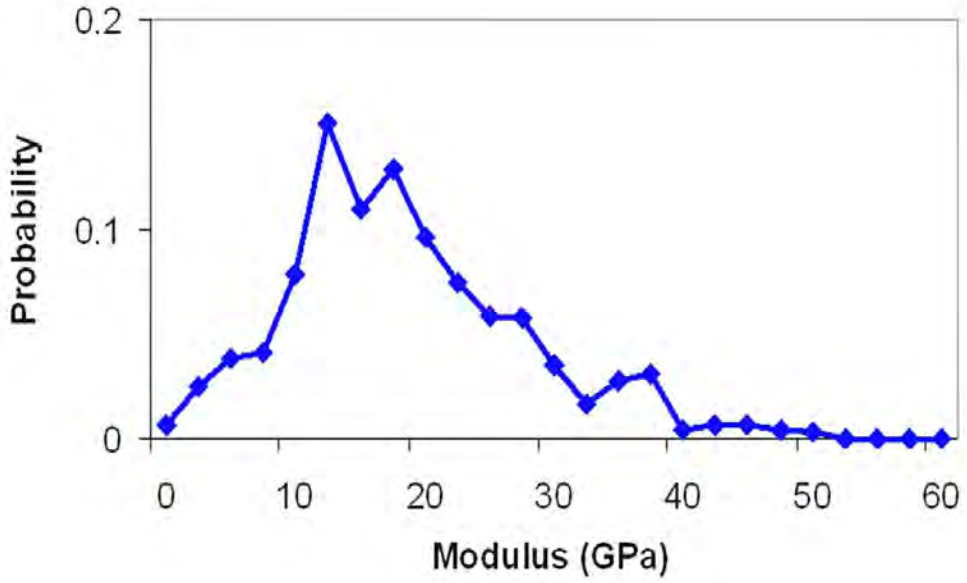

Figure 5.27. Probability Distribution of Indentation Modulus for Cement Sample with w/c 0.5

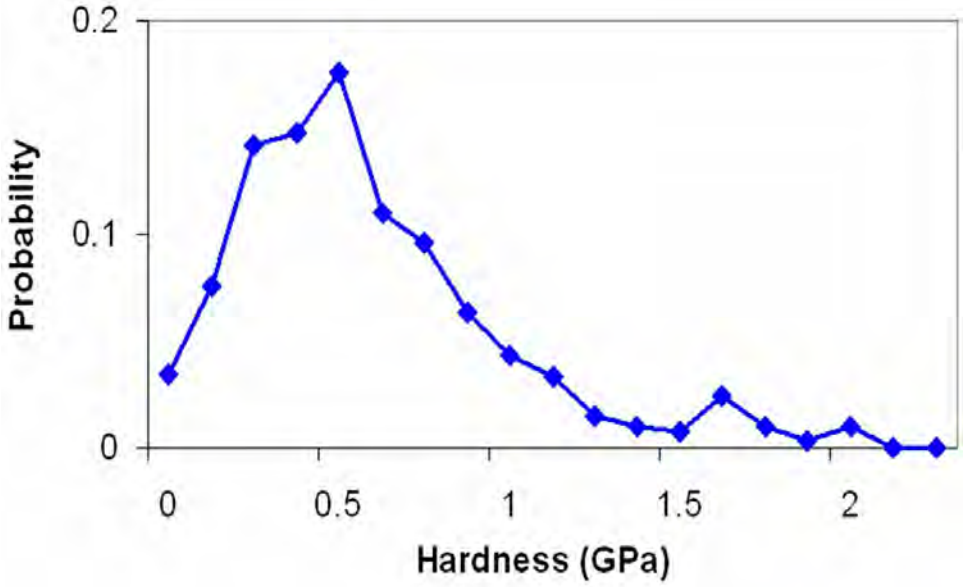

Figure 5.28. Probability Distribution of Hardness for Cement Sample with w/c 0.5

Figure 5.29 shows a contour map of indentation modulus created from the gird indentation data. Similar to what has been reported in some recent papers [20, 22, 24, 89], modulus map created based on grid indentation results shows ring like areas of higher modulus around unhydrated cement particle. As mentioned in Section 5.2.6, this is due to less number indents around unhydrated cement particles and the averaging effect of contour mapping. This proves the limitation of grid indentation to show localized effects in small areas. However, this is a good technique to determine volume fraction of different phases.

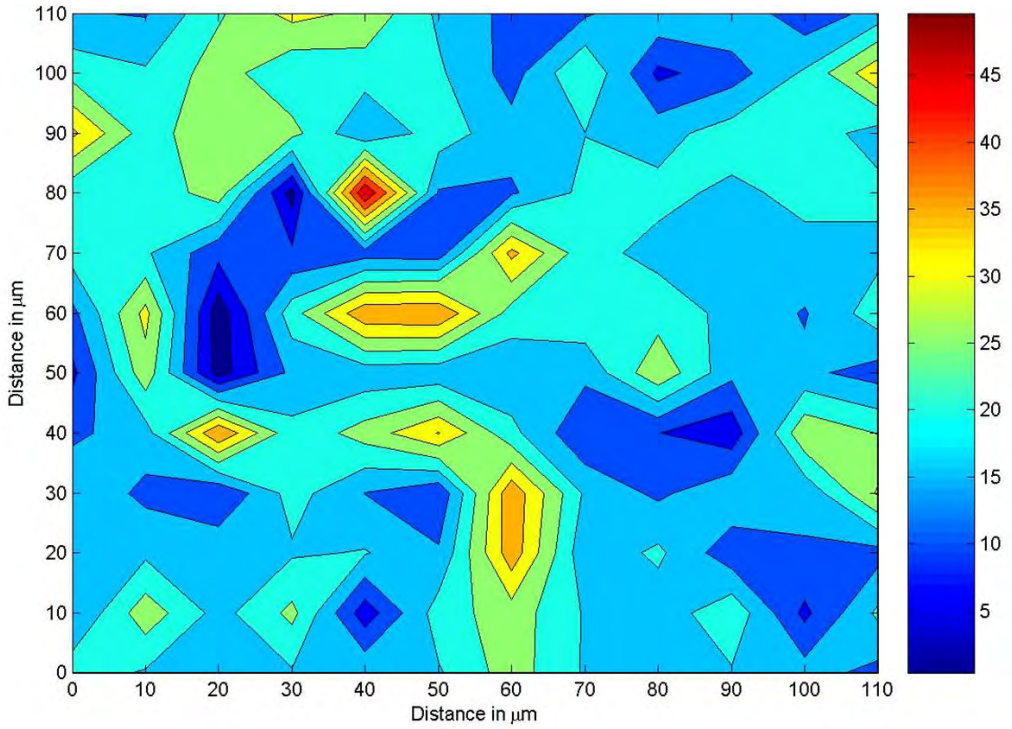

Figure 5.29. Contour map of Indentation Modulus Based on Grid Indentation on 120 μm $\times$ 120 μm area of Cement Sample with w/c 0.5

Figure 5.30 and Figure 5.31 compares probability distribution plot of indentation modulus and hardness respectively for cement paste samples with w/c 0.35, 0.5 and o.65. At higher water to

cement ratio, volume fraction of low modulus and low hardness phases are much higher. With a decrease in water to cement ratio, both modulus and hardness plots were shifted to the right. Non-linear optimization problem $P(1)$ described in Section 5.2.5, was used to fit 4 normal distributions representing four phases: porous phase, low and high stiffness C-S-H and calcium hydroxide. A peak analyzing protocol from a commercially available software called Origin was used to decompose the overall probability distribution (p.d.f.) obtained into individual probability distribution (p.d.f) of each phase. Figure 5.32 shows overall probability distribution obtained from nanoindentation data of cement paste with w/c 0.35, 4 fitted normal distributions and cumulative distribution of the 4 fitted distribution. Comparison of the experimentally obtained overall distribution with the cumulative of the 4 fitted normal distribution in Figure 5.32 shows the goodness of fit. Reduced R-square statistics was 0.92 which is very close to 1 (closer the value of reduced R-square to 1 denotes better fit). The area under each fitted normal distribution represents volume fraction of the associated phase. This analysis was repeated for w/c 0.5 and 0.65. Figure 5.33 and Figure 5.34 shows experimentally obtained overall probability distribution, 4 fitted normal distributions and a cumulative distribution of the 4 fitted distributions for w/c 0.5 and 0.65 respectively.

Table 5.2 summarizes the results of statistical analysis on nanoindentation data. Average modulus of 4 phases; a porous phase with very low modulus and hardness, a low stiffness C-S-H phase, a high stiffness C-S-H phase and calcium hydroxide and change in volume fraction with change in water to cement ratio are presented. It was very interesting to note that the average modulus of these phases did not change much with water to cement ratio, although a decrease in volume fraction of the porous phase with decrease in water to cement ratio was very significant. Furthermore,

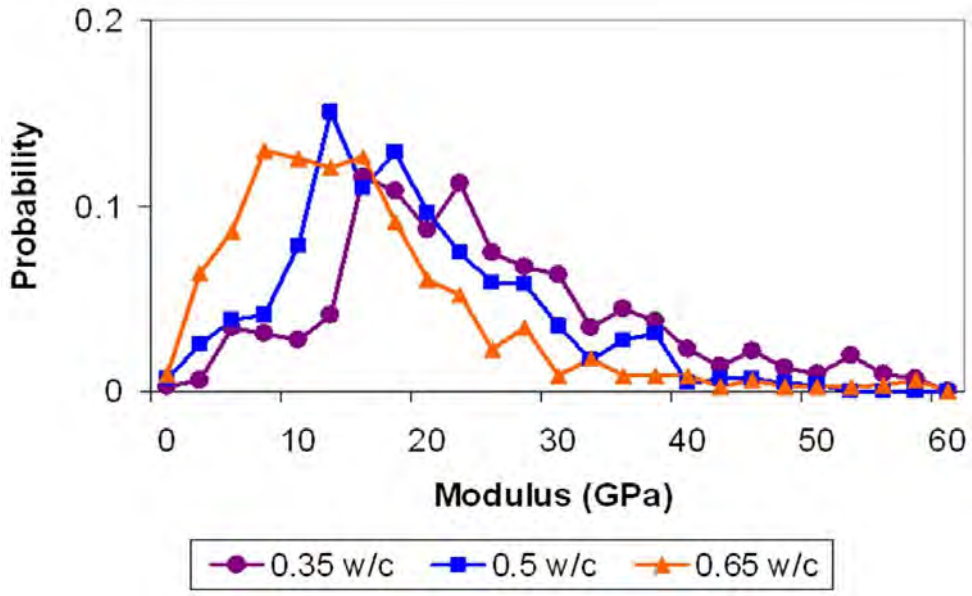

Figure 5.30. Comparison of Indentation Modulus of Cement Paste with Different w/c

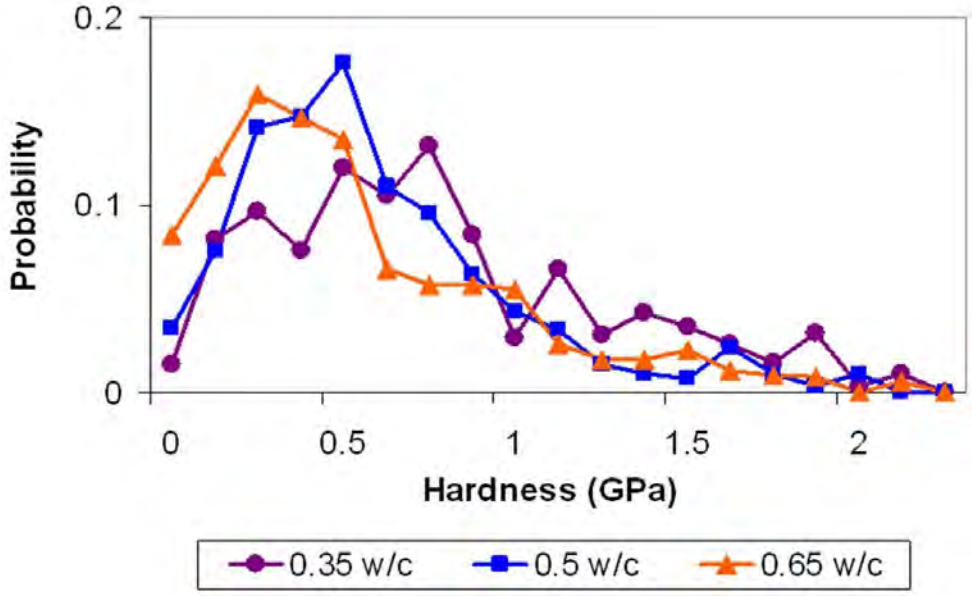

Figure 5.31. Comparison of hardness of Cement Paste with Different w/c

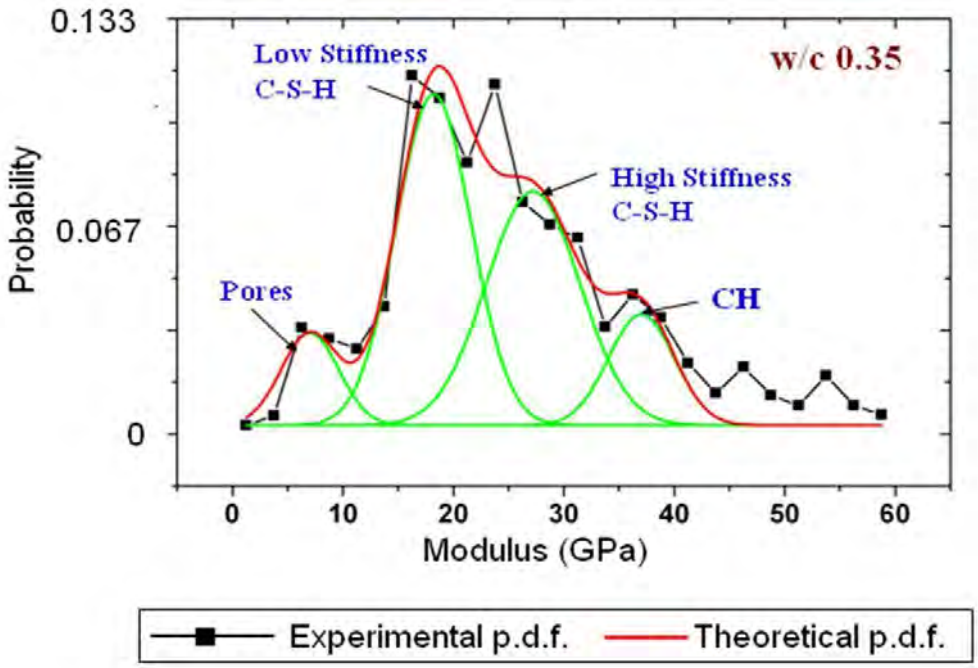

Figure 5.32. Cement Paste with w/c 0.35: 4 Fitted Normal Distributions Representing 4 Phases: Porous Phase, Low and High Stiffness C-S-H and Calcium Hydroxide

the volume fraction of low stiffness C-S-H decreased and the volume fraction of high stiffness C-S-H increased with decrease in w/c. The decrease in volume fraction of low stiffness C-S-H in w/c 0.65 may seem anomalous, but the increase in volume fraction of porous phase was very high in this case and comparison of sum of porous phase and low stiffness C-S-H phase shows increase with increase in w/c.

5.3.3.2. Same Water to Cement Ratio at Different Curing Ages

To study effects of curing age on average phase properties and volume fraction of different phases in cement paste, grid indentation following the method described in Section 5.2.5 was performed on 1 month old samples with w/c 0.5. Around 420 indents were made on 3 different randomly chosen areas to minimize site specific properties on the indentation data set. In each

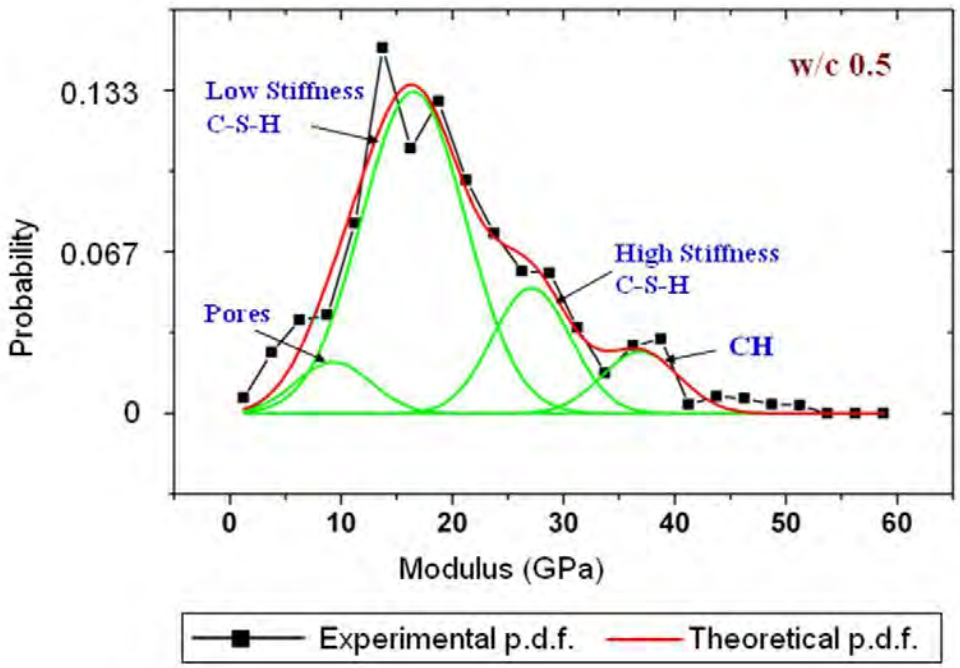

Figure 5.33. Cement Paste with w/c 0.5: 4 Fitted Normal Distributions Representing 4 Phases: Porous Phase, Low and High Stiffness C-S-H and Calcium Hydroxide

area, 144 indents were made in an array where 12 indents were made in each of the 12 rows. Spacing between each indents were 10 μm. Figure 5.35 compares probability distribution plot of indentation modulus for cement paste with 0.5 w/c at two different curing age. It is clear from the plot that modulus distribution for a 10-day-old paste and a 1 month old paste is very similar. Most of the data is found to be within a range of modulus between 10 GPa to 30 GPa and one additional peak corresponding to calcium hydroxide at a modulus around 33 GPa is visible.

Statistical analysis was performed using the peak analyzing protocol of Origin. Table 5.3 summarizes the average modulus of 4 phases and change in volume fraction with change in curing age. Interestingly, the average modulus of the phases did not change much with curing age. Furthermore, the volume fraction of different phases did not show significant change either.

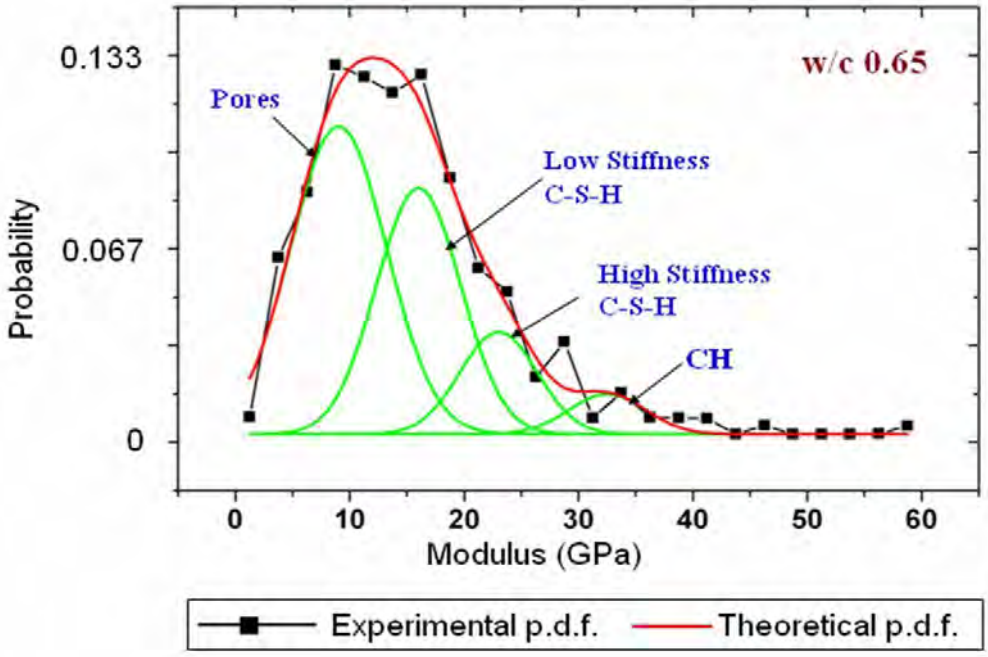

Figure 5.34. Cement Paste with w/c 0.65: 4 Fitted Normal Distributions Representing 4 Phases: Porous Phase, Low and High Stiffness C-S-H and Calcium Hydroxide

5.4. Discussion and conclusions

From nanoindentation experiments, unhydrated cement particles were found to have an elastic modulus around 100 GPa which is much higher than its products of hydration. The elastic modulus of unhydrated cement particles found in this study is little lower than the results reported by Velez *et al.* [85] which is attributed to the porosity within cement particles. The modulus of the C-S-H phase was found to be within a range between 10 GPa to 30 GPa and a hardness of 0.25 GPa to 1 GPa. This matches well with the modulus and hardness reported by other researchers [20, 22, 24, 35, 56, 89]. Nanoindentation with in-situ imaging was found to be very effective to determine the location of specific properties. For example, concentration of high stiffness C-S-H was found near unhydrated cement particles. Particularly, in the case of cement paste with lower w/c (w/c = 0.35),

		w/c = 0.35	w/c = 0.5	w/c = 0.65
Porous Phase	Elastic Modulus	9.3±2.6	9.4±3.4	9.1±4.2
	Volume Fraction (%)	9	10	46
Low Stiffness C-S-H	Elastic Modulus	18.2±3.4	16.5±4.7	16±3.7
	Volume Fraction (%)	39	63	36
High Stiffness C-S-H	Elastic Modulus	27.2±5.4	27.1±3.5	23.5±3.4
	Volume Fraction (%)	41	19	14
Calcium Hydroxide	Elastic Modulus	37.8±3.9	36.9±3.5	32.5±3.4
	Volume Fraction (%)	11	8	4

Table 5.2. Change in Volume Fraction of Different Phases with Change in Water to Cement Ratio.

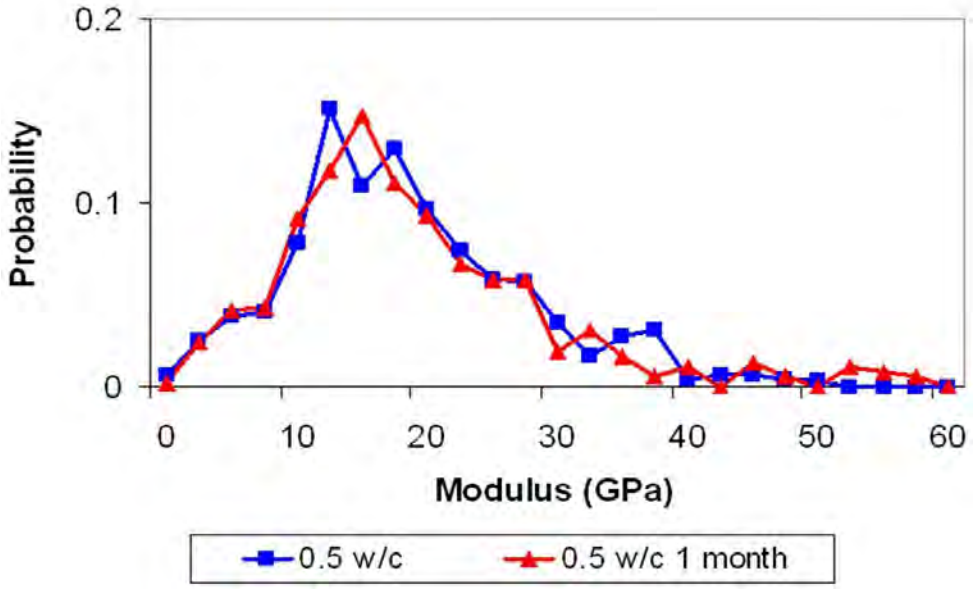

Figure 5.35. Probability Distribution of Modulus for Cement Sample with w/c 0.5 at Two Different Curing Age

		10 Days	1 Month
Porous Phase	Elastic Modulus	9.4±3.4	9.4±4.2
	Volume Fraction (%)	10	8
Low Stiffness C-S-H	Elastic Modulus	16.5±4.7	16.5±3.7
	Volume Fraction (%)	63	65
High Stiffness C-S-H	Elastic Modulus	27.1±3.5	26±3.4
	Volume Fraction (%)	19	20
Calcium Hydroxide	Elastic Modulus	36.9±3.5	33±3.4
	Volume Fraction (%)	8	7

Table 5.3. Change in Volume Fraction of Different Phases with Change in Water to Cement Ratio.

a concentration of higher modulus C-S-H was observed in the narrow areas between multiple cement particles. Based on nanoindentation on cement paste with three different w/c, 0.35, 0.5 and 0.65, presence of high modulus C-S-H along with some areas of low modulus C-S-H around cement particles were confirmed. High stiffness C-S-H was also found randomly scattered at a distance from unhydrated cement particles. Therefore, based on only 2-dimensional image of the sample surface, it was not possible to conclude if high modulus C-S-H only exist near unhydrated cement particles.

Grid indentation was used to make large number of indents on each type of sample for statistical analysis. As C-S-H and other phases present in a cement sample are expected to have a unique set of modulus and hardness, the distribution of modulus and hardness show similar trend. Most

of the data was found to be within a range of modulus between 10 GPa to 30 GPa and hardness of 0.25 GPa to 1 GPa, which corresponds to the main phase in cement paste, C-S-H. Furthermore, both modulus and hardness plot show a peak corresponding to calcium hydroxide at a modulus around 33 GPa and hardness around 1.5 GPa. Applying expectation maximization scheme, average modulii of four phases; a porous phase with very low modulus and hardness, a low stiffness C-S-H phase, a high stiffness C-S-H phase and calcium hydroxide were found to be around 10 GPa, 16 GPa, 26 GPa and 35 GPa respectively. It was found that average modulii of these phases do not change with water to cement ratio or curing age. However, the volume fraction of different phases changed with change in water to cement ratio. Significant decrease in volume fraction of porous phase was observed with decrease in water to cement ratio. Volume fraction of low stiffness C-S-H decreased and volume fraction of high stiffness C-S-H increased with decrease in w/c. Interestingly, the volume fraction did not show significant change with curing age. This indicates that C-S-H has the same average nanomechanical properties irrespective of water to cement ratio or degree of hydration. With different water to cement ratio, only volume fraction of different phases change, and higher percentage of high modulus phase with excess unhydrated cement particles leads to higher macroscopic strength. Furthermore, with increase in curing age, both the low stiffness and high stiffness C-S-H form keeping the relative volume same. Macroscopic strength increase may be attributed to the reduction in macro-porosity due to formation of both the low stiffness and high stiffness C-S-H.

Chapter 6 Determination of Local Mechanical Properties of ITZ

6.1. Introduction

In concrete, paste works as the glue that holds aggregates together to behave as a whole. However, this composite action depends on a thin layer that is believed to exist between the aggregates and the paste matrix, referred to as the interfacial transition zone (ITZ). This is the region of cement paste around aggregates developed due to the so called "wall effect" [4, 9]. Relatively smooth surfaces of large aggregates act as wall and interfere with the packing of cement particles against it (Figure 6.1). According to the literature, the w/c ratio within the ITZ is higher than elsewhere in the paste matrix and the large crystals of $Ca(OH)_2$ introduce higher porosity at the interface [57]. This is a region of gradual transition where the effective thickness of the region varies with the microstructural feature being studied, and with degree of hydration [72]. In many studies,

it was concluded that in ordinary Portland cement concrete, the ITZ consists of a region up to 50 μm around each aggregate with fewer unhydrated particles, less calcium-silicate-hydrate, higher porosity, and greater concentration of calcium hydroxide and ettringite. The microstructure of an interfacial transition zone in concrete is presented schematically in Figure 6.2. The ITZ is believed to be weaker than the bulk paste matrix. When the material is subjected to loads, microcracks may appear within the region of the ITZ. This leads to the quasi-brittle nature of concrete. Development of microcracks also reduces both the strength and the stiffness of the composite [47]. In normal strength concrete, the failure plane always passes through the ITZ (Figure 6.3).

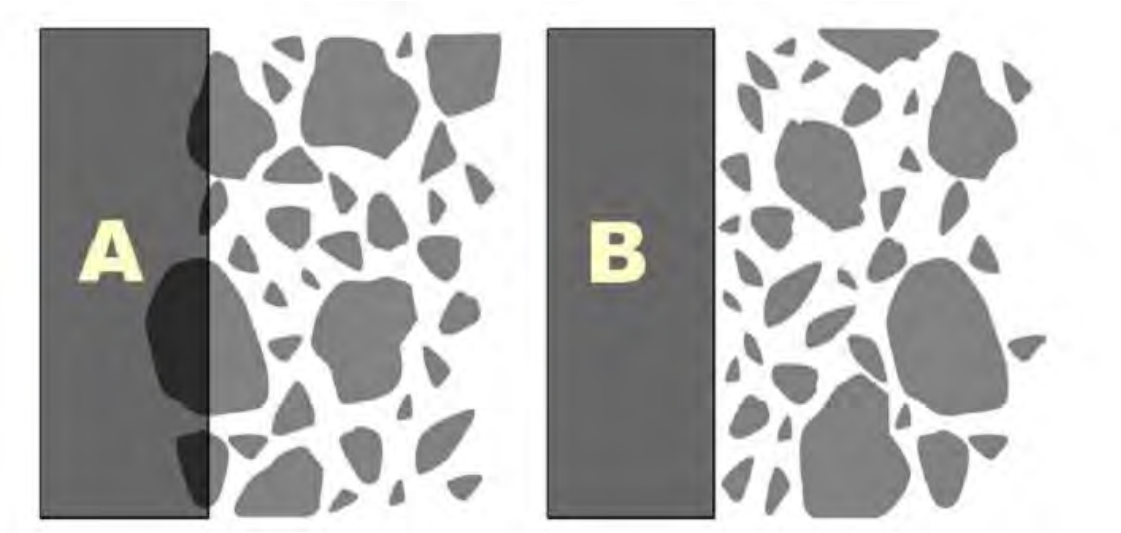

Figure 6.1. Schematic Diagram Showing Wall Effect of Aggregate [72]

6.1.1. Factors Affecting Properties of Interfacial Transition Zone

The quality of the bond between the paste matrix and aggregate is influenced by the shape, size, surface roughness, mineral and chemical composition, porosity, and surface moisture content of aggregates. Generally, a rougher surface of crushed particles results in a better bonding due to

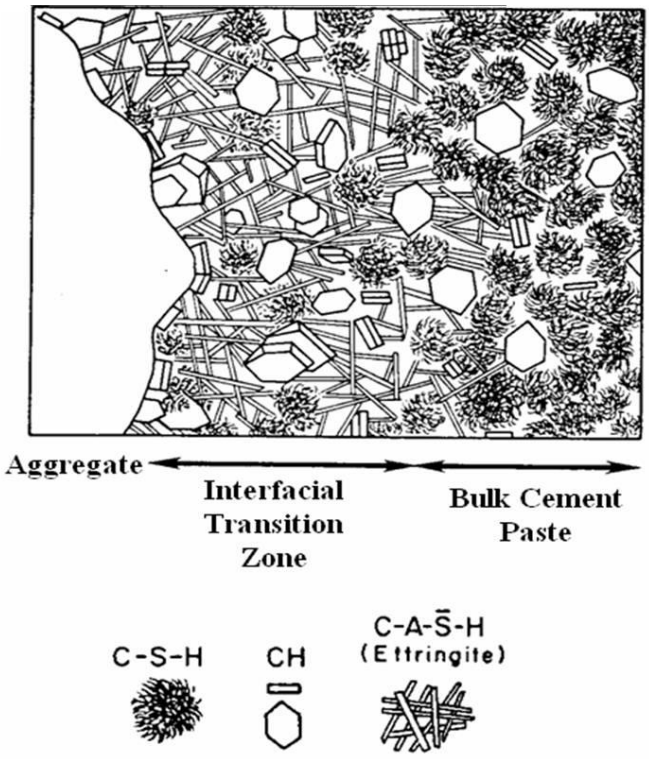

Figure 6.2. Schematic Diagram of Interfacial Transition Zone [47]

mechanical interlocking. Limestone, dolomite, and siliceous aggregates may have stronger ITZ because of the existence of chemical bonds. Ryu et al. studied effects of the specific gravity of aggregates and w/c on the ITZ [71]. Lightweight aggregates with a porous outer layer lead to the migration of mobile ions towards the surface to form a dense ITZ, so that a better bond can be obtained. There are a lot of arguments about the effect of aggregate size on the properties of the ITZ. Some researchers argued that the thickness of the ITZ depends largely on the size of the aggregate. During mixing, dry cement particles are unable to become closely packed against the relatively large aggregate, thus a coarse aggregate may have a thicker ITZ (Scrivener, et al., 1988; and Ping, et al., 1991). Elsharief et al. studied effects of w/c, age and aggregate size on

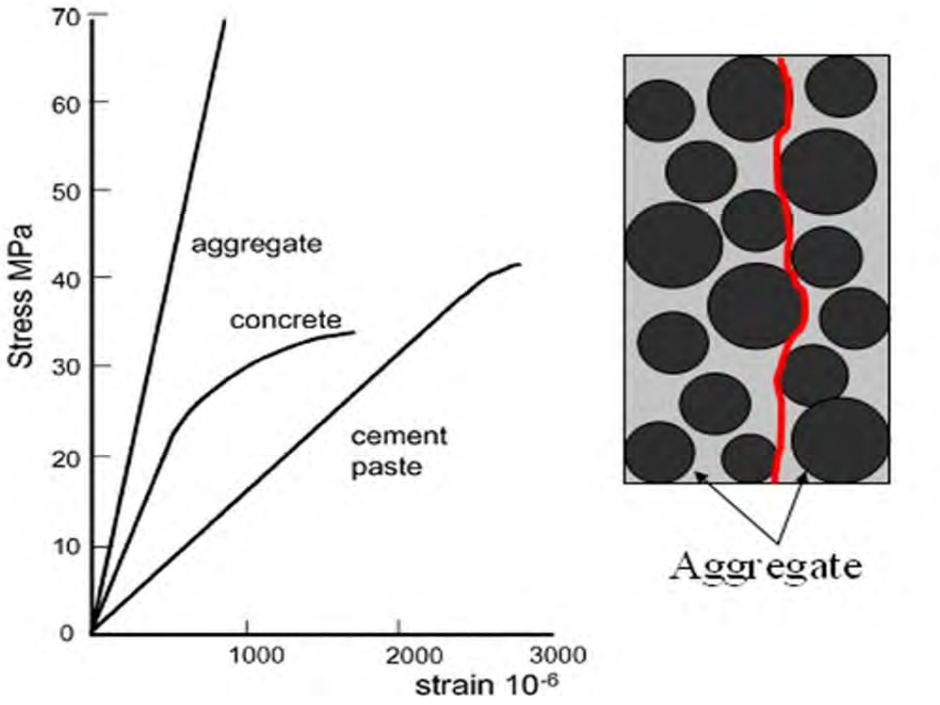

Figure 6.3. Effects of the ITZ on Mechanical Properties of Concrete [72]

properties of the ITZ between normal weight aggregates and bulk cement paste using scanning electron microscopy [28]. They reported reduction in porosity by changing w/c from 0.55 to 0.4 and by reducing size of aggregates. For w/c 0.55, they reported the ITZ being more porous compared to the bulk paste at 180 days than at 7 days and vice verse for w/c 0.4. Simeonov et. al also reported effects of the water to cement ratio on thickness and elastic modulus of the ITZ from their analysis of literature data using a two phase model for concrete [73]. They reported the ITZ being thinner and stronger than the bulk matrix for w/c 0.3 to 0.4, but weaker than bulk for w/c less than 0.4. Contrary to the previous two studies, Asbridge et al. reported lower microhardness of the ITZ than the bulk for w/c 0.4 to 0.6. Furthermore, the difference between the microhardness of

the ITZ and the bulk paste decreases with increase in the water to cement ratio and they are almost similar at w/c 0.6 [3]. Some researchers argued that the thickness of the ITZ depends on the particle size distribution of binder (cement powder, fly ash, silica fume, etc) instead of the aggregate size (Garboczi, et al, 1998). Asbridge et al. reported about increase in Knoop microhardness measured in the ITZ in model mortar with 10 percent metakaolin [3]. But the ITZ was still reported to be weaker than the bulk matrix at w/c of 0.4 and 0.5. However, at w/c 0.6, they reported higher Knoop microhardness at the ITZ and bulk matrix. Jiang studied properties of the ITZ in high volume fly ash concrete (HVFA). From x-ray diffraction, scanning electron microscopy imaging and bond strength test, he reported that there is no obvious transition zone between aggregate and HVFA paste [45]. Similar study was done by Kuroda et al. [42]. Considering the fracture properties of concrete, Prokopski et al. reported that the ITZ in silica fume concrete is stronger than that in Portland cement concrete [67]

6.1.2. Local Mechanical Properties of the ITZ: Literature Review

Simeonov et al. [73] reported the influence of ITZ on the overall elastic properties of mortar and concrete. In normal strength concrete, it is considered to be the weakest link in the mechanical system [34, 72]. Although it is widely accepted that the properties of the ITZ have to be taken into account in modeling the overall mechanical properties of concrete [4, 34, 43, 44, 46, 55, 73, 76], it is difficult to determine its local mechanical properties because of the complexity of the structure and the constraints of existing measurement techniques [68]. Most of the time, the modulus of the ITZ is assumed to be uniform and less than that of the paste matrix by a constant factor [43]. This factor is assumed to have a value between 0.2 and 0.8, although there is not enough theoretical or

experimental evidence to support this assumption [76]. In their model, Lutz et al. assumed that the elastic properties vary smoothly as a power law within the ITZ. By fitting macroscopic bulk modulus data, they found that the modulus of the ITZ is 30-50 percent less than that of the bulk matrix. In some recent studies, attempts were made to determine the local mechanical properties of the ITZ using microindentation or microhardness testing [3, 88, 89]. Nadeau reported that elastic modulus of the ITZ in mortar is 10 to 20 percent of that of the bulk paste based on his generalized self-consistent model [55]. Asbridge et al. reported about 20 percent reduction in Knoop microhardness in the ITZ than the bulk matrix at w/c of 0.4 and 0.5 [3]. At w/c 0.6, however, they reported similar Knoop microhardness at the ITZ and the bulk matrix. In their study, the width of indentation was reported as 10-15 μm, which is comparable with the width of the ITZ itself. Therefore, though it revealed some information, effects of adjacent phases on hardness results makes microhardness test not suitable for determining local properties of the ITZ. There is still very little information available at the nanoscale properties of the ITZ.

6.2. Experimental Detail

Since different factors such as water to cement ratio, age of sample, aggregate type and size affect properties of interfacial transition zone, it was decided to keep most of them constant and vary one or two factors at a time. Water to cement ratio was fixed at 0.5, age of the sample was fixed at 1 month. The ITZ between cement paste and three different types of aggregates were studied. Model mortar samples were made using Type I Portland cement and river sand. Sand particles were sieved and only particles in the size range of 1.18 mm to 2.36 mm (i.e sand passing sieve #8 and retained on sieve #16) were used. Two types of model concrete samples were made, one with

round gravel and the other one with limestone aggregates. Both round gravels and limestone were sieved and aggregates in the size range of 9.5 mm to 4.75 mm (i.e. passing sieve #3/8 and retained on sieve #4) were separated. From this, aggregates with an approximate size of 5 mm were used to make model concrete samples. All the samples were 1 inch $\times$ 1 inch $\times$ 0.5 inch. Half of the model concrete samples had multiple aggregates where as rest of them had just one aggregate at the center. Samples were cured under water at 25°C. For nanoindentation, samples were prepared following the method described in Chapter 4.

6.2.1. Study of the ITZ using Scanning Electron Microscopy

Figure 6.4 shows scanning electron microscopy image of polished model concrete samples. In most of the areas, there were large voids adjacent to an aggregate or crack running along the interface. Similar results was reported by other researchers. For example, Figure 6.5 shows SEM image of interfacial transition zone reported by Birgisson [6]. This proves weak bonding between aggregates and cement paste. Figure 6.6 shows areas around aggregates where no obvious interfacial zone was found except there were less number of unhydrated cement particles. Furthermore, no difference in porosity was found in these areas. From SEM imaging, no difference in the ITZ was found in samples with multiple coarse aggregates and samples with one coarse aggregate at the center. Therefore, model concrete with one aggregate was chosen for subsequent nanoindentation studies.

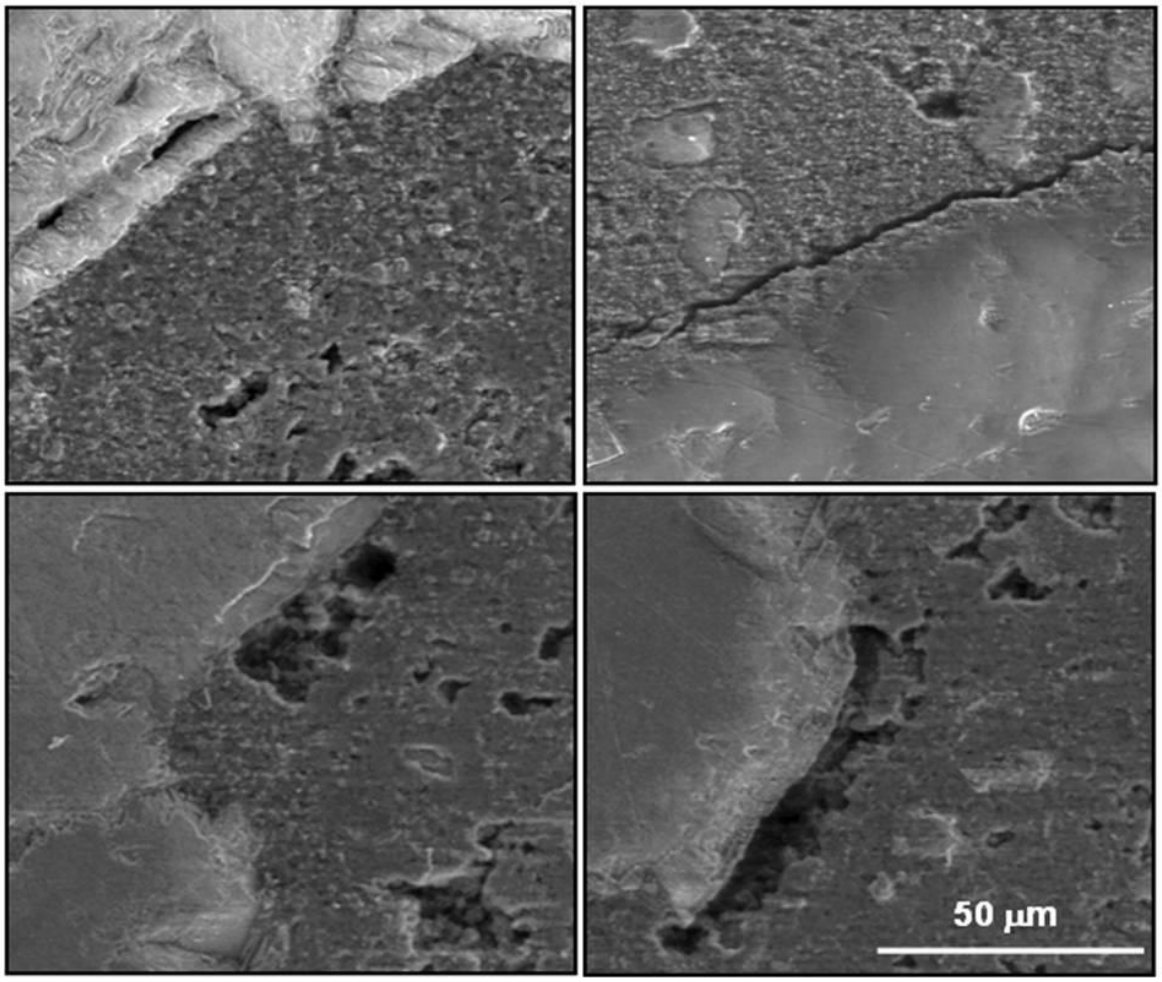

Figure 6.4. SEM Image of the ITZ Showing Cracks and Large Voids

6.3. Nanomechanical Properties at the Interfacial Transition Zone

6.3.1. ITZ between Sand and Cement Paste

Figure 6.7 shows a image of the ITZ between a sand particle and cement paste. Nanoindentation with imaging, as discussed in Section 5.2.4, proved to be indispensable to identify the narrow area around aggregate and position the indenter in the same area. After imaging, approximately 40 locations were chosen for indentation on the sand particle, and on cement paste. In the image, the

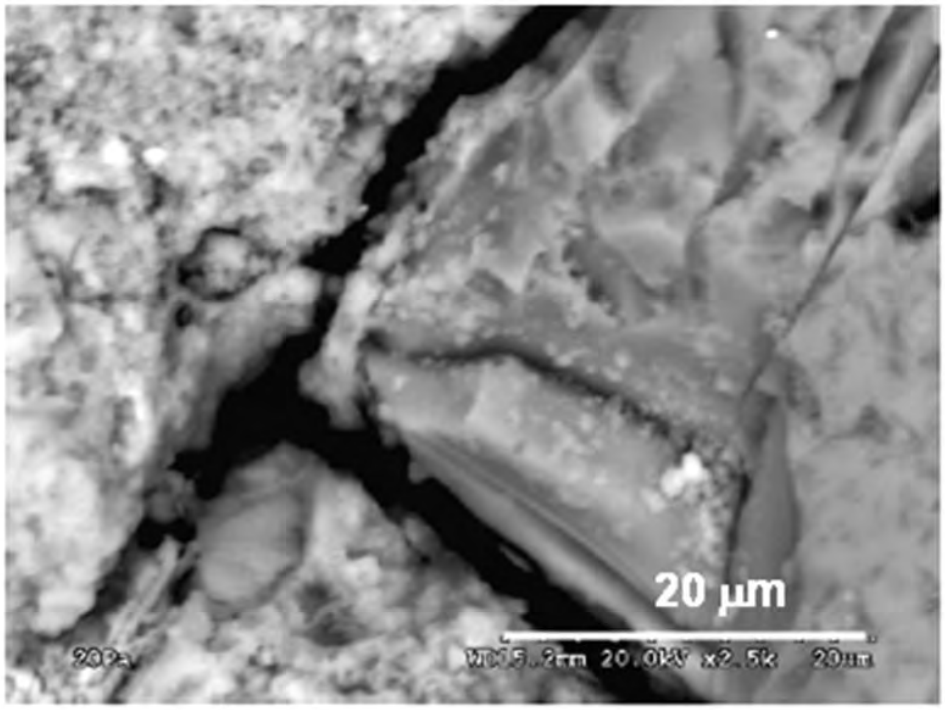

Figure 6.5. Interfacial Transition Zone Showing Poor Bonding [6]

modulus values obtained from the indents are written at the indent location. Part of the interfacial zone shows lower modulus and the modulus seems to increase with distance from sand. Though there are areas near the sand particle that seem less porous from the image and at the same time higher modulus was observed, like the area at the top left hand corner of the image.

6.3.2. ITZ between Gravel and Cement Paste

Model concrete samples were used for detailed analysis of the properties of the ITZ. Figure 6.8 shows the SEM image of cement paste adjacent to gravel and results of nanoindentation on the same area. From the SEM image, no obvious differences in properties were found at the interface. To determine nanomechanical properties, exactly the same area was identified using the AFM

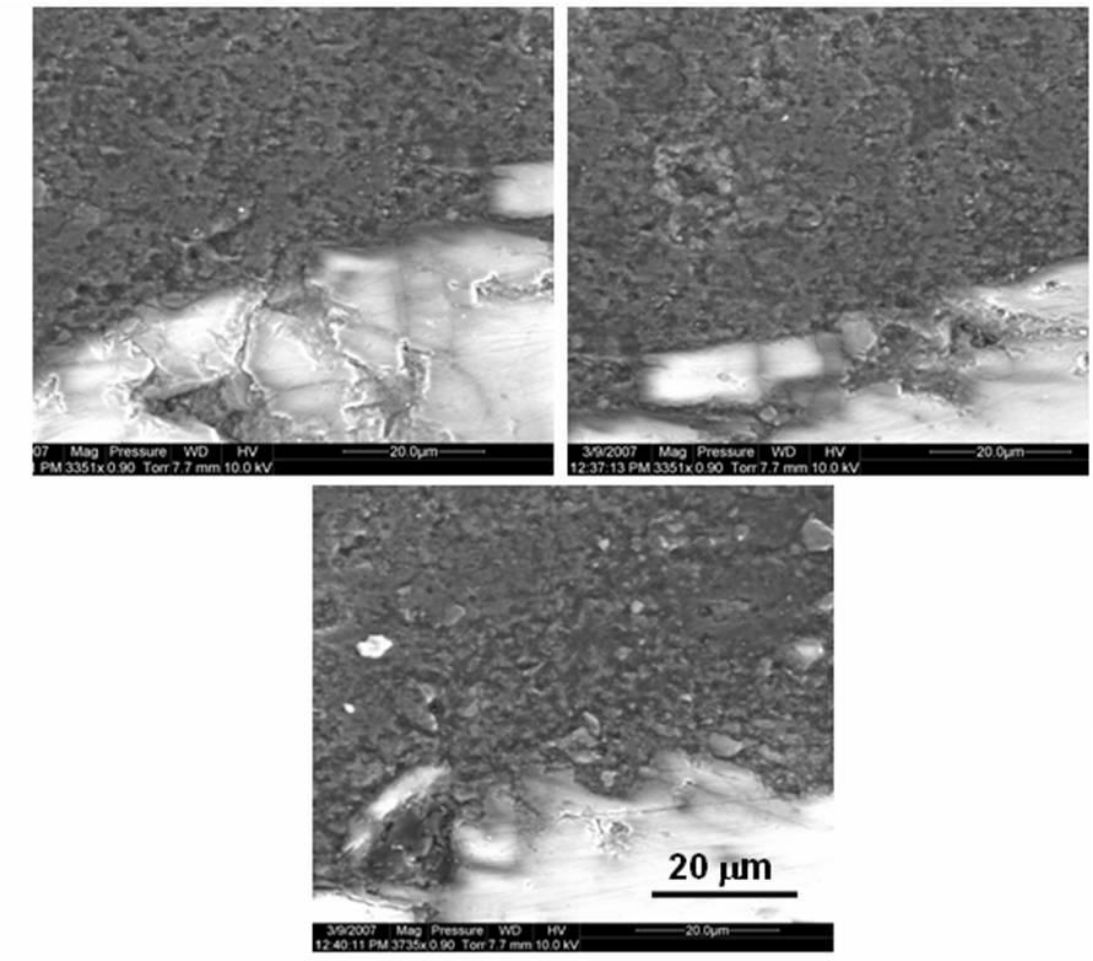

Figure 6.6. SEM Image of the ITZ Showing Proper Bond between Aggregate and Paste

imaging mode of the indenter. Indentation was performed on the selected locations as shown in the top right image of Figure 6.8. The image at the bottom shows modulus in GPa obtained from each indent. No difference in modulus was observed in the area adjacent to gravel. Figure 6.9 shows an AFM image of another area of the same sample captured with the indenter tip. Cement paste close to the gravel shows higher porosity in this case (darker areas in the image represents pore). The indentation modulus obtained in this case was lower than the previous case. Figure 6.10 shows the

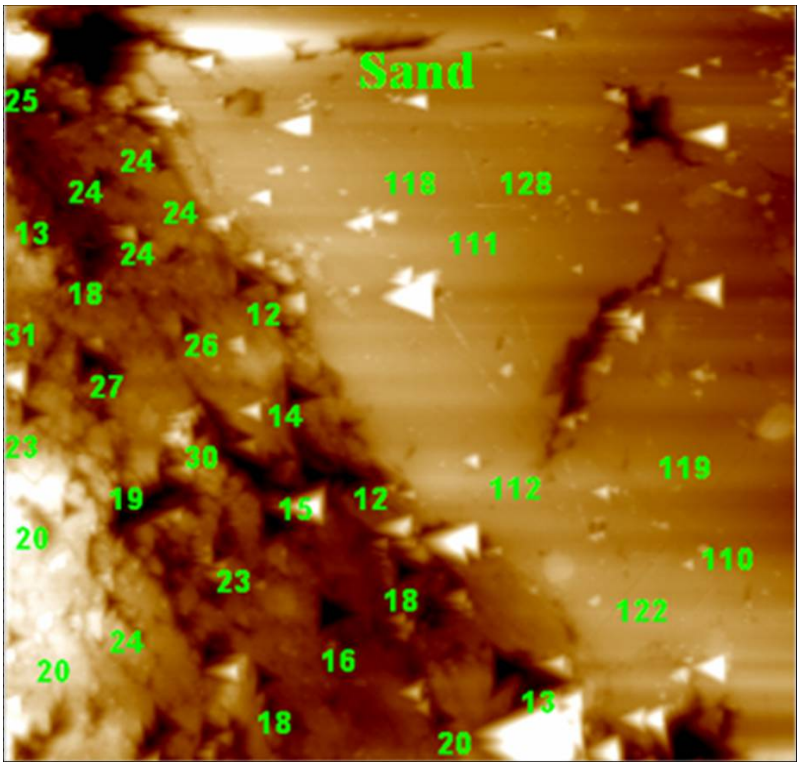

Figure 6.7. 60 μm $\times$ 60 μm Image of Paste with Sand Particle Showing Location of Indents and Elastic Modulus in GPa

modulus obtained from indentation all around one gravel plotted against distance from the gravel. The plot clearly shows that there is no trend of increasing modulus of cement paste with increasing distance from gravel. This is in contrast to what has been reported by Zhu et al. [89], although one has to keep in mind that Zhu et al. used microindentation to study the ITZ between paste and steel bar. The average modulus in the interfacial zone was found to be 85% of that of the paste matrix. This is close to the value assumed by few resent researchers for modeling purposes [76].

6.3.3. ITZ between Limestone and Cement Paste

To eliminate any uncertainty that might be present due to the mixed chemical composition of round gravel, limestone aggregates were used for further study. Figure 6.11 shows AFM image of

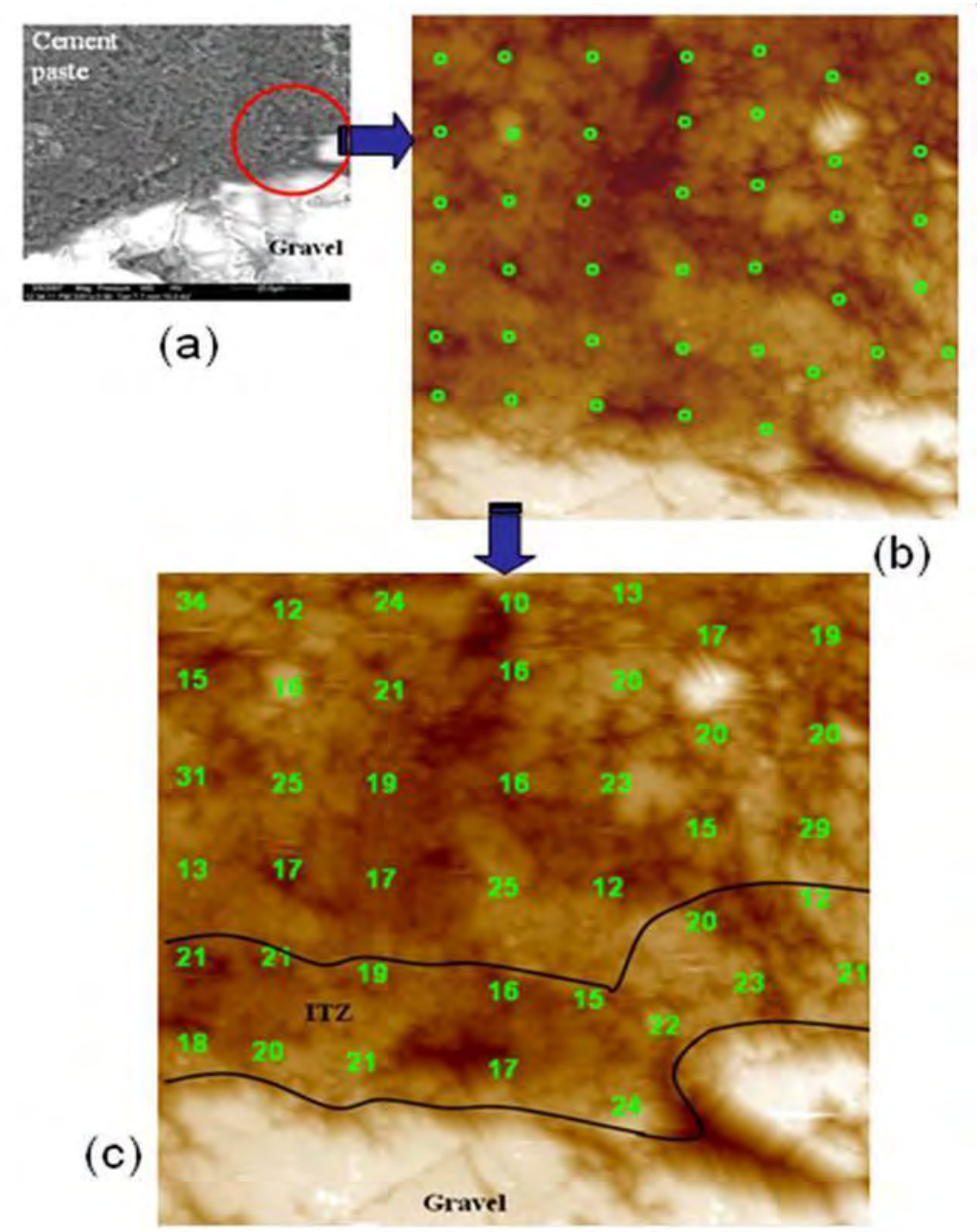

Figure 6.8. 60 μm $\times$ 60 μm Image of a Strong ITZ between Paste and Gravel (a) Scanning Electron Microscopy Image, (b) Atomic Force Microscopy Image Showing Indent Locations, (c) Indentation Modulus in GPa Written on each Indent Locations

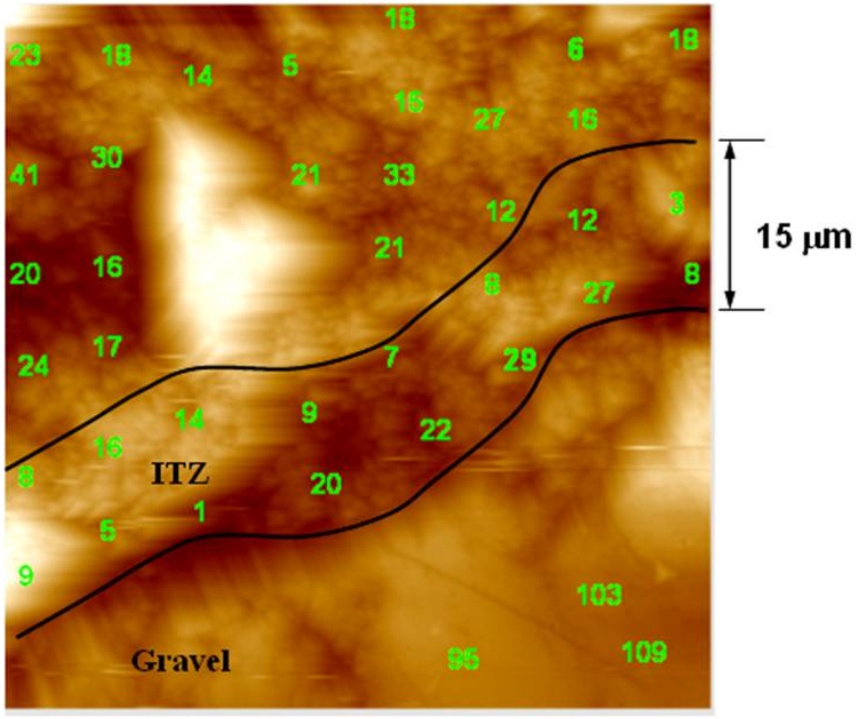

Figure 6.9. 60 μm $\times$ 60 μm Image of a Weak ITZ between Paste and Gravel Showing Elastic Modulus in GPa

the interfacial zone between limestone and cement paste captured with the indenter tip. Indentation was performed on 36 locations in the area and the image shows modulus in GPa obtained from each indent. To determine the variation of modulus with distance from limestone, the experiment was repeated on eight different locations around the same limestone aggregate. Analyzing results of over 200 indents, no trend of increasing modulus with distance from aggregate was found. Figure 6.12 compares the distribution of modulus obtained from nanoindentation on the interfacial zone with modulus of bulk cement paste. In this case, the bin size for the modulus distribution for both the ITZ and the bulk matrix was set at 5 GPa instead of 2.5 MPa. This is because, number of data available in the ITZ was relatively small compared to data obtained from bulk matrix.

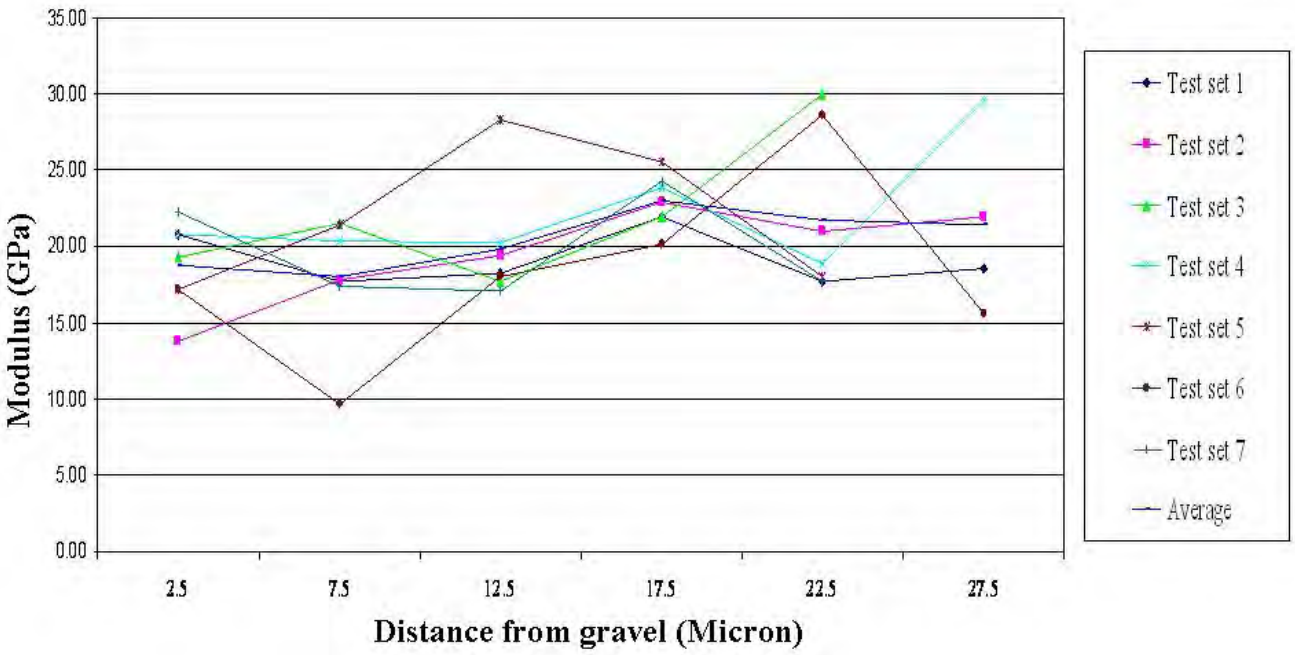

Figure 6.10. Modulus of the ITZ Plotted against Distance from the Aggregate

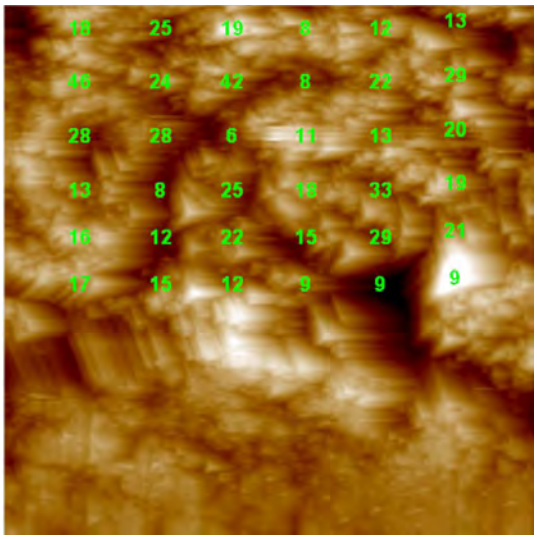

Figure 6.11. Modulus Map of the ITZ between Limestone and Cement Paste

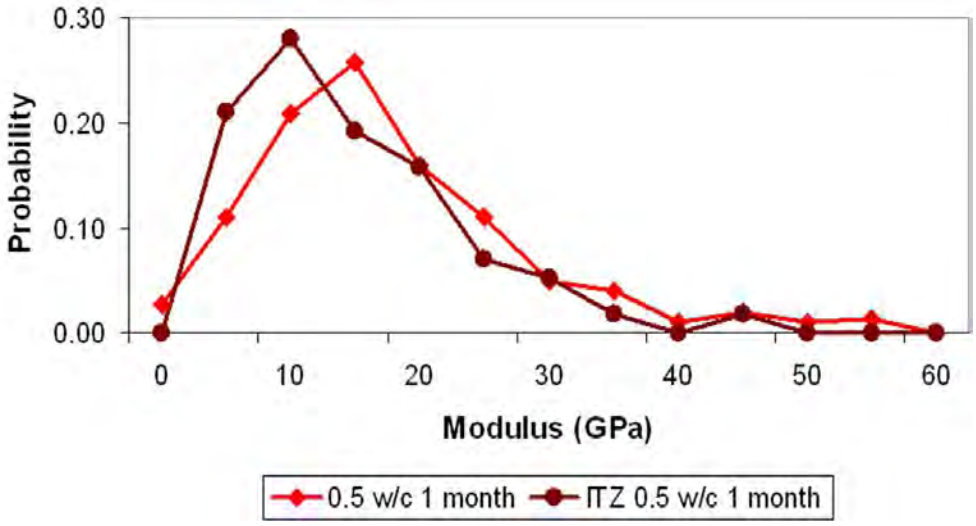

Figure 6.12. Comparison between the Modulus of the ITZ and the Bulk Paste

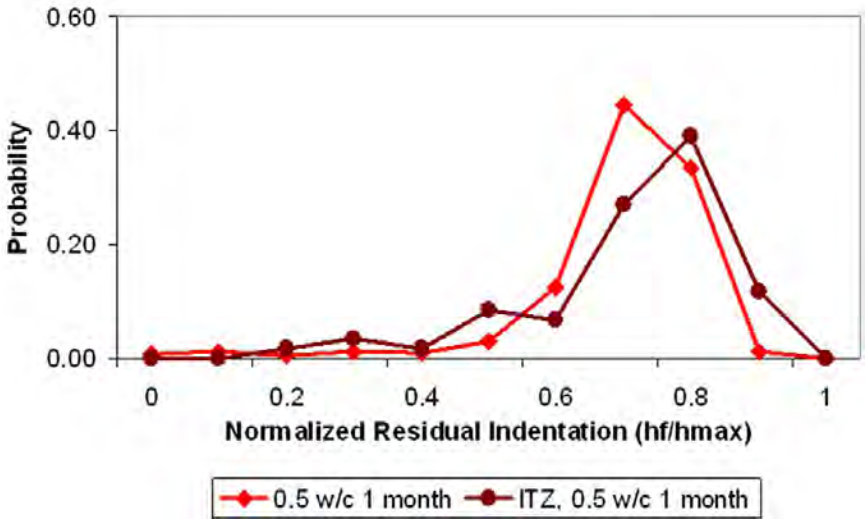

Figure 6.13. Distribution of Normalized Plastic Deformation in the ITZ

Reducing the bin size to 2.5 GPa resulted in too few data in each bin and made it difficult to compare. The figure clearly shows that the modulus distribution of the interfacial zone is shifted to the left which means the average modulus of the ITZ is lower than the average modulus of the

bulk cement paste. Furthermore, the percent of data within the modulus range of 5 to 15 GPa is much higher in the case of the ITZ compared to that of the bulk paste. This implies higher porosity in the interfacial zone. The average indentation modulus of the ITZ was found to be 70% of the average modulus of bulk paste. Figure 6.13 compares the distribution of plastic deformation during indentation normalized over total deformation for the same indentation load. Normalized plastic deformation in interfacial zone was higher than that of bulk matrix since the distribution is shifted to the right. The average plastic deformation in the ITZ was found to be 15% higher than the average plastic deformation of the of bulk cement paste.

6.4. Conclusions

Nanoindentation with imaging was proved to be indispensable to identify the narrow area around aggregate and position the indenter in the same area. Interfacial transition zone was found to be extremely heterogeneous with some areas as strong as the bulk matrix. A higher concentration of large voids and cracks along the interface was observed due to poor bonding. Nanoindentation was performed on relatively intact areas of interface. Results from this study disagree with the notion of increasing the elastic modulus with distance from the interface. However, results show higher porosity in the ITZ and the average modulus of the ITZ is 70% to 85% depending on the aggregate type. 15% higher plastic deformation was observed in the interfacial zone than the average plastic deformation of the bulk cement paste. Still, extreme heterogeneity within the interface and poor bonding between the aggregate and paste remain as the main problem that affects the overall mechanical properties of concrete. It is important to note that the connectivity of the weaker areas such as large voids and cracks along the interface will govern failure. Thus, modeling concrete as

three phase material considering the ITZ as a weak zone around aggregate with average property some percentage less than the paste matrix may not be sufficient to predict overall strength.

Chapter 7 Nanomechanical Properties of Concrete with Silica Fume and Nanosilica

7.1. Introduction

It is well recognized that the use of mineral admixtures such as silica fume and fly ash enhances strength and durability of concrete. Many researchers studied changes in macroscopic properties. In recent years, Poon et al. reported effects of metakaolin and silica fume on compressive strength, chloride diffusivity and pore structute [66]. Olson and Jennings used water adsorption to measure C-S-H content in blended cement [60]. Richardson reported the effect of adding silica fume on the structure of C-S-H [70]. This chapter summarizes a detailed study of how addition of silica fume and nanosilica affect nanoscale local mechanical properties of paste. Furthermore, from macroscopic tests, silica fume was found to improve properties of the interfacial transition zone in concrete [12, 62, 63]. Research presented in this chapter shows how the addition of silica fume has

a greater effect on the mechanical properties of the interfacial transition zone than on bulk paste in concrete.

7.2. Paste with Silica Fume

Silica fume is a byproduct of silicon metal or ferrosilicon alloy manufacture which primarily consists of amorphous (non-crystalline) silicon dioxide (SiO_2). The individual particles of silica fume are extremely small, approximately 1/100th the size of an average cement particle. Because of its chemical and physical properties, it is a very reactive pozzolan. Concrete containing silica fume can have very high strength and can be very durable.

7.2.1. Experimental Detail

Paste samples were made with densified silica fume powder. 15% silica fume by wt. was used to replace Type I Portland cement. The water to binder ratio was kept at 0.5. Figure 7.1 shows the particle size distribution of the densified silica fume powder. Silica fume is supposed to have nanometer size particles that improves particle packing in concrete and therefore reduces porosity. However, Figure 7.1 shows high volume of larger particles with average particle size of 143 μm. This is due to the formation of agglomerates. As reported by Diamond, [27], it is difficult to break these agglomerates into smaller particles. Also dispersing silica fume is a serious problem. The Silica Fume Association suggests the following mixing procedure to ensure proper dispersion of densified powder in concrete:

- Place 75% of water in mixer. Follow ASTM C192 for addition of admixtures.
- Add coarse aggregate.

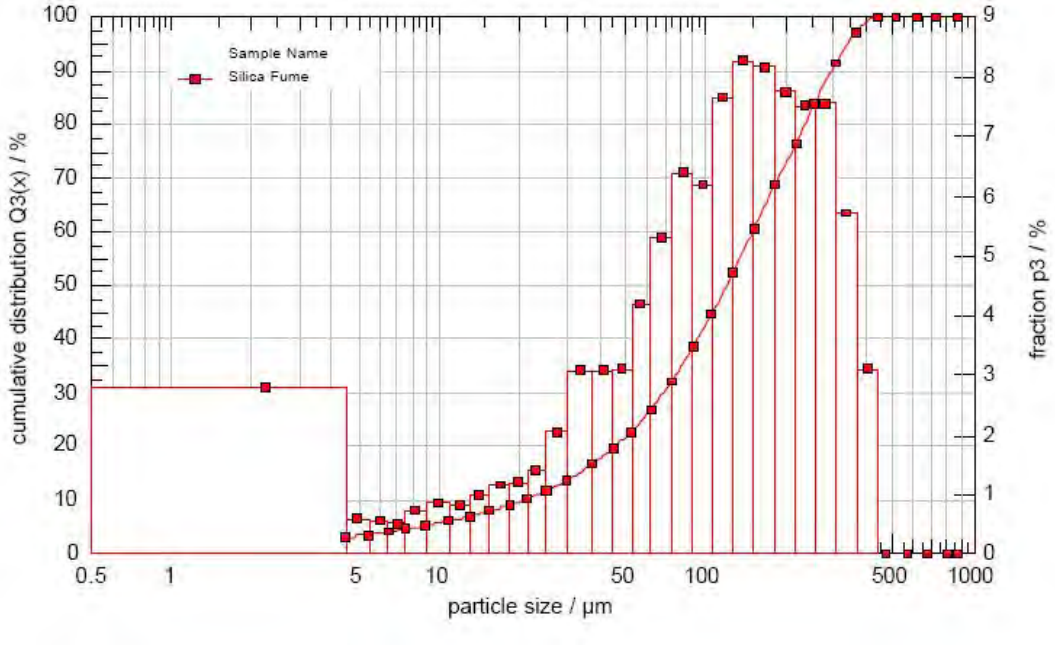

Figure 7.1. Particle Size Distribution of Densified Silica Fume Powder

- Add silica fume slowly into the revolving mixer.
- Mix $1\frac{1}{2}$ minutes.
- Add cement (and fly ash or slag cement, if being used) slowly into the revolving mixer.
- Mix $1\frac{1}{2}$ minutes.
- Add fine aggregate.
- Wash-in all ingredients using the remaining 25% of water.
- Mix 5 minutes (time may be extended by user based on equipment and performance results).
- Rest 3 minutes.
- Mix 5 minutes.

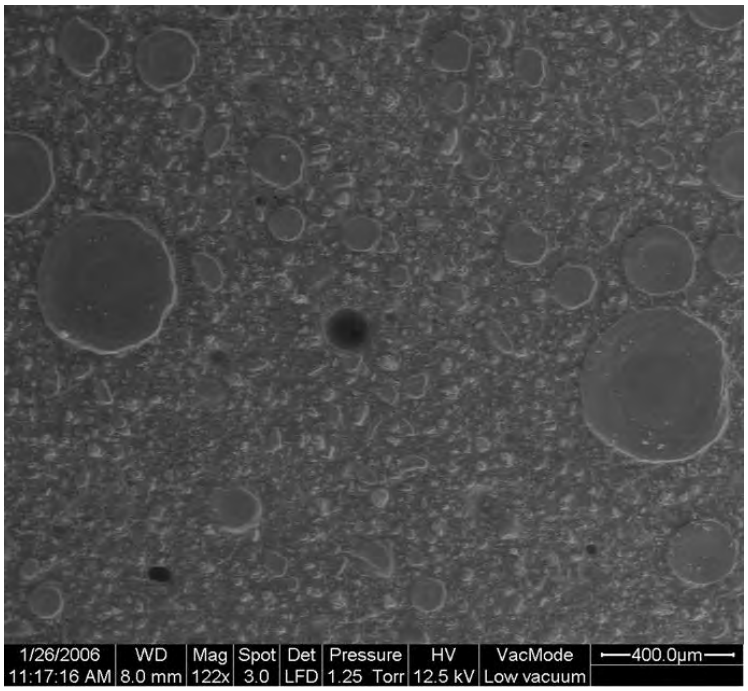

Figure 7.2. Scanning Electron Microscopy Image of Paste with 15% Densified Silica Fume Powder

To make paste samples for this study, the above mixing procedure was modified based on the specification of ASTM standard C305. Samples were cured under water for one month at 25° C temperature. After curing, samples were polished following the procedure discussed in Chapter 4. Figure 7.2 shows an SEM image of a polished sample where silica fume particles, as large as couple of 100 μm, are clearly visible. It was decided to use Force 1000D silica slurry from W. R. Grace for the rest of this study. Silica slurry is a predispersed mix of silica fume powder in water with 50% total solid by weight. Figure 7.3 shows an SEM image of a polished sample with slurry. Similar to the previous case, 15% silica fume by weight of cement was used to replace cement. The percentage of water present in the slurry was considered to maintain effective water to binder ratio as 0.5. From Figure 7.3, it is evident that the problem with dispersing silica fume was solved

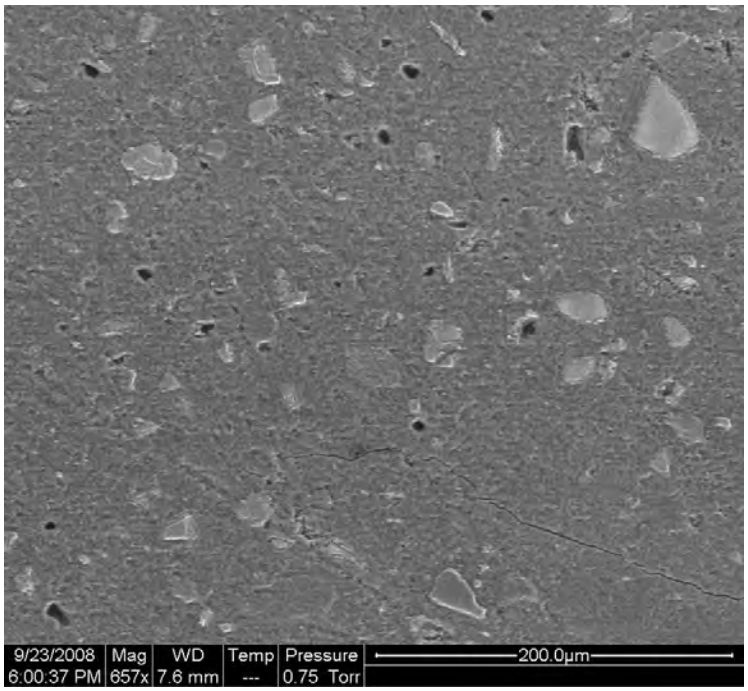

Figure 7.3. Scanning Electron Microscopy Image of Paste with 15% Silica Slurry

by using the slurry form. Furthermore, Figure 7.3 shows less porosity on the surface compared to SEM image of paste without silica fume in Figure 5.20.

7.2.2. Nanomechanical Properties of Paste with Silica Fume

Grid indentation was performed following the method described in Section 5.2.5. A Total of 432 indents were made in 3 different randomly chosen areas to minimize site specific properties in the indentation data set. In each area, 144 indents were made in an 12×12 array. Spacing between each indent was 10 μm. Figure 7.4 and Figure 7.5 shows the probability distribution plot of the modulus and hardness respectively. Since C-S-H and other phases present in a cement sample are expected to have a unique set of modulus and hardness, the distribution of modulus and hardness show a similar trend. Most of the modulus data was found within a range of 10 GPa to 30 GPa

and hardness in between 0.25 GPa to 1 GPa. These values correspond to the main phase in cement paste, C-S-H. Furthermore, both the modulus and hardness plot show a peak corresponding to calcium hydroxide at a modulus around 32 GPa and hardness around 1.5 GPa. The probability plot shown in Figure 7.4 was analyzed to determine the volume fraction of C-S-H. Table 7.1 shows change in volume fraction of different phases in a sample with 15% cement replaced by silica fume. Although Figure 7.3 shows less porosity on the surface compared to the SEM image of paste without silica fume (see Figure 5.20), the volume fraction of the porous phase was found to be comparable in both the samples with and without silica fume. However, nanoindentation results showed evidence of pozzolanic reaction in the sample with silica fume. Table 7.1 clearly shows that the addition of silica fume increased the volume fraction of high stiffness C-S-H and decreased volume fraction of calcium hydroxide.

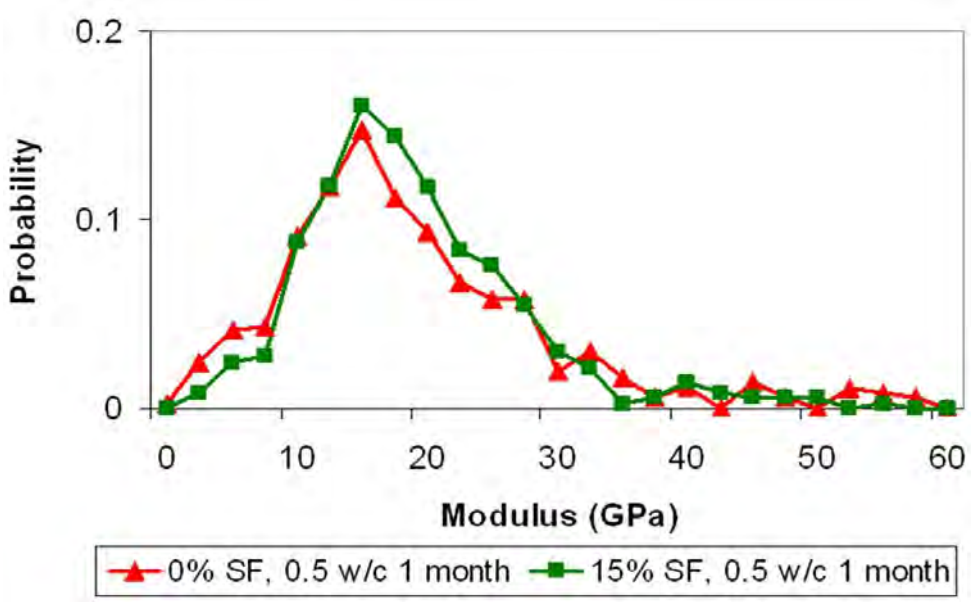

Figure 7.4. Probability Distribution of Modulus for Paste with 15% Silica Slurry

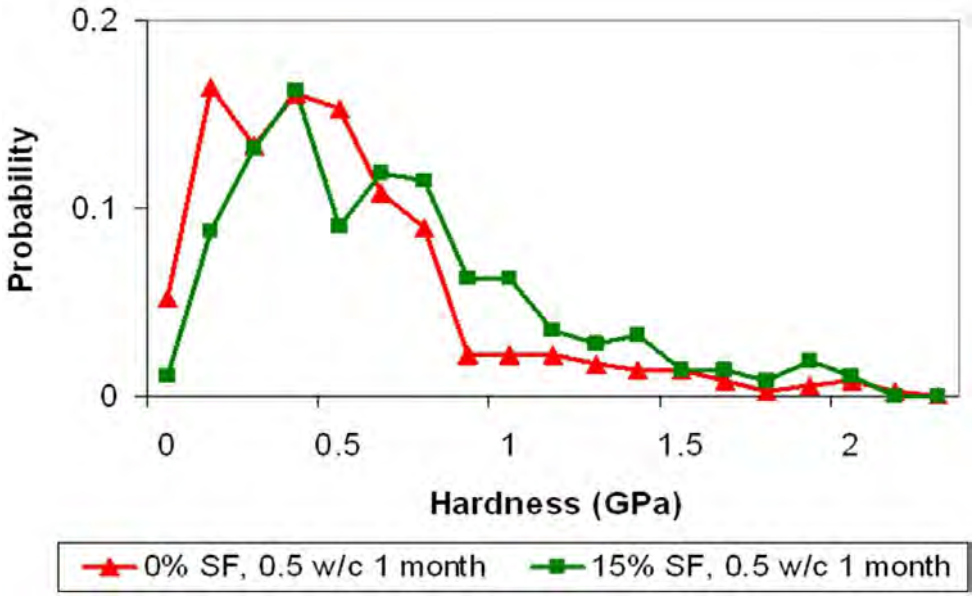

Figure 7.5. Probability Distribution of Hardness for Paste with 15% Silica Slurry

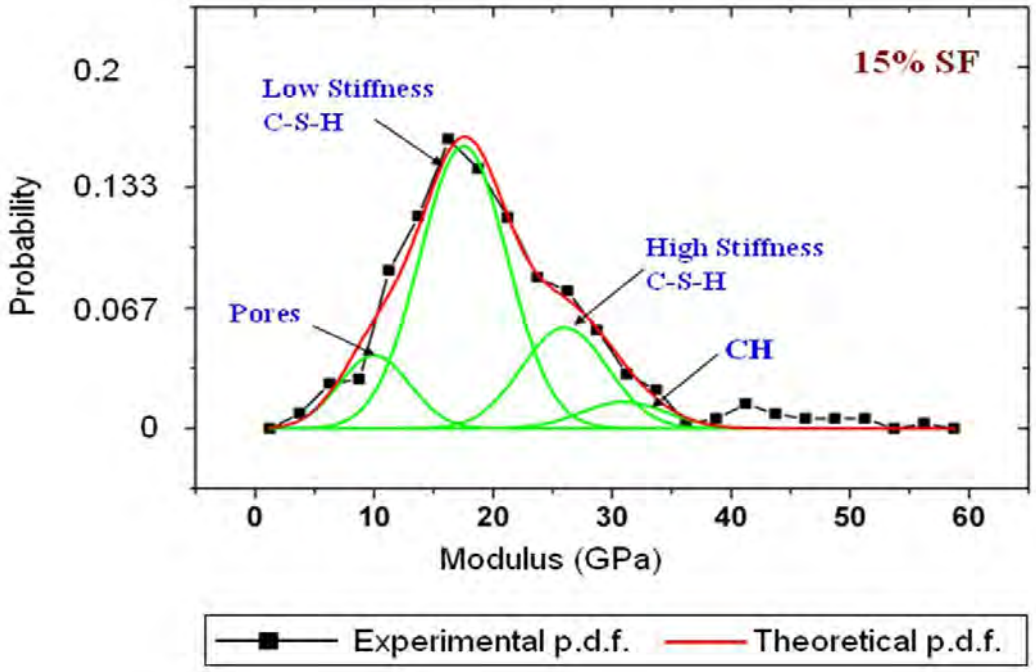

Figure 7.6. Indentation Modulus of Paste with 15% Silica Slurry

		0% SF	15% SF
Porous Phase	Elastic Modulus	9.4±3.4	10±4.2
	Volume Fraction (%)	10	12
Low Stiffness C-S-H	Elastic Modulus	16.5±4.7	17.5±3.7
	Volume Fraction (%)	63	60
High Stiffness C-S-H	Elastic Modulus	27.1±3.5	26±3.4
	Volume Fraction (%)	19	25
Calcium Hydroxide	Elastic Modulus	36.9±3.5	31.8±3.4
	Volume Fraction (%)	8	3

Table 7.1. Change in Volume Fraction of Different Phases with Addition of Silica Fume

7.3. Paste with Nanosilica

7.3.1. Experimental Detail

This part of the work was done in collaboration with the Centre for Nanomaterials Applications in Construction (NANOC) of LABEIN-Tecnalia, at Derio (Spain). In a parallel study done by the LABEIN group, ^{29}Si MAS-NMR spectra of cement pastes with nanosilica proved that nanoparticles increase the average chain length of C-S-H gel [32]. Therefore, it was expected that nanosilica increased either the amount or the strength of high density C-S-H in paste. Two different samples were studied in this occasion using commercially available nanosilica (Table 7.2): one with 6 wt% of nanosilica (L100-6g) and another one with 18 wt% of nanosilica. Samples were cast and cured at the Centre for Nanomaterials Applications in Construction (NANOC) of LABEIN-Tecnalia, at Derio (Spain). Both specimen preparation and nanoindentation tests were performed at the Advanced

Cement Based Materials Center (ACBM), at the Northwestern University at Evanston (USA). The sample were polished following the technique described in Section 4.3.1 and a significant number of indents (140-280) were made in each of the samples. As an example, Figure 7.7 shows a SEM image of polished sample with 18% nanosilica.

Commercial Name	Particle Size (nm)	SiO_2 Content (wt%)	Stabilizer	pH	Physical Description
Levasil 100/45	30	45	NaO	10	Colloid

Table 7.2. Detail of L100 Nanosilica [32]

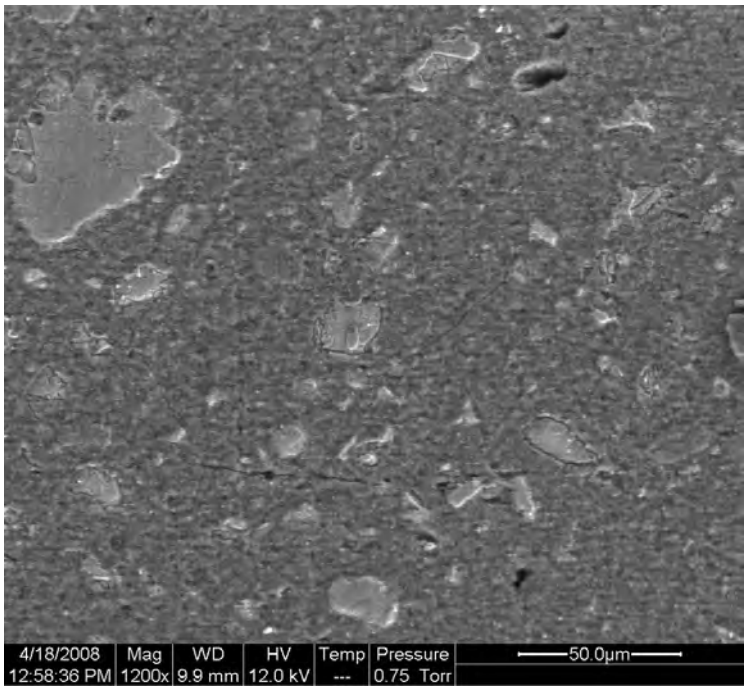

Figure 7.7. Scanning Electron Microscopy Image of Paste with 18% Nanosilica

7.3.2. Nanomechanical Properties of Paste with Nanosilica

Indentation data was analyzed in terms of their frequency distributions. The bin size for the distribution was set at 2.5 GPa and 125 MPa for the elastic modulus and hardness respectively.

Frequency distribution plots for modulus and hardness data show occurrence of major peaks in the

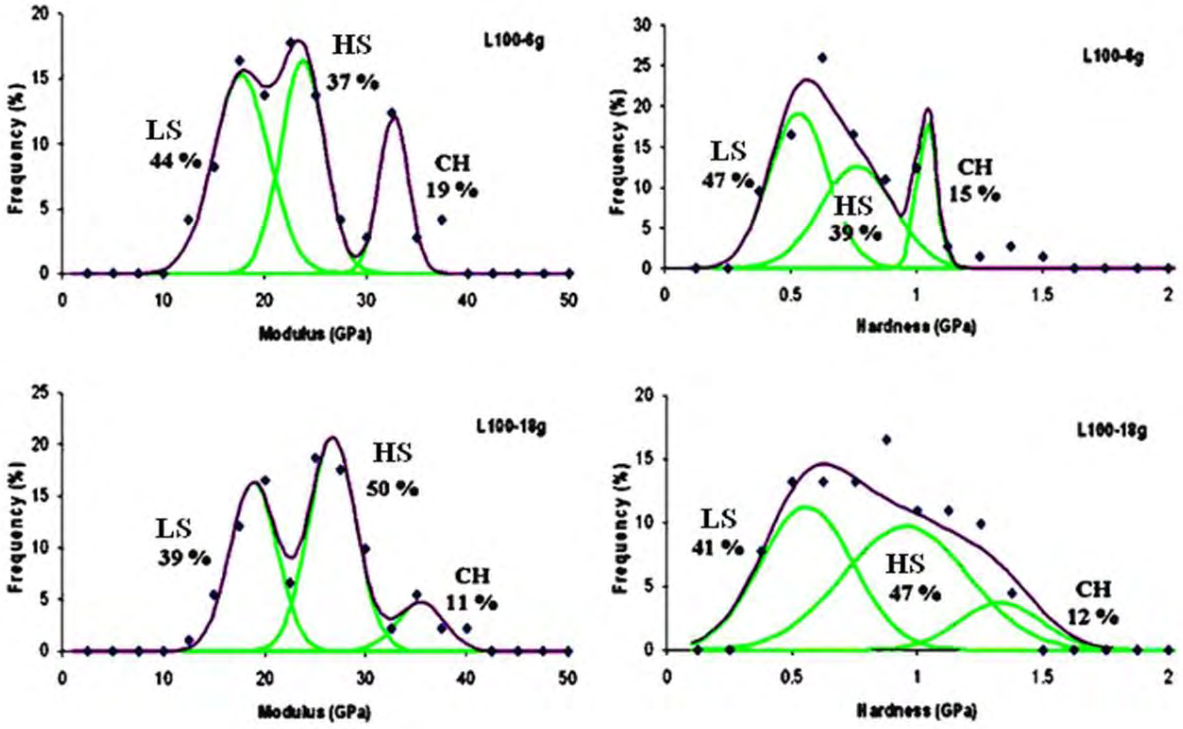

Figure 7.8. Modulus and Hardness Distribution of Paste with 6% and 18% Nanosilica

range 10-30 GPa and 0.25-1 GPa for modulus and hardness respectively, as shown in Figure 7.8. An additional peak was found for calcium hydroxide in both modulus and hardness distributions. The values of hardness and modulus of the sample containing the highest amount of nanosilica (L100-18g), were in good agreement with the ones found in the literature. Figure 7.8 shows that nanosilica significantly increased the amount of high stiffness C-S-H gel. Volume fraction of high stiffness C-S-H were 37% and 50% for samples with 6% and 18% nanosilica respectively. The calculated amount of portlandite clearly diminished with increasing amount of nanosilica.

7.4. Local Mechanical Properties of the ITZ with Other Binder: Literature Review

As reported in Chapter 6, the interfacial transition zone has a significant role on the overall properties of concrete. Simeonov et al. [73] reported the influence of ITZ on the overall elastic properties of mortar and concrete. In normal concrete, it is considered to be the weakest link in the mechanical system [34, 72]. However, many researchers reported that the addition of supplementary materials enhances properties at the interface. This was observed in many macroscopic tests particularly for high strength concrete. However, complexity of the structure and constraints of existing measurement techniques still pose the main challenge to determine changes in local mechanical properties due to the addition of the supplementary materials. Asbridge et al. reported an increase in Knoop microhardness measured in the ITZ in model mortar with 10 percent metakaolin [3]. The ITZ was still reported to be weaker than the bulk matrix at w/c of 0.4 and 0.5. However, at w/c 0.6, they reported higher Knoop microhardness at the ITZ and at the bulk matrix. Jiang studied properties of the ITZ in high volume fly ash concrete (HVFA). From X-ray diffraction, scanning electron microscopy imaging, and bond strength test, he reported that there is no obvious transition zone between aggregate and HVFA paste [45]. Considering the fracture properties of concrete, Prokopski et al. reported that the ITZ in silica fume concrete is stronger than that in Portland cement concrete [67]. Paulon, Molin and Monteiro reported that the results of macroscopic tests, such as compressive, tensile and shear strength test indicated that the addition of silica fume not only increases the strength of the ITZ, but also has a greater influence on the strength of the ITZ than on the strength of the paste matrix. The following sections present a detailed nanoindentation study to arrive at a definite answer to these issues.

7.4.1. ITZ between Limestone and Paste with Silica Fume: Experimental Detail

To compare properties of the ITZ with and without silica fume, values of different factors such as water to cement ratio, age of sample, aggregate type and size were kept the same as those in Section 6.2. In this case, the water to binder ratio was fixed at 0.5 and the age of the sample was fixed at 1 month. Limestone aggregates with an approximate size of 5 mm were used to make model concrete samples. The size of all the samples were 1 inch $\times$ 1 inch $\times$ 0.5 inch. Force 1000D silica slurry from W. R. Grace was used to replace 15% of cement (by weight) with silica fume. Samples were cured under water at 25°C. For nanoindentation, samples were prepared following the method described in Chapter 4. Figure 7.9 shows a SEM image of the ITZ between limestone and paste with silica slurry. In contrast to the interfacial transition zone in model concrete samples without silica fume, no obvious interfacial zone was found in this case. Interface areas were free of large voids and cracks. From SEM imaging, no difference in porosity was found in these areas. This demonstrates improved bonding between aggregates and cement paste with silica fume.

7.4.2. Nanomechanical Properties of the ITZ between Limestone and Paste with Silica Fume

Though the SEM image shown in Figure 7.9 did not show a concentration of large pores at the interface, micron size pores at the interface were visible in high resolution AFM images. Figure 7.10 is one such AFM image of the interfacial zone between limestone and paste with silica fume, captured with the indenter tip. Figure 7.11 shows the modulus and hardness map created from 72 indents over an area of 40 μm $\times$ 88 μm adjacent to the limestone. The horizontal axis represents the distance from the interface. Deep blue areas near the interface represents weaker areas. To determine the variation of modulus with distance from limestone, experiment was repeated

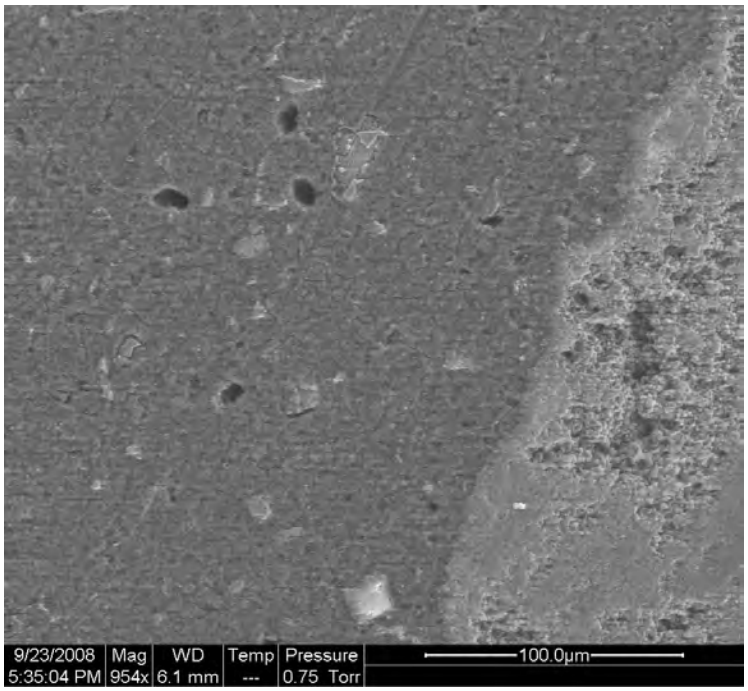

Figure 7.9. SEM Image of the ITZ between Limestone and Paste with Silica Fume

on eight different locations around the same limestone aggregate. Analyzing results of over 200 indents, increasing trend of modulus was found within 20 μm of the interface (Figure 7.12).

Figure 7.13 compares distribution of modulus obtained from nanoindentation on interfacial zone with modulus of bulk paste. This figure shows little higher volume fraction of porous phase, though the average modulus at the interface was the same as the average modulus of the bulk paste. Figure 7.14 compares probability distribution of modulus of interfacial transition zone with and without addition of silica fume. It is clear that addition of silica fume increases stiffness of the interfacial zone. Percentage of data within the modulus range of 5 to 15 GPa is much higher in case of the ITZ without silica fume. This implies reduction in porosity with addition of silica fume.

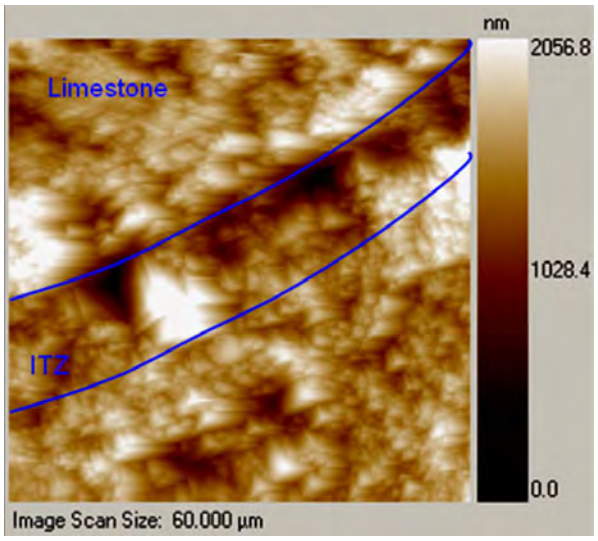

Figure 7.10. 60 μm $\times$ 60 μm Image of the ITZ between Limestone and Cement Paste

Figure 7.15 compares distribution of plastic deformation during indentation normalized over total deformation for samples with silica fume. Normalized plastic deformation in interfacial zone was higher than that of bulk matrix since the distribution is shifted towards right. In spite of the reduction in porosity and similar average modulus, plastic deformation in the ITZ was found to be 15% higher than the average plastic deformation of the of bulk paste. Furthermore, when plastic deformation in the ITZ for samples with and without silica fume was compared, they were found to be similar.

7.5. Conclusions

Nanoindentation was performed on paste with 15% of silica fume. The indentation modulus and hardness corresponding to the main phase in paste, C-S-H, were found to be within a range between 10 GPa to 30 GPa and 0.25 GPa to 1 GPa respectively. Replacing 15% cement by silica

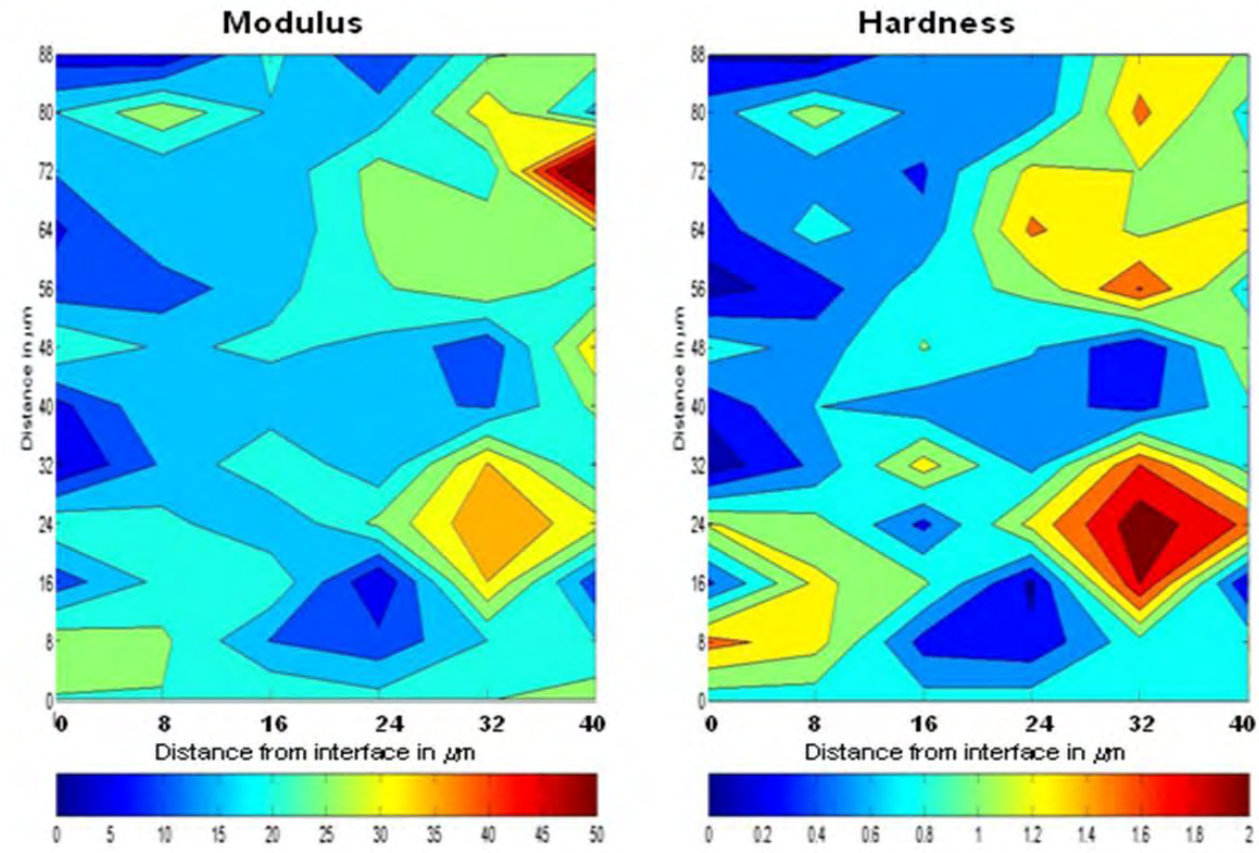

Figure 7.11. Modulus and Hardness Map of the ITZ between Limestone and Cement Paste

fume did not change phase properties of the four phases. A reduction in volume fraction of calcium hydroxide in the sample with silica fume provides evidence of pozzolanic reaction. Little increase in volume fraction of high stiffness C-S-H was observed. This increase is comparable with the decrease in volume fraction of calcium hydroxide. This observation suggested that either prozzolanic reaction forms more high stiffness C-S-H or improved packing in a sample with silica fume facilitates formation of high stiffness C-S-H and thus increases the ratio of high stiffness to low stiffness C-S-H by 10%. This observation is particularly interesting since it compares well

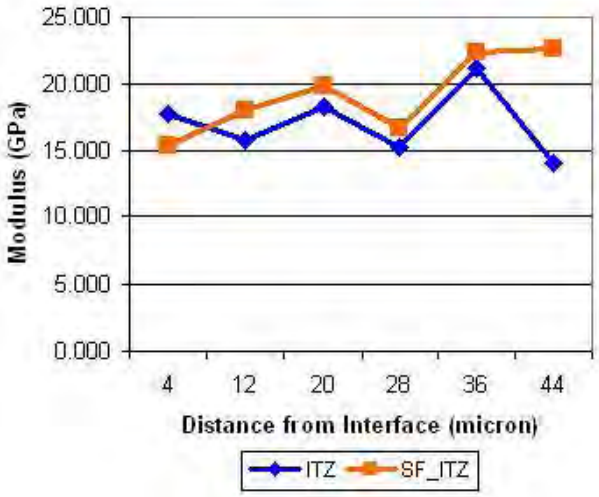

Figure 7.12. Modulus of the ITZ vs. Distance from Interface

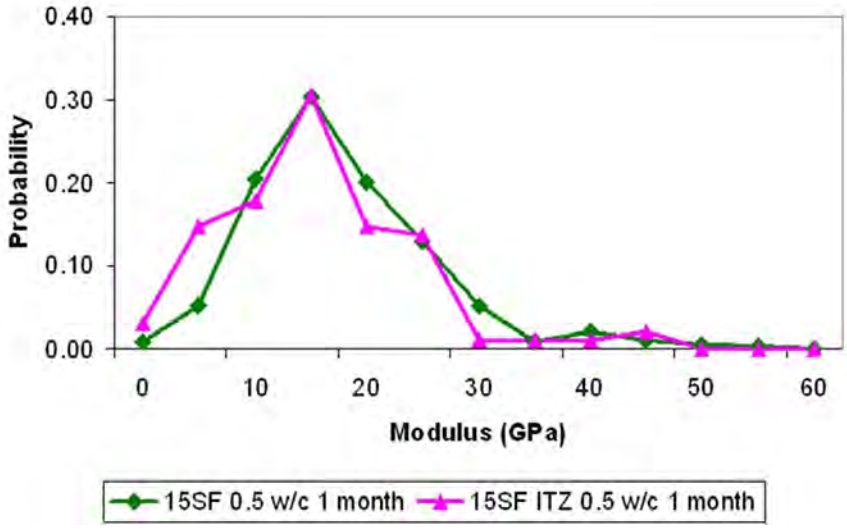

Figure 7.13. Distribution of Modulus of the ITZ and the Bulk Paste with 15% Silica Fume

with literature reporting higher volume fraction of C-S-H with longer chain length in blended cement paste with silica fume [70]. However, further study on change in morphology of C-S-H due to addition of silica fume is necessary.

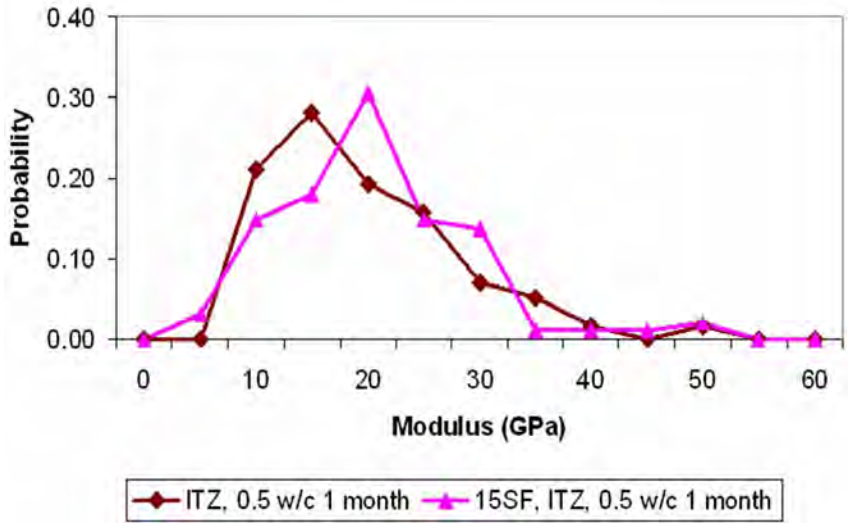

Figure 7.14. Comparison of the distribution of Modulus of the ITZ for Samples with and without Silica Fume

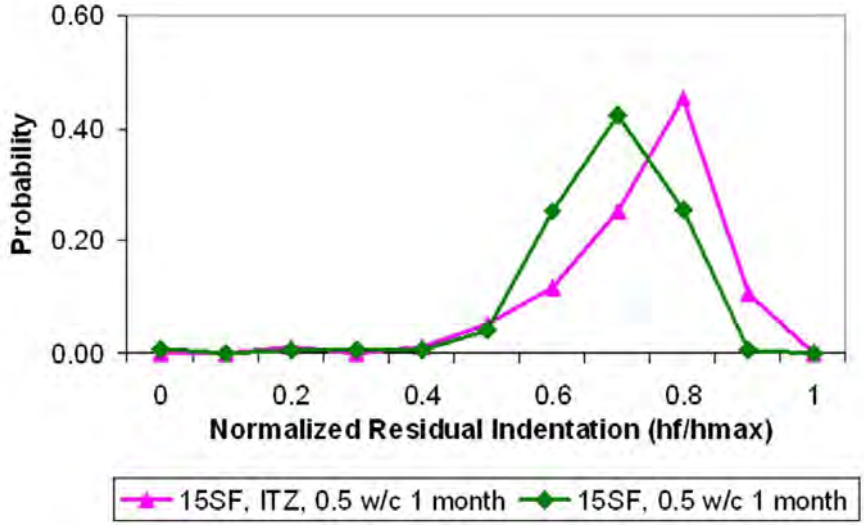

Figure 7.15. Distribution of Normalized Plastic Deformation at the ITZ

Nanoindentation was performed on cement paste with 18% nanosilica. In a study parallel to this research, ^{29}Si MAS-NMR spectra of the cement pastes with nanosilica proved that nanosilica increases the average chain length of C-S-H gel. Therefore, it was expected that nanosilica either

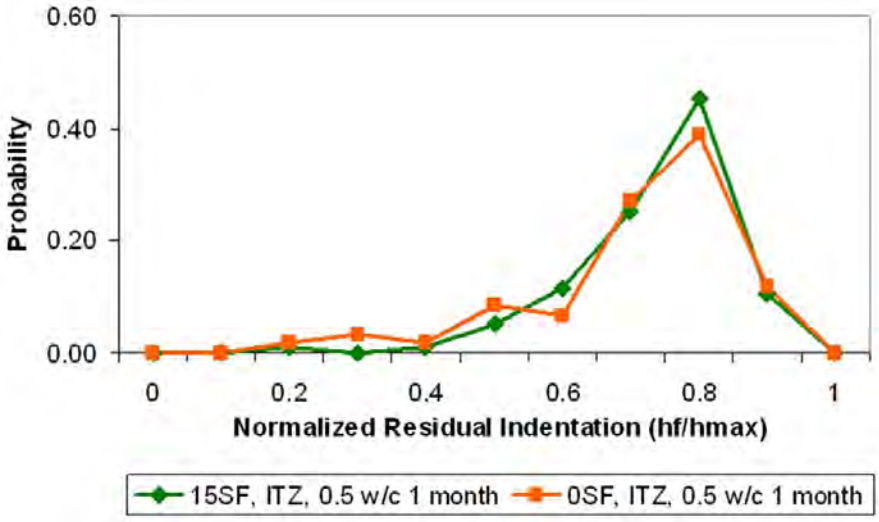

Figure 7.16. Comparison of Plastic Deformation at the ITZ with and without Addition of Silica Fume

increases the amount of high stiffness C-S-H or its strength. Nanoindentation study proved that elastic modulus of either of the two C-S-H phases do not change with addition of nanosilica. However, as high as 50% increases in the volume fraction of high stiffness C-S-H gel was observed in sample with 18% nanosilica.

Furthermore, nanoindentation results showed that the addition of silica fume had greater effects on the nanomechanical properties of the interfacial transition zone than on bulk paste. Comparing the modulus of interfacial transition zone with and without addition of silica fume, it was clear that the addition of silica fume increased stiffness of the interfacial zone and reduced porosity. It is also important to note that the addition of silica fume eliminated large cracks and voids at the interface and made the interfacial zone more homogeneous. In the sample with 15% silica fume, the interface was found to have the same average modulus as that of the bulk paste. In spite of the reduction in porosity and similar average modulus, the plastic deformation in the ITZ was found to

be 15% higher than the average plastic deformation of the bulk paste. Furthermore, when plastic deformation in the ITZ for samples with and without silica fume was compared, they were found to be similar.

Chapter 8 Indentation on Rough Surfaces

8.1. Introduction

Chapter 4 discussed the importance of surface preparation for applying nanoindentation to characterize cementitious materials. It also presented the surface preparation technique developed in this research. Based on existing literature, it was shown that the proposed surface preparation method was successful to reduce roughness to a tolerable level. Hence, analysis of nanoindentation data, described in Chapter 5 to 7 was performed based on classical contact mechanics theory for indentation on flat surface. Indentation was considered as contact between an indenter and an infinite half-space where initial surface is perfectly flat. In consequence, contact between the indenter and the sample was considered continuous within the nominal contact area and absent outside it. In this part of this thesis, surface roughness criteria is revisited. There are a number of approaches to solve the contact problem on real rough surface [8, 40, 65]. In this chapter, few of

these approaches are summarized and how this was applied to address surface roughness criterion of polished cementitious samples for nanoindentation is presented.

8.2. Profilometric Theory of Rough Contact

8.2.1. Contact of Nominally Flat Rough Surfaces

In frictionless contact of elastic solids, contact stresses depend only on the relative profile of the two surfaces. In other word, stresses depend on the gap between the two surfaces before loading. This section describes the profilometric theory of contact between a rigid flat surface and a nominally flat deformable rough surface. As described in Johnson [40], following analysis was developed by Greenwood and Williamson [33]. Figure 8.1 shows the profile of a surface where mean surface level is taken as a datum. At a separation distance or gap d between the two solids, summits of surface asperities with height z_s greater than d will be in contact. Now using the probability distribution of summit heights, $\phi(z_s)$, with a mean $\bar{z_s}$, we can compute the total number of asperities in contact as

$$n = N \int_d^\infty \phi(z_s) dz_s \tag{8.1}$$

where N is the total number of summits within the nominal contact area A_0. For simplicity, summits of each asperities are assumed to be spherical with constant curvature k_s. Deformation of each summit that makes contact with the flat punch over a circular area of radius a can be written as $\delta = z_s - d$. Therefore, for the i^{th} summit in contact, we can express contact area and force in

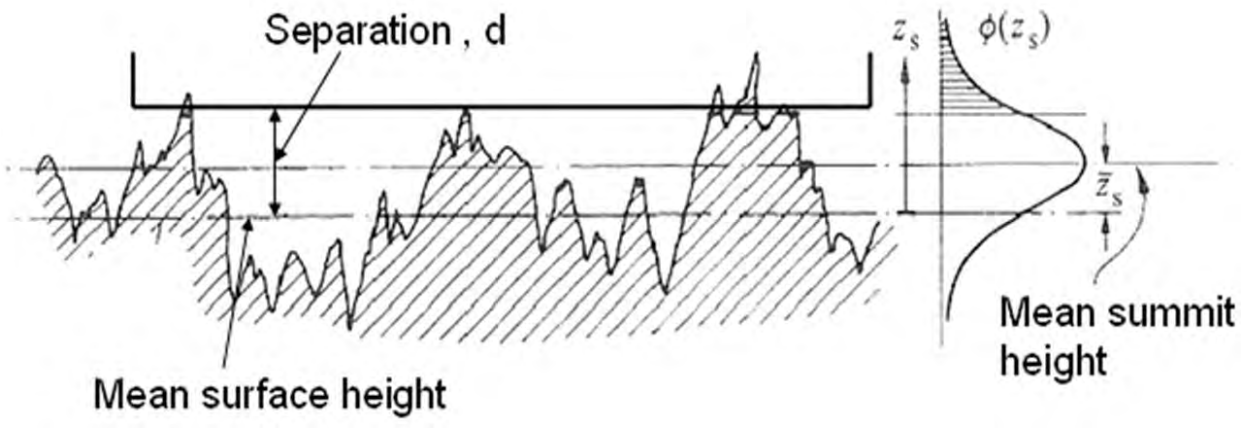

Figure 8.1. Contact of a Randomly Rough Surface with a Smooth Flat Surface [40]

terms of deformation δ as

$$A_i = \pi a_i^2 = f(\delta_i) \tag{8.2}$$

and

$$P_i = g(\delta_i) \tag{8.3}$$

where functions $f(\delta)$ and $g(\delta)$ depend on material properties. In case of elastic deformation, using Hertz solution

$$f(\delta) = \frac{\pi \delta}{k_s} \tag{8.4}$$

and

$$g(\delta) = \frac{4}{3} E^* k_s^{\frac{-1}{2}} \delta^{\frac{3}{2}} \tag{8.5}$$

For perfectly plastic deformation of an asperity, ignoring piling-up or sink-in

$$f(\delta) = \frac{2\pi\delta}{k_s} \tag{8.6}$$

and

$$g(\delta) = \bar{p}A = 6\pi Y \frac{\delta}{k_s} \tag{8.7}$$

where Y is the yield strength of the material. Now the total contact area, A and the total contact force Pcan be calculated by adding Eq. 8.2 and Eq. 8.3 for all asperities in contact. Thus,

$$A = N \int_d^\infty f(z_s - d)\phi(z_s) dz_s \tag{8.8}$$

and

$$\bar{p}A_0 = P = N \int_d^\infty g(z_s - d)\phi(z_s) dz_s \tag{8.9}$$

One of the limitation of this theory is that, it uses the stress-displacement response of isolated microcontacts. Surface displacements of non-contact points are neglected in this theory and it does not take into account interaction between microcontacts.

8.2.2. Modification of Profilometric Theory for Rigid Cone

This section presents how the previous derivation can be modified for a rigid conical indenter. Figure 8.2 shows the profile of a rough surface. As before, mean surface level is taken as the datum. Since a cone indenter introduces a sharp change in the slope of the indenter profile, we need to rewrite the gap function. It is assumed that the first contact occurs at a summit height equal to the 90^{th} percentile of the distribution of z_s and is denoted as z_{90}. The first contact point is considered as the origin and indentation depth is measured along z axis with +ve direction pointing downward. For an approach distance δ, the gap between the tip of the cone and the mean surface level is denoted by $h(0)$ and can be written as

$$h(0) = z_{90} - \delta \tag{8.10}$$

Now, if the cone angle of the indenter is α, gap function at a distance r from the origin is given by

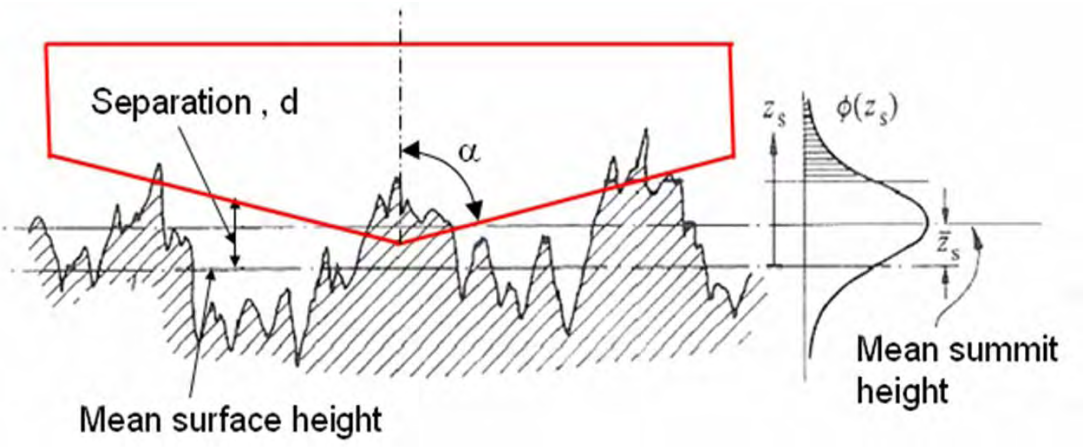

Figure 8.2. Contact of a Randomly Rough Surface with a Rigid Cone

$$h(r) = z_{90} - \delta + \frac{r}{\tan\alpha} \tag{8.11}$$

Let us assume that the number of asperities per unit area of the surface is N_u. As shown in Figure 8.3, consider a circular ring at a distance r from the origin with a width dr. The area of the ring is $2\pi r dr$ and the number of asperities within this annular ring is $2\pi r dr N_u$. Now, any asperity with summit height greater than the gap function at a distance r from the origin, would be in contact with the indenter. Therefore, number of asperities in contact

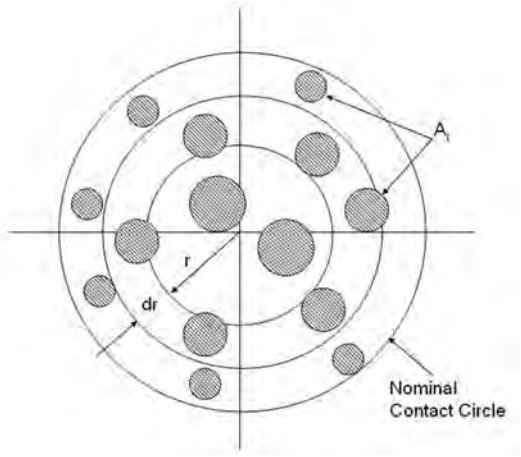

Figure 8.3. Plan View of Contact between a Randomly Rough Surface with a Rigid Cone

$$dn = 2\pi r dr N_u \int_{h(r)}^{\infty} \phi(z_s) dz_s = 2\pi r dr N_u \int_{z_{90}-\delta+\frac{r}{\tan\alpha}}^{\infty} \phi(z_s) dz_s \tag{8.12}$$

Deformation of the i^{th} asperity with summit height z_s would be

$$\delta_i = z_s - h(r) = z_s - \left(z_{90} - \delta + \frac{r}{\tan\alpha}\right) \tag{8.13}$$

To determine contact area for each asperity, A_i, we can rewrite Eq. 8.6 for perfectly plastic deformation as

$$A_i = \pi a_i^2 = f(\delta_i) = \frac{2\pi}{k_s}\left(z_s - \left(z_{90} - \delta + \frac{r}{\tan\alpha}\right)\right) \tag{8.14}$$

where k_s denotes the average curvature of summits. Now the contact area within the annular ring of width dr is given by

$$A = N_u \frac{4\pi^2 r dr}{k_s} \int_{z_{90}-\delta+\frac{r}{\tan\alpha}}^{\infty} \left(z_s - \left(z_{90} - \delta + \frac{r}{\tan\alpha}\right)\right) \phi(z_s) dz_s \tag{8.15}$$

Therefore, to determine the total contact area for an approach δ, we can integrate the above equation for $r = 0$ to R to obtain,

$$A = \frac{4\pi^2 N_u}{k_s} \int_{r=0}^{R} \int_{z_{90}-\delta+\frac{r}{\tan\alpha}}^{\infty} \left(z_s - \left(z_{90} - \delta + \frac{r}{\tan\alpha}\right)\right) \phi(z_s) dz_s dr \tag{8.16}$$

8.2.3. Implementation of Profilometric Theory

Topographic data obtained from atomic force microscopy imaging was used to calculate actual contact area using Greenwood and Williamson's theory. First, a distribution of surface height was created. Actual contact area was calculated using Eq. 8.16 for different indentation depth with an increment of 50 nm. Figure 8.4 plots the ratio of actual contact area to nominal contact area vs. contact depth. At smaller indentation depth, this ratio is considerably lower than 1, i.e. the actual contact area is significantly smaller than the nominal contact area. As indentation depth increases, the ratio of actual contact area over nominal contact area approaches unity. From Figure 8.4, the

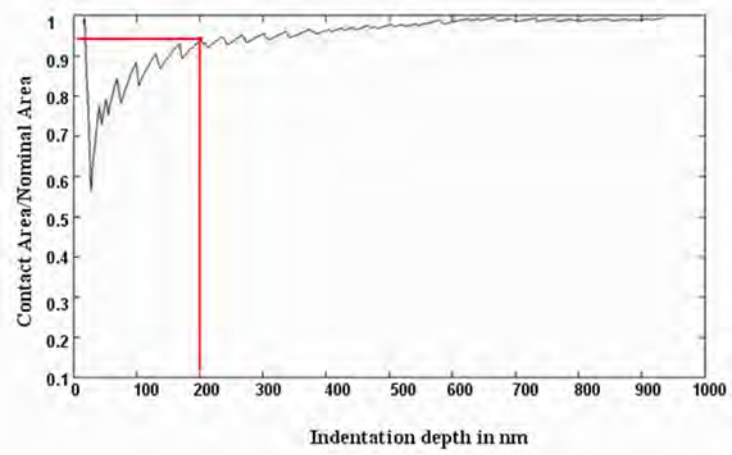

Figure 8.4. Effect of Surface Roughness on Contact Area: Plot of Indentation Depth vs. Ratio of Actual Contact Area to Nominal Contact Area

ratio is around 0.95 for the average contact depth used in this study. Therefore, the error introduced by the assumption of flat surface in the contact analysis was not more than 5%.

8.2.4. Limitations of Profilometric Theory

Greenwood and Williamson analysis of rough surface is based on the assumption that the deformation of each aspirity is independent of its neighbors. Surface displacements at non-contact points are neglected. The shape of the contact area is then determined by a purely geometrical analysis of undeformed surface topography as measured by a profilometric device. Stress−displacement response of only isolated microcontacts are considered, neglecting any interactions between them.

8.3. Numerical Methods for Contact Analysis

Many non-Hertzian contact problems do not permit analytical solutions in closed form. This has led to development of various numerical methods. These are the only approaches that can accurately account for interaction between microcontacts while solving contact problems on a rough

surface. The basis for all these methods is to determine the traction distributed over the surface that satisfy boundary conditions within and outside the contact area where the shape and size of the contact area is not a know *a priori*. In general, traction is considered as a combination of discrete forces on the surface. Displacement at any point is computed by summing the displacements due to all the forces. The gap between the two surfaces before deformation is denoted by a function $h(x, y)$. As before, we can write the conditions for a contact as

$$\bar{u}_{z1} + \bar{u}_{z2} + h(x, y) - \delta \begin{cases} = 0 & \text{within contact} \\ > 0 & \text{outside contact} \end{cases} \tag{8.17}$$

where δ is the approach of the two bodies. Contact surface is divided into segments of appropriate size. Displacement at a point i due to a pressure at j is given by an influence coefficient C_{ij}. Therefore, the total displacement at a general mesh point i is

$$\{\bar{u}_z\}_i = -\frac{(1-\nu^2)c}{E} \sum C_{ij} p_j \tag{8.18}$$

The total force acting of the surface can be calculated as the sum of all the pressure by

$$P = A \sum p_j \tag{8.19}$$

Distribution of forces can be solved in various ways. Here, two different methods area summarized.

a) Matrix Inversion Method

For n number of pressure elements, Eq. 8.18 can be used to determine surface displacements and

we can rewrite Eq. 8.17 as follows

$$\sum_{j=0}^{n-1} C_{ij} p_j \quad = \quad \left(\frac{E^*}{c}\right)(h-\delta) \tag{8.20}$$

Now, if the approach distance δ is specified, Eq. 8.20 can be solved for n unknown values of p_j by direct matrix inversion. Since the size and the shape of the contact area is not know, an assumption of the contact area must be made. If the value of δ is specified, a first approximation of the contact area can be obtained from the geometric interpenitration of the two profiles. After solving Eq. 8.20, some points near the periphery of the contact area may appear to have negative values of pressure. In the second iteration, these points are excluded and the procedure is repeated until it converges.

a) Variational Method

Varitional method utilizes well-established optimization technique such as quadratic programming for the numerical solution. Duvaut and Lions [40] showed that the real contact area and surface displacements can be calculated by minimizing total strain energy U_E for a particular approach distance δ without any interpenitration i.e.

$$\bar{u}_{z1} + \bar{u}_{z2} + h(x,y) - \delta \geq 0 \tag{8.21}$$

Kalker [40] Proposed an alternative way to calculate contact area by minimizing total complementary energy V^* where V^* is

$$V^* \quad = \quad U_E^* + \int_S p(h-\delta) dS \tag{8.22}$$

In the above equation, p represents the pressure acting on the surface S and U_E^* is the internal complementary energy of the two bodies in contact. For linear elastic materials, U_E^* is numerically equal to the elastic strain energy and can be calculated as

$$U_E^* = U_E = \frac{1}{2}\int_S p(\bar{u}_{z1} + \bar{u}_{z2})dS \tag{8.23}$$

Dividing the contact area S into suitable mesh, we can write

$$U_E^* = -\frac{cA}{2E^*}\sum\left(\sum C_{ij}p_j\right)p_i \tag{8.24}$$

$$\int_S p(h-\delta)dS = A\sum p_i(h_i - \delta) \tag{8.25}$$

Hence, V^* is an objective function quadratic in p_i and values of p_i which minimize V^* can be calculated using a standard quadratic programming routine.

8.3.1. Implementation of Numerical Methods for Contact Analysis of Rough Surface

As mentioned in the previous section, the most suitable approach to compute microcontact interaction for rough surfaces is direct numerical solution of the contact problem. As summarized by Polonsky and Keer [65], numerical solution of 3D rough contact problem can be solved by discretizing the contacting surfaces. Surfaces are divided into uniformly spaced rectangular array of surface points or surface grids. Surface height data or topography data for the surface at each grid points are obtained from a 3D surface imaging device such as an atomic force microscope. Tip profile can be generated by knowing the tip geometry. Surface grid for both the surfaces should

match exactly with the same number of points in the x and the y direction. It is also assumed that the reference plane for the surfaces become parallel and all the grid points match when the two bodies come into contact. This simplifies the solution making it possible to use a single grid to describe shape, stresses and deformations of both the bodies. Actual contact area can be determined using the contact criterion mention in Eq. 8.17 and matrix inversion method can be used to determine contact forces. In practice, this method requires lot of computer memory and convergence is slow. Polonsky and Keer [65] proposed an alternative numerical method based on two dimensional multi-level multi summation algorithm. This technique will be considered in the future for solving indentation on cementitious materials.

8.4. Conclusion

In this chapter surface roughness criteria for applying nanoindentation to characterize cementitious material is revisited. Actual contact area was calculated following Greenwood and Williamson's analysis for different indentation depth. It was found that at smaller indentation depth, this ratio is considerably lower than 1. As the indentation depth increases, the ratio of actual contact area to nominal contact area approaches unity. This ratio is around 0.95 for the average contact depth used in previous chapters. Therefore, the error introduced by the assumption of contact between flat surfaces was not more than 5%.

The author is also aware of the limitations of the analysis by Greenwood and Williamson. As surface displacements at non-contact points are neglected, it introduces error. Applicability of a numerical simulation to solve rough surface contact problem is considered. However, in practice, this method requires lot of computer memory and convergence is slow. An alternative numerical

method based on two dimensional multi-level multi summation algorithm, proposed by Polonsky and Keer [65], will be considered in the future for solving indentation on cementitious materials.

Chapter 9 Conclusions and Future Work

This thesis examines nanomechanical properties of significant phases of cement paste microstructure and concrete. With a goal of improving the understanding of the basic properties of concrete and cementitious materials, nanoindentation experiments were performed on cement pastes with different water to cement ratio at different curing ages. The major challenge of applying nanoindentation to characterize cementitious material was preparing the sample surface. A systematic technique for preparing the sample surface was developed to minimize surface roughness. Furthermore, from a contact analysis and 2 dimensional simulation of indentation, it was shown that the error introduced by the surface roughness is not more than 5%. Nanoindentation was also used to determine local mechanical properties of the interfacial transition zone (ITZ) and

to investigate effects of adding a micro-modifier such as silica fume and nano-modifier (nanosilica) on the nanomechanical properties. This final chapter summarizes the conclusions made in the course of this study and proposes areas of future work.

9.1. Conclusions

The major challenge of applying nanoindentation to characterize cementitious material is preparing the sample surface. The theory of nanoindentation is developed based on the assumption of indentation on a flat surface. Therefore, the accuracy of nanoindentation experiments on cementitious materials depend on reducing surface roughness to a tolerable level without causing any damage to the sample. In this study, a systematic technique for preparing the sample surface was developed. Cement paste micro- and nanostructure was studied using atomic force microscopy (AFM) imaging. The structure of C-S-H gel in different areas showed spherical particles of different sizes in the range of 200-700 nm. The improved polishing protocol proposed in this work, facilitated identification of spherical particles as small as 40 nm in many areas of C-S-H. The size of these spherical particles were found to vary in different areas, which seems to be an inherent nature of C-S-H.

AFM topography imaging was used to compute the RMS roughness for quantitative analysis of surface roughness. The data showed an increasing trend of the RMS roughness with increase in image size. It was found that an area on the order of the nominal contact area during one indentation has very little surface roughness. However, the RMS roughness reported in this study was found to be higher than that reported by Ulm et al. [48]. The results obtained in the current work conform with the one presented by Trtik, Holzer and et al. [79]. According to Holzer et

al., the average intrinsic RMS roughness of cement paste is between 115 nm to 492 nm and a RMS roughness below this may indicate surface damage and polishing artifacts. However, while comparing literature, it is important to note that the two above mentioned papers do not report surface roughness values of cement paste with the same water to cement ratio. At lower water to cement ratio, less porosity of a paste sample will possibly show less roughness after polishing. Ulm et al. used a very low water to cement ratio, (w/c = 0.2) [48], and this may explain the lower RMS roughness reported.

The main conclusions made in the course of this study are summarized below:

1) The average modulii of the four main phases present in cement paste, viz. (i) a porous phase with very low modulus (around 10 GPa), (ii) a low stiffness C-S-H phase (around 16 GPa), (iii) a high stiffness C-S-H phase (around 26 GPa), and (iv) calcium hydroxide (around 35 GPa), do not change with change in water to cement ratio. However, while the volume fraction of the porous phase and the low stiffness C-S-H decrease significantly with increase in the water to cement ratio, the volume fraction of the high stiffness C-S-H increases. Hence, in can be concluded that higher macroscopic strength at low water to cement ratio is a combined effect of large volume of high stiffness C-S-H phase and unhydrated cement particles, and lower porosity.

2) Both the average phase properties and the volume fraction of these phases do not change with the curing age of cement paste. This indicates that, with an increase in the curing age, both the low stiffness and the high stiffness C-S-H form while keeping the relative volume unchanged. The macroscopic strength increase may be attributed to the reduction in macro-porosity and increase in the percolation of solids due to formation of both the low stiffness and the high stiffness C-S-H.

3) Replacing 15% cement by silica fume did not show any change in the elastic modulus of the four phases. A reduction in the volume fraction of calcium hydroxide in samples with silica fume provided evidence of pozzolanic reaction. An increase in the volume fraction of the high stiffness C-S-H was observed and the percent increase is comparable with the decrease in the volume fraction of calcium hydroxide. 10% increase in the ratio of high stiffness to low stiffness C-S-H suggests that pozzolanic reaction converts calcium hydroxide to high stiffness C-S-H. However, this could also be an effect of improved packing due to silica fume. This observation is particularly interesting since it compares well with the literature reporting higher volume fraction of C-S-H with longer chain length in cement paste blended with silica fume [70]. However, further study on the change in morphology of C-S-H due to addition of silica fume is necessary.

4) A parallel study of cement pastes with nanosilica using ^{29}Si MAS-NMR spectra reported that nanosilica increases the average chain length of C-S-H gel [32]. Hence, it can be expected that nanosilica increases either the strength or the proportion of high stiffness C-S-H in the paste. The nanoindentation study, however, proved that the elastic modulus of either of the two C-S-H phases remain unaltered with the addition of nanosilica, while the volume fraction of high stiffness C-S-H gel increased significantly. In sample with 18% nanosilica, the volume fraction of high stiffness C-S-H was as high as 50%.

5) The ITZ was found to be extremely heterogeneous. Higher concentrations of large voids and cracks along the interface was observed due to poor bonding. However, some areas of the ITZ were as strong as the bulk matrix. Nanoindentation results on relatively intact areas of the interface disagree with the notion of increasing elastic modulus with distance from the interface.

6) Nanoindentation results showed higher porosity even in relatively intact areas of the ITZ and consequently, it was not possible to determine the volume fraction of the different phases. Depending on the aggregate type, the average modulus of the ITZ was found to be 15-30% lower than that of the bulk matrix. However, the detrimental effect of the ITZ on the overall mechanical properties of concrete is due to its extreme heterogeneity and poor bonding between the aggregate and the paste. It is important to note that the connectivity of the weaker areas such as large voids and cracks along the interface will govern failure. Thus, modeling concrete as three phase material considering the ITZ as a weak zone around aggregates with average property some percentage less than the paste matrix may not be sufficient to predict overall strength.

7) The addition of silica fume had greater effects on the nanomechanical properties of the ITZ than on bulk paste. Comparing the modulus of the interfacial transition zone in samples with and without silica fume, it was found that the addition of silica fume increased stiffness and reduced porosity of the ITZ. Furthermore, the addition of silica fume eliminated large cracks and voids at the interface making the ITZ more homogeneous. In samples with 15% silica fume, the interface was found to have the same average modulus as that of the bulk paste with silica fume. The ratio of the high stiffness to the low stiffness C-S-H is found to be little higher in the ITZ than in the bulk paste. One possible explanation for this could be due to the excess amount calcium hydroxide initially available in the ITZ if pozzolanic reaction is assumed to produces more high stiffness C-S-H.

8) Finally, analysis for surface roughness was performed. Actual contact area was calculated using the Greenwood and Williamson's analysis for different indentation depth. It was found that

at smaller indentation depth, the ratio of actual contact area to nominal contact area is considerable less than 1. However, as the indentation depth increased, the ratio approached unity. This ratio was found to be around 0.95 for the average contact depth used in this study. Therefore, the error introduced by the assumption of flat surface was not more than 5%.

9.2. Recommendation for Future Research

It is hoped that better understanding of the nanomechanical properties of cement paste, interfacial transition zone and effects of micro and nano silica based additives can be employed to develop an advanced model to predict overall properties and to develop new materials with improved properties by altering the nanostructure. Though this research provided valuable insight on nanoscale local mechanical properties, the outcome was still restricted by the limitations of the available techniques. As the next step, the precise relationship between nanostructure of calcium silicate hydrate and mechanical properties can be studied using tools such as atomic force microscopy combined with ultrasonic force microscopy; this will yield a higher resolution than what has been possible up to now.

Furthermore, effects of sample preparation and surface roughness of nanomechanical properties should be studied. A numerical simulation of nanoindentation using advanced technique shuch as one proposed by Polonsky and Keer [65] could be considered for solving indentation on cementitious materials.

References

[1] A. J. Allen and J. J. Thomas. Analysis of C-S-H gel and cement paste by small-angle neutron scattering. *Cement and Concrete Research*, 37(3):319–324, 2007.

[2] A. J. Allen, J. J. Thomas, and H. M. Jennings. Composition and density of nanoscale calcium-silicate-hydrate in cement. *Nature Materials*, 6(4):311–316, 2007.

[3] A. H. Asbridge, C. L. Page, and M. M. Page. Effects of metakaolin, water/binder ratio and interfacial transition zones on the microhardness of cement mortars. *Cement and Concrete Research*, 32(9):1365–1369, 2002.

[4] D. P. Bentz, E. J. Garboczi, and E. Schlangen. Computer simulation of interfacial zone microstructure and its effect on the properties of cement-based composites. *Materials Science of Concrete*, 4:44, 1995.

[5] G. Binnig, C. F. Quate, and C. Gerber. Atomic force microscope. *Physical review letters*, 56(9), March 1986.

[6] B. Birgisson. Nanomodificationof cement paste to improve bulk properties of concrete. In *NSF Workshop on Nanomodification of Cementitious Materials: Portland Cement Concrete and Asphalt Concrete*, Gainesville; Florida, August 2006.

[7] M. S. Bischel, M. R. VanLandingham, R. F. Eduljee, J. W. Gillespie Jr., and J. M. Schultz. On the use of nanoscale indentation with the afm in the identification of phases in blends of linear low density polyethylene and high density polyethylene. *Journal of Materials Science*, 35(1):221–228, January 2000.

[8] M. S. Bobji and S. K. Biswas. Estimation of hardness by nanoindentation of rough surfaces. *Journal of Materials Research*, 13(11):3227–3233, 1998.

[9] D. Breton, A. Carles-Gibergues, G. Ballivy, and J. Grandet. Contribution to the formation mechanism of the transition zone between rock-cement paste. *Cement and Concrete Research*, 23(2):335–346, 1993.

[10] B. Cappella, P. Baschieri, C. Frediani, P. Miccoli, and C. Ascoli. Force-distance curves by afm. *Engineering in Medicine and Biology Magazine, IEEE*, 16(2):58–65, 1997.

[11] R. W. Carpick and M. Salmeron. Scratching the surface: Fundamental investigations of tribology with atomic force microscopy. *Chem. Rev.*, 97(4):1163–1194, 1997.

[12] Y. W. Chan and S. H. Chu. Effect of silica fume on steel fiber bond characteristics in reactive powder concrete. *Cement and Concrete Research*, 34(7):1167–1172, 2004.

[13] C. M. Cheng and Y. T. Cheng. On the initial unloading slope in indentation of elastic-plastic solids by an indenter with an axisymmetric smooth profile. *Applied Physics Letters*, 71(18):2623, 1997.

[14] Y. T. Cheng and C. M. Cheng. Further analysis of indentation loading curves: Effects of tip rounding on mechanical property measurements. *Journal of Materials Research*, 13(4):1059–1064, 1998.

[15] Y. T. Cheng and C. M. Cheng. Relationship between hardness, elastic modulus, and the work of indentation. *Applied Physical Letters*, 73(5):614–616, 1998.

[16] Y. T. Cheng and C. M. Cheng. Can stress-strain relationships be obtained from indentation curves using conical and pyramidal indenters? *Journal of Materials Research*, 14(9):3493–3496, 1999.

[17] Y. T. Cheng and C. M. Cheng. General relationship between contact stiffness, contact depth, and mechanical properties for indentation in linear viscoelastic solids using axisymmetric indenters of arbitrary profiles. *Applied Physics Letters*, 87(11):111914, 2005.

[18] T. D. Ciach, J. E. Gillott, E. G. Swenson, and P. J. Sereda. Microstructure of calcium silicate hydrates. 1(1):13–25, 1971.

[19] T. D. Ciach and E. G. Swenson. Morphology and microstructure of hydrating Portland cement and its constituents- 5. 1(5):515–30, 1971.

[20] G. Constantinides. *Material Invariant Properties of Cement-Based Materials: Instrumented Nanoindentation Microporomechanical Modeling*. PhD thesis, Massachusetts Institute of Technology, Boston MA, USA, May 2005.

[21] G. Constantinides and F. J. Ulm. The effect of two types of C-S-H on the elasticity of cement-based materials: Results from nanoindentation and micromechanical modeling. *Cement and Concrete Research*, 34(1):67–80, 2004.

[22] G. Constantinides and F. J. Ulm. The effect of two types of C-S-H on the elasticity of cement-based materials: Results from nanoindentation and micromechanical modeling. *Cement and Concrete Research*, 34:67–80, 2004.

[23] G. Constantinides and F. J. Ulm. The nanogranular nature of C-S-H. *Journal of the Mechanics and Physics of Solids*, 55(1):64–90, 2007.

[24] G. Constantinides, F. J. Ulm, and K. Van, Vliet. On the use of nanoindentation for cementitious materials. *Materials and Structures/Matériaux et Constructions*, 36(257):191–196, April 2003.

[25] M. J. DeJong and F. J. Ulm. The nanogranular behavior of C-S-H at elevated temperatures (up to 700° c). *Cement and Concrete Research*, 37(1):1–12, 2007.

[26] S. Diamond and E. E. Lachowski. On the morphology of type III C-S-H gel. *Cement and Concrete Research*, 10:703–705, 1980.

[27] S. Diamond and S. Sahu. Densified silica fume: Particle sizes and dispersion in concrete. *Materials and Structures*, 39(9):849–859, 2006.

[28] A. Elsharief, M. D. Cohen, and J. Olek. Influence of aggregate size, water cement ratio and age on the microstructure of the interfacial transition zone. *Cement and Concrete Research*, 33(11):1837–1849, 2003.

[29] C. Famy, A. R. Brough, and H. F. W. Taylor. The C-S-H gel of Portland cement mortars: Part I. The interpretation of energy-dispresive X-ray microanalyses from scanning electron microscopy, with some observations on C-S-H, AFm and AFt microscopy phase compositions. *Cement and Concrete Research*, 33:1389–1398, 2003.

[30] R. F. Feldman and P. J. Sereda. A model for hydrated Portland cement paste as deduced from sorption-length change and mechanical properties. *Matáriux Et Constructions*, 1(6):509–520, 1968.

[31] Fischer-Cripps and C. Anthony. *Nanoindentation*. Springer-Verlag, New York, Secaucus, NJ USA, 2002.

[32] J. J. Gaitero. *Multi-scale study of the fibre matrix interface and calcium leaching in high performance concrete*. PhD thesis, Centre for Nanomaterials Applications in Construction of Labein-Tecnalia, Spain, December 2008.

[33] J. A. Greenwood and J. B. P. Williamson. Contact of nominally flat surfaces. *Proceedings of the Royal Society of London. Series A, Mathematical and Physical Sciences*, 295(1442):300–319, 1966.

[34] J. Hu and P. Stroeven. Properties of the interfacial transition zone in model concrete. *Interface Science*, 12(4):389–397, 2004.

[35] J. J. Hughes and P. Trtik. Micro-mechanical properties of cement paste measured by depth-sensing nanoindentation: a preliminary correlation of physical properties with phase type. *Materials Characterization*, 53(2-4):223–231, November 2004.

[36] H. M. Jennings. *The developing microstructure of Portland cement*. Pergamon Press, 1983.

[37] H. M. Jennings. A model for the microstructure of calcium silicate hydrate in cement paste. *Cement and Concrete Research*, 30:101–116, 2000.

[38] H. M. Jennings. Colloid model of C-S-H and implication to the problem of creep and shrinkage. *Materials and Structures/Concrete Science and Engineering*, 37:59–70, January-February 2004.

[39] H. M. Jennings and P. D. Tennis. Model for the microstructure in Portland cement paste. *Journal of the American Ceramic Society*, 77(12):3161–3172, 1994.

[40] K. L. Johnson. *Contact Mechanics*. Cambridge University Press, Cambridge UK, 1999.

[41] A. Kauppi, K. M. Andersson, and L. Bergström. Probing the effect of superplasticizer adsorption on the surface forces using the colloidal probe afm technique. *Cement and Concrete Research*, 35:133–140, 2005.

[42] M. Kuroda, T. Watanabe, and N. Terashi. Increase of bond strength at interfacial transition zone by the use of fly ash. *Cement and Concrete Research*, 30(2):253–258, 2000.

[43] G. Li, Y. Zhao, and S. S. Pang. Four-phase sphere modeling of effective bulk modulus of concrete. *Cement and Concrete Research*, 29(6):839–845, 1999.

[44] G. Li, Y. Zhao, S. S. Pang, and Y. Li. Effective young's modulus estimation of concrete. *Cement and Concrete Research*, 29(9):1455–1462, 1999.

[45] J. Linhua. The interfacial zone and bond strength between aggregates and cement pastes incorporating high volumes of fly ash. *Cement and Concrete Composites*, 21(4):313–316, 1999.

[46] M. P. Lutz, P. J. M. Monteiro, and R. W. Zimmerman. Inhomogeneous interfacial transition zone model for the bulk modulus of mortar. *Cement and Concrete Research*, 27(7):1113–1122, 1997.

[47] P. K. Mehta and P. J. M. Monteiro. *Concrete, Microstructure, Properties and Materials*. McGraw Hill, NY, USA, third edition edition, 2004.

[48] M. Miller, C. Bobko, M. Vandamme, and F. J. Ulm. Surface roughness criteria for cement paste nanoindentation. *Cement and Concrete Research*, 38(4):467–476, 2008.

[49] S. Mindess, J. F. Young, and D. Darwin. *Concrete*. Prentice Hall, NJ, USA, second edition edition, 2003.

[50] L. D. Mitchell, M. Prica, and J. D. Birchall. Aspects of Portland cement hydration studied using atomic force microscopy. *Journal of Materials Science*, 31:4207–4212, 1996.

[51] P. Mondal, S. P. Shah, and L. D. Marks. Atomic force microscopy for cementitious materials. In *RILEM Proceedings: Nanotechnology in Construction*, pages 179–185, 2006.

[52] P. Mondal, S. P. Shah, and L. D. Marks. A reliable technique to determine the local mechanical properties at the nano-scale for cementitious materials. *Cement and Concrete Research*, 37:1440–1444, 2007.

[53] P. Mondal, S. P. Shah, and L. D. Marks. Nano-scale characterization of cementitious materials. *ACI Materials Journal*, 105(2):174–179, March-April 2008.

[54] P. Mondal, S. P. Shah, and L. D. Marks. Use of atomic force microscopy and nanoindentation for characterization of cementitious materials at the nanoscale. *SP-254: Nanotechnology of Concrete: Recent Developments and Future Perspectives*, 2008.

[55] J. C. Nadeau. Water-cement ratio gradients in mortars and corresponding effective elastic properties. *Cement and Concrete Research*, 32(3):481–490, 2002.

[56] J. Nemecek, L. Kopecky, and Z. Bittnar. Size effect in nanoindentation of cement paste. In *Proceedings of the International Conference held at the University of Dundee*, Scotland; UK, July 2005. Thomas Telford.

[57] A. M. Neville. *Properties of Concrete*. Longman Group Limited, Essex, England, fourth edition edition, 1995.

[58] A. Nonat. The structure and stoichiometry of C-S-H. *Cement and Concrete Research*, 34:1521–1528, 2004.

[59] W. C. Oliver and G. M. Pharr. An improved technique for determining hardness and elastic modulus using load and displacement sensing indentation experiments. *Journal of Material Research*, 7:1564–1583, 1992.

[60] R. A. Olson and H. M. Jennings. Estimation of C-S-H content in a blended cement paste using water adsorption. *Cement and Concrete Research*, 31(3):351–356, 2001.

[61] V. G. Papadakis, E. J. Pedersen, and H. Lindgreen. An afm-sem investigation of the effect of silica fume and fly ash on cement paste microstructure. *Journal of Materials Science*, 34:683–690, 1999.

[62] V. A. Paulon, D. Dal Molin, and P. J. M. Monteiro. Statistical analysis of the effect of mineral admixtures on the strength of the interfacial transition zone. *Interface Science*, 12(4):399–410, 2004.

[63] X. Ping and J. J. Beaudoin. Modification of transition zone microstructure –silica fume coating of aggregate surfaces. *Cement and Concrete Research*, 22(4):597–604, 1992.

[64] C. Plassard, E. Lesniewska, I. Pochard, and A. Nonat. Investigation of the surface structure and elastic properties of calcium silicate hydrates at the nanoscale. *Ultramicroscopy*, 100(3-4):331–338, August 2004.

[65] I. A. Polonsky and L. M. Keer. A numerical method for solving rough contact problems based on the multi-level multi-summation and conjugate gradient techniques. *Wear*, 231(2):206–219, 1999.

[66] C. S. Poon, S. C. Kou, and L. Lam. Compressive strength, chloride diffusivity and pore structure of high performance metakaolin and silica fume concrete. *Construction and Building*

Materials, 20(10):858–865, 2006.

[67] G. Prokopski and J. Halbiniak. Interfacial transition zone in cementitious materials. *Cement and Concrete Research*, 30(4):579–583, 2000.

[68] G. Ramesh, E. D. Sotelino, and W. F. Chen. Effect of transition zone on elastic stresses in concrete materials. *Journal of Materials in Civil Engineering*, 10(4):275–282, 1998.

[69] C. Reynaud, F. Sommer, C. Quet, C. El, Bounia, and T. M. Duc. Quantitative determination of young's modulus on a biphase polymer system using atomic force microscopy. *Surface and Interface Analysis*, 30:185–189, 2000.

[70] I. G. Richardson. Tobermorite/jennite and tobermorite/calcium hydroxide-based models for the structure of C-S-H: Applicability to hardened pastes of tricalcium silicate, β-dicalcium slicate, Portland cement, and blends of Portland cement with blast-furnace slag, metakaolin, or silica fume. *Cement and Concrete Research*, 34:1733–1777, 2004.

[71] J. S. Ryu and P. J. M. Monteiro. Effect of specific gravity of coarse aggregate on interfacial transition zone, permeability, and strength of concrete. *British Ceramic Transactions*, 101:30–34, 2002.

[72] K. L. Scrivener, A. K. Crumbie, and P. Laugesen. The interfacial transition zone (itz) between cement paste and aggregate in concrete. *Interface Science*, 12(4):411–421, 2004.

[73] P. Simeonov and S. Ahmad. Effect of transition zone on the elastic behavior of cement-based composites. *Cement and Concrete Research*, 25(1):165–176, 1995.

[74] I. Sneddon. The relation between load and penetration in the axisymmetris boussinesq problem for a punch of arbitrary profile. *International Journal of Engineering Science*, 3:47–57,

1965.

[75] I. Sneddon. *Application of Integral Transforms in the Theory of Elasticity*. Springer Verlag, Wien-New York, 1977.

[76] Z. Sun, E. J. Garboczi, and S. P. Shah. Modeling the elastic properties of concrete composites: Experiment, differential effective medium theory, and numerical simulation. *Cement and Concrete Composites*, 29(1):22–38, 2007.

[77] H. F. W. Taylor. *Cement Chemistry*. Telford, 1997.

[78] S. Timoshenko and J. N. Goodier. *Theory of Elasticity*. McGraw-Hill, New York, 3rd edition edition, 1951.

[79] P. Trtik, J. Dual, B. Muench, and L. Holzer. Limitation in obtainable surface roughness of hardened cement paste: Virtual topographic experiment based on focussed ion beam nanotomography datasets. *Journal of Microscopy*, 6(4):311–316, 2008.

[80] F. J. Ulm. Chemomechanics of concrete at finer scales. *Materials and Structures/Matériaux et Constructions*, 36:426–438, August-September 2003.

[81] F. J. Ulm, G. Constantinides, and Heukamp F. H. Is concrete a poromechanics material? - A multiscale investigation of poroelastic properties. *Materials and Structures/Concrete Science and Engineering*, 37:43–58, January-February 2004.

[82] F. J. Ulm, M. Vandamme, C. Bobko, J. A. Ortega, K. Tai, and C. Ortiz. Statistical indentation techniques for hydrated nanocomposites: Concrete, bone, and shale. *Journal of the American Ceramic Society*, 90(9):2677–2692, 2007.

[83] M. R. Vanlandingham, S. H. McKnight, G. R. Palmese, R. F. Eduljee, J. W. Jr. Gillespie, and R. L. McCulough. Relating elastic modulus to indentation response using atomic force microscopy. *Journal of Materials Science Letters*, 16(2):117–119, January 1997.

[84] M. R. Vanlandingham, S. H. McKnight, G. R. Palmese, R. F. Eduljee, Jr. Gillespie, and R. L. McCulough. Relating ploymer indentation behavior to elastic modulus using atomic force microscopy. *Material Research Society*, 1996.

[85] K. Velez, S. Maximilien, D. Damidot, G. Fantozzi, and F. Sorrentino. Determination by nanoindentation of elastic modulus and hardness of pure constituents of Portland cement clinker. *Cement and Concrete Research*, 31:555–561, 2001.

[86] T. Yang, B. Keller, and E Magyari. Afm investigation of cement paste in humid air at different relative humidities. *Journal of Physics D: Applied Physics*, 35:L25–L28, 2002.

[87] T. Yang, B. Keller, E. Magyari, K. Hametner, and D. Günther. Direct observation of the carbonation process on the surface of calcium hydroxide crystals in hardened cement paste using atomic force microscope. *Journal of materials Science*, 38:1909–1916, 2003.

[88] W. Zhu and P. J. M. Bartos. Application of depth-sensing microindentation testing to study of interfacial transition zone in reinforced concrete. *Cement and Concrete Research*, 30(8):1299–1304, 2000.

[89] W. Zhu, M. Sonebi, and P. J. M. Bartos. Bond and interfacial properties of reinforcement in self-compacting concrete. *Materials and Structures/Materiaux et Constructions*, 37:442–448, August-September 2004.